Predictions for the secondary CO, C and O gas content of debris discs from the destruction of volatile-rich planetesimals

Quentin Kral,[★] Luca Matrà, Mark C. Wyatt and Grant M. Kennedy
Institute of Astronomy, University of Cambridge, Madingley Road, Cambridge CB3 0HA, UK

ABSTRACT

This paper uses observations of dusty debris discs, including a growing number of gas detections in these systems, to test our understanding of the origin and evolution of this gaseous component. It is assumed that all debris discs with icy planetesimals create second generation CO, C and O gas at some level, and the aim of this paper is to predict that level and assess its observability. We present a new semi-analytical equivalent of the numerical model of Kral et al. allowing application to large numbers of systems. That model assumes CO is produced from volatile-rich solid bodies at a rate that can be predicted from the debris discs fractional luminosity. CO photodissociates rapidly into C and O that then evolve by viscous spreading. This model provides a good qualitative explanation of all current observations, with a few exceptional systems that likely have primordial gas. The radial location of the debris and stellar luminosity explain some non-detections, e.g. close-in debris (like HD 172555) is too warm to retain CO, while high stellar luminosities (like η Tel) result in short CO lifetimes. We list the most promising targets for gas detections, predicting >15 CO detections and >30 C I detections with ALMA, and tens of C II and O I detections with future far-IR missions. We find that CO, C I, C II and O I gas should be modelled in non-LTE for most stars, and that CO, C I and O I lines will be optically thick for the most gas-rich systems. Finally, we find that radiation pressure, which can blow out C I around early-type stars, can be suppressed by self-shielding.

Key words: accretion, accretion discs – hydrodynamics – interplanetary medium – Planetary systems – planet–disc interactions – circumstellar matter.

1 INTRODUCTION

Gas is observed around a growing number of planetary systems where planets are likely to be formed and the protoplanetary discs in which they formed are already gone. All these gas detections are in systems where secondary dust is created from collisions by bigger bodies orbiting in a debris belt similar to the Kuiper or asteroid belt in our Solar system. Similarly, the observed gas around these mature systems may also be of secondary origin and being released from debris belt planetesimals/dust owing to grain–grain collisions (Czechowski & Mann 2007), planetesimal breakup (Zuckerman & Song 2012), sublimation (e.g. Beust et al. 1990), photodesorption (Grigorieva et al. 2007) or giant impacts (Lisse et al. 2009; Jackson et al. 2014). For some systems such as HD 21997, the observed gas may be of primordial origin (Kóspál et al. 2013).

Molecular CO gas is observed in the sub-mm with both single-dish telescopes (JCMT, APEX) and interferometers such as ALMA,

the SMA or NOEMA. For the brightest targets, ALMA's high-resolution and unprecedented sensitivity allow us to obtain CO maps for different lines and isotopes showing the location of CO belts and giving an estimate of their mass (see the CO gas disc around β Pic, Dent et al. 2014; Matrà et al. 2017). Atomic species are also detected around a few debris disc stars. In particular, *Herschel* was able to detect the O I and C II fine structure lines in two and four systems, respectively (e.g. Riviere-Marichalar et al. 2012, 2014; Roberge et al. 2013; Cataldi et al. 2014; Brandeker et al. 2016). Also, metals have been detected, using UV/optical absorption lines, around β Pictoris (Na, Mg, Al, Si and others, Roberge et al. 2006), 49 Ceti (Ca II, Montgomery & Welsh 2012) and HD 32297 (Na I, Redfield 2007). Some of these metals are on Keplerian orbits but should be blown out by the ambient radiation pressure (Olofsson, Liseau & Brandeker 2001). It is proposed that the overabundant ionized carbon observed around β Pic, which is not pushed by radiation pressure could brake other ionized species due to Coulomb collisions with them (Fernández, Brandeker & Wu 2006). A stable disc of hydrogen has not yet been observed in these systems (Freudling et al. 1995; Lecavelier des Etangs et al. 2001) but some high

Table 1. List of all known debris discs with gas.

Star's name	Atoms and molecules observed	L_* ($L_\odot$)	d (pc)	M_{CO} ($M_\oplus$)[a]	R_0 (au)	M_{dust} ($M_\oplus$)	L_{IR}/L_*	Star's age (Myr)
β Pic (1)	CO, C I, C II, O I, ...	8.7	19.4	2.8×10^{-5}	85	7.8×10^{-2}	1.7×10^{-3}	23
49 Ceti (2)	CO, C I, C II, O I[b]	15.5	59.4	1.4×10^{-4}	100	0.27	1.1×10^{-3}	40
η Tel (3)	C II	22	48.2	–	24	1.3×10^{-2}	7.6×10^{-4}	23
HD 21997 (4)	CO	14.4	71.9	6×10^{-2}	60	0.16	5.9×10^{-4}	45
HD 32297 (5)	CO, C II	5.6	112	1.3×10^{-3}	110	0.37	5.4×10^{-3}	30
HD 110058 (6)	CO	5.9	107	2.1×10^{-5}	50	3×10^{-3}	1.9×10^{-3}	10
HD 131835 (7)	CO	9.2	122	6×10^{-2}	50	0.47	1.5×10^{-3}	16
HD 138813 (6)	CO	24.5	150.8	7.4×10^{-4}	100	7.6×10^{-3}	1.5×10^{-3}	10
HD 146897 (6)	CO	3.1	122.7	2.1×10^{-4}	100	2×10^{-2}	5.4×10^{-3}	10
HD 156623 (6)	CO	14.8	118	2.0×10^{-3}	75	2.4×10^{-4}	5.5×10^{-3}	10
HD 172555 (8)	O I	7.8	29	–	6	4.8×10^{-4}	7.8×10^{-4}	23
HD 181327 (9)	CO	3.1	51.8	1.8×10^{-6}	85	0.44	2×10^{-3}	23

[a]We computed these masses in NLTE from the most recent ^{12}CO integrated line fluxes cited in papers below (assuming that it is optically thin), except for HD 21997 and HD 131835 where it is based on C^{18}O observations (see also Table 2).

[b]C I and O I are detected via absorption lines in the UV for 49 Ceti and their abundances are not well quantified (Roberge et al. 2014).

(1) Kral et al. (2016), (2) Hughes et al. (2008), (3) Riviere-Marichalar et al. (2014), (4) Kóspál et al. (2013), (5) Greaves et al. (2016), (6) Lieman-Sifry et al. (2016), (7) Moór et al. (2015, 2016), (8) Riviere-Marichalar et al. (2012), (9) Marino et al. (2016).

velocity H I component (presumably falling on to the star) was detected recently with the HST/COS around β Pic (Wilson et al. 2017). All these observations need to be understood within the framework of a self-consistent model. Models of the emission of the gas around main sequence stars have been developed, but gas radial profiles were not derived self-consistently and often assumed to be Gaussian (e.g. Zagorovsky, Brandeker & Wu 2010) or not to be depleted in hydrogen compared to solar (as expected in debris discs, e.g. Gorti & Hollenbach 2004) or both (e.g. Kamp & Bertoldi 2000).

One self-consistent model has been proposed in Kral et al. (2016, KWC16) that can explain gas observations around β Pictoris. It proposes that CO gas is released from solid volatile-rich bodies orbiting in a debris belt as first proposed by Moór et al. (2011); Zuckerman & Song (2012), and verified by Dent et al. (2014); Matrà et al. (2017). CO is then photodissociated quickly and produces atomic carbon and oxygen gas that evolves by viscous spreading, parametrized with an α viscosity, resulting in an accretion disc inside the parent belt and a decretion disc outside. A steady state is rapidly reached (on a viscous time-scale), meaning that it is unlikely that we observe a system in a transient phase. The α viscosity could be provided by the magneto-rotational instability (MRI) as presented in Kral & Latter (2016). Gas temperature, ionization state and population levels are computed using the photodissociation region model CLOUDY at each time-step (Ferland et al. 2013).

This model is generic and could apply to all debris discs as long as they are made up of volatile-rich bodies and their CO content is released as gas as they are ground down within a steady-state collisional cascade as proposed in Matrà et al. (2015). To apply the KWC16 model to a given system, we assume that the CO released is a proportion γ of the mass lost through the collisional cascade. That mass-loss rate can be determined from the fractional luminosity of the debris disc L_{IR}/L_* and its temperature from which the planetesimal belt location R_0 can be determined. These combine to give the CO input rate of $\dot{M}_{CO}$, which is one of the parameters in the KWC16 model, along with R_0, the α viscosity, the amount of radiation coming from the central star (L_*) and the interstellar radiation field (L_{IRF}) as well as the distance to Earth d. That model can then provide as an output the radial structure of the atomic gas disc in terms of density, temperature, ionization fraction for differ-

ent elements, line fluxes and make predictions/produce synthetic images for observations with ALMA or any other instruments.

In this paper, we will provide a semi-analytical model (simpler than the complex numerical model described above) to model secondary gas in debris discs and apply it to a large sample of debris disc systems in order to predict the abundance and detectability of CO, C I, C II and O I for each system. Previous observations, both detections and non-detections, will provide tests of these predictions, and allow us to assess whether the model can be used as a reliable predictor for unobserved systems.

We assume γ, α and L_{IRF} are same for all stars (we take the local interstellar radiation field (IRF) derived by Draine 2011), in which case the detectability of gas in the model depends only on R_0, $\dot{M}_{CO}$, L_* and d. We will explain which parts of this parameter space should be preferentially observed when trying to detect CO, C I, C II or O I with different instruments. This will give a general understanding of gas observations in debris discs and is particularly well suited for planning mm-wave APEX/ALMA line observations and considering the science that could be done with future missions such as SPICA (Swinyard et al. 2009) or NASA's far-IR surveyor concept (FIRS, now called the Origins Survey Telescope) that may be built within the next 15 yr.

In Section 2, a summary of gas detections around nearby main-sequence stars is presented. In Section 3, we present CO abundance predictions for a large sample of debris discs and explain which systems are more likely to have CO detected. In Section 4, we present a similar analysis for C I and C II and go on with O I predictions in Section 5. We discuss our findings in Section 6 before concluding in Section 7.

2 GAS OBSERVATIONS IN DEBRIS DISCS

The number of debris disc systems with gas detected is growing and we now have 12 systems that can help us to understand the dynamics of this gas and its origin. These systems are presented in Table 1. Ten of them have CO detections, whilst two have C I detected, four have C II detected and three systems have O I detected. All of these systems are shown in Fig. 1 in a L_* versus R_0 diagram (see Table 1 to find the values used and their references).
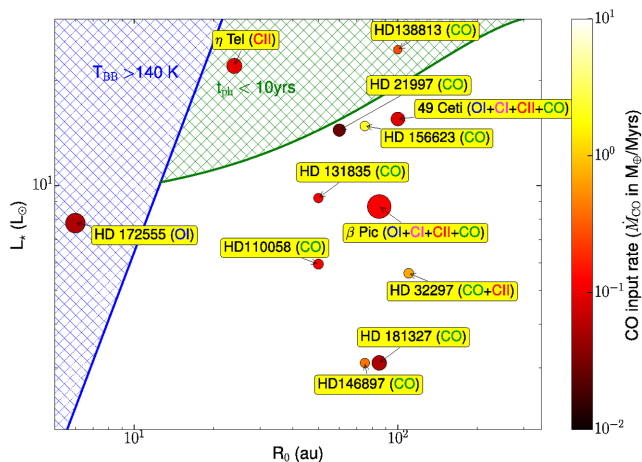
Figure 1. L_* versus R_0 for all discs with gas detected (see Table 1). The point sizes are inversely proportional to distance to Earth and the colour bar indicates CO input rates deduced from our model. The blue line represents a blackbody temperature of 140 K and the green line a photodissociation time-scale of 10 yr.

Table 2. NLTE calculations of CO masses from observations (optically thin assumption). We indicate as a footnote where the line fluxes were taken from. The second column provides the assumed electron density (computed from the model presented in this paper) when computing the CO mass.

Star's name	CO mass ($M_\oplus$)	Electron density (cm^{-3})
β Pic (1)	2.8×10^{-5}	240
49 Ceti (2)	1.4×10^{-4}	350
HD 21997 (3)	6.0×10^{-2}	510
HD 32297 (4)	1.3×10^{-3}	360
HD 110058 (5)	2.1×10^{-5}	500
HD 131835 (6)	6.0×10^{-2}	10
HD 138813 (5)	7.4×10^{-4}	1400
HD 146897 (5)	2.1×10^{-4}	5
HD 156623 (5)	2.0×10^{-3}	10
HD 181327 (7)	1.8×10^{-6}	130

(1) Matrà et al. (2017), (2) Hughes et al. (2008), (3) Kóspál et al. (2013), (4) Greaves et al. (2016), (5) Lieman-Sifry et al. (2016), (6) http://www.eso.org/sci/meetings/2016/Planet-Formation2016/Contributions/Oral/planets2016-MoorA.pdf, (7) Marino et al. (2016).

In this plot, we show the four fundamental parameters that matter in this study: R_0 and L_* (the x- and y-axes), $\dot{M}_{CO}$[1] (the point colour) and d (the point size). On the plot, one can see where the 12 systems lie, and we annotate their names, as well as the elements that have been detected so far (we omit metals as they are not expected to make up the bulk of the gas, Fernández et al. 2006). We overlay a blue line showing a blackbody temperature of 140 K. For CO adsorbed on amorphous H_2O, this is the temperature above which CO cannot be trapped in ices (under laboratory conditions, Collings et al. 2003). Any systems to the left of this line should not be able to retain any CO on grains (if no refractories are present to hold CO). A photodissociation time-scale of 10 yr is shown by the green line. If only the IRF were to be present (no central star or shielding), the photodissociation time-scale would be equal to ~120 yr (Visser, van Dishoeck & Black 2009). Systems that are above the green line are sufficiently luminous that the central star's radiation will act to significantly decrease this time-scale. It is thus unlikely to detect CO far above this green line for reasonable production rates.

The C II and O I fine structure lines have been detected with *Herschel* thanks to the GASPS programme, which used PACS to survey a small sample of debris discs (Dent et al. 2013; Riviere-Marichalar et al. 2014). Also, HIFI high spectral resolution data have been used for probing the C II location (and potential asymmetries) around β Pic (Cataldi et al. 2014). Of the systems with CO detected, 9 out of 10 have also been observed and detected with ALMA (see Table 2 to see the calculated CO masses from line fluxes). We included the four new CO ALMA detections by Lieman-Sifry et al. (2016), HD 138813, HD 146897, HD 110058 and HD 156623 (references are listed in Table 1). We do not include the recent tentative detection of CO in η Corvi by Marino et al. (2017), as the CO detection is not co-located with its debris belt and the gas release mechanism may be different than proposed in this paper.

In Fig. 1 and Table 1, one can notice several trends. Most gas detections are around A stars (only HD 181327 and HD 146897 are F stars). Also, all systems have high fractional luminosities; greater than 5×10^{-4}. Moreover, all the detections are for young systems

that are less than 45 Myr old.[2] In terms of the gaseous species detected, CO is almost always detected (10/12). For one system, C II is detected without CO (η Tel), and for another, O I is the only element detected (HD 172555). These two systems are located in the green and blue hatched areas, respectively, which could potentially explain a lack of CO detections so far (see Sections 3.1 and 3.5.3 for a more thorough explanation). We also note that there is an O I detection around HD 98800 (member of TW Hydrae association, Riviere-Marichalar et al. 2013) but we do not include this system as it might still be in an early pre-debris disc stage. All of the CO detections are for systems with debris belts located beyond 50 au.

Could these main trends be explained within the framework presented in KWC16? The remainder of this paper tackles this question. We first present the part of the semi-analytical model that computes CO mass predictions from the parameters of the dust belt and all the results we get for CO in Section 3. We then present the rest of the semi-analytical model to be able to get C I, C II predictions in Section 4 and later O I predictions in Section 5. We show that it is indeed possible to explain all the main trends presented above and henceforth give some predictions for debris disc systems without gas detected so far.

3 UNDERSTANDING CO

In this section, we explain why CO has been detected only around 10 main-sequence stars so far. To do so, we use our model to make predictions for the CO mass around many debris discs under the assumption that the dust is created in the destruction of volatile-rich planetesimals, a process that also releases CO gas (Zuckerman & Song 2012; Matrà et al. 2015). We then compare these predictions to APEX and ALMA mass detection limits to assess the detectability of each system. We then make predictions of CO detectability around a large number of debris disc host stars and provide the most promising targets to observe in the near future. We also identify what

---

[1] Computed with equation (2).

[2] We note that the age of HD 32297 is not well constrained but is likely ~30 Myr or younger (Kalas 2005).

determines the abundance of CO in any system. We show how observations give us a way to access the CO content of planetesimals, from which the observed CO is released (Matrà et al. 2015, 2017; Marino et al. 2016).

3.1 First check: solid body temperature and photodissociation time-scale

Fig. 1 gives some first insights on the systems in which CO is most likely to be detected. If the system is located in the blue hatched area, all CO has likely been lost already as it is released from icy grains above $T \sim 140$ K. This conclusion assumes that there are no refractories and no CO hidden in the core of big rocky bodies (the blue line assumes that grains radiate like black bodies). The only possibility to have CO in this region in a secondary scenario would be if there is enough CO (or C I, Matrà et al. 2017) to shield the radiation coming from both the star and IRF, but this requires a substantial amount (Matrà et al. 2017). This explains naturally why we do not expect CO to be detected around HD 172555 but we note that if the disc is twice as large as assumed here and/or that CO is hidden inside rocky bodies and released when they collide, it would be possible for CO to be present.

Also, it is less likely to find CO in the green hatched area as the photodissociation time-scale is smaller than 10 yr [calculated with equation (6), assuming no shielding] in this region and can reach very low values. This is a natural explanation for the lack of CO detection around η Tel so far. Not accounted for in this explanation are the CO mass input rate $\dot{M}_{CO}$ and distance to Earth d, which we consider further below.

3.2 CO mass predictions

To predict the CO mass within debris disc systems, we make the assumption that gas is produced from debris created through the collisional cascade. The mass-loss rate can be worked out from Wyatt (2008) assuming a $q = -3.5$ standard size distribution (e.g. Kral, Thébault & Charnoz 2013). While producing debris through the collisional cascade, we assume that solid bodies are composed[3] of a certain amount of CO γ (typically equal to ~ 10 per cent in Solar system comets, Mumma & Charnley 2011) that is released through the mass-loss process. Solid bodies ground down into dust in the collisional cascade are removed by radiation pressure at a rate $\dot{M}_{loss}$. Unless volatiles remain in dust then the CO production rate should only depend on the rate of dust production. In terms of the parameter space we study in this paper, the mass-loss rate is equal to (Wyatt 2008)

$$\dot{M}_{loss} = \delta \left(\frac{L_{IR}}{L_\star} \right)^2 \left(\frac{L_\star}{L_\odot} \right)^{13/12} \left(\frac{R_0}{1\,au} \right)^{-1/3} M_\oplus\,Myr^{-1}, \quad (1)$$

where R_0 is the distance from the host star to the planetesimal belt (in au), L_* is the star's luminosity (in $L_\odot$) and δ equals $e^{5/3}(2700/\rho)/(2.4 \times 10^{-10} dr/r\, Q_D^{*\,5/6})$. L_{IR}/L_* is the fractional luminosity of the debris disc, e is the mean eccentricity of the parent belt planetesimals, dr is the belt width (in au), ρ their bulk density (in kg/ m^{-3}) and Q_D^* their collisional strength (in J kg^{-1}). For the purpose of this study, we use typical values (as in Wyatt 2008),

---

[3] Note that the CO_2 ice may also contribute to the observed CO gas mass (e.g. Marino et al. 2016), in which case this assumed CO+CO$_2$ fraction would be higher by at most a factor of a few, increasing the CO gas mass produced (this would only change γ by a few).

i.e. we fix $e = 0.05$, $dr/r = 0.5$, $\rho = 3000$ kg m^{-3}, $Q_D^* = 500$ J kg^{-1}, which gives $\delta = 2.9 \times 10^5$. We will study in Section 3.6 what change can result from varying these parameters. Therefore, the CO mass rate can be estimated as

$$\dot{M}_{CO} = \gamma \dot{M}_{loss}, \quad (2)$$

where γ needs to be of the order of a few per cent to fit the observed β Pic CO mass or the composition of Solar system comets. More precisely, we fix γ to 6 per cent, the upper limit found by Matrà et al. (2017) for β Pic (when taking into account that CO$_2$ dissociation can also contribute to observed CO). This is consistent with the composition of Solar system comets for which 2 per cent $< \gamma <$ 27 per cent (when also including CO$_2$ that can contribute to the observed CO, Mumma & Charnley 2011; Matrà et al. 2017).

To get the actual CO mass, one needs to know the photodissociation time-scale t_{ph}, which is directly proportional to the impinging UV radiation on the gas disc. The main contributors to UV photons are the central star and the IRF. The mean intensity field (in W m^{-2} Hz^{-1}) is defined as

$$J_\nu = \frac{1}{4\pi} \int_\Omega I_\nu\,d\Omega, \quad (3)$$

where the intensity I_ν is the sum of the stellar I_* and IRF I_{IRF} intensities, and is integrated over the solid angle Ω subtended by its source. We use Castelli & Kurucz (2004) stellar spectra for I_* and the Draine IRF for I_{IRF} (Draine 2011).

Also, we take into account any attenuation of the flux coming from the star and IRF. When CO photodissociates, it creates atomic carbon and oxygen that spread all the way to the star. C I will photoionize by absorbing strong UV photons with energies greater than 11.26 eV (the ionization potential of C I). This will attenuate the UV flux impinging on to CO and reduce the CO photodissociation efficiency. We take into account the attenuation in the radial direction for radiation coming from the star but also in the vertical direction for the IRF. We note that we do not attenuate the photons with energies lower than 11.26 eV that may still participate in photodissociating CO. The new fluxes after attenuation are $I_* \exp(-\tau_r)$ and $I_{IRF} \exp(-\tau_\nu)$, where τ_r and τ_ν are the radial and vertical optical thicknesses to UV radiation defined as

$$\tau_r(R) = \sigma_{ion} \int_0^R n_{C\,I}(R')\,dR', \quad (4)$$

$$\tau_\nu(R) = \sigma_{ion} H(R)\, n_{C\,I}(R), \quad (5)$$

where $n_{C\,I}$ is the C I number density, σ_{ion} is the C I ionization cross-section and H is the height of the gas disc. Note that equations (4) and (5) require knowledge of the density of C I, the calculation of which is given in equations (14) and (15) of Section 4. For simplicity we first present here all the equations relating to CO, but note that the full model requires Section 4 to close the system of equations presented in this section. However, for most targets the CO photodissociation time-scale will in fact be dominated by the IRF (roughly outside of the green hatched area in Fig. 1) and can be assumed to be 120 yr so that equations (4) and (5) are not needed to compute this time-scale (see also KWC16).

The CO photodissociation time-scale can now be computed

$$t_{ph} = \left(\sum_{\nu = \nu_i} \frac{4\pi J_\nu}{h\nu} \sigma_\nu^{CO} \right)^{-1}, \quad (6)$$

where σ_ν^{CO} is the CO photodissociation cross-section per unit wavelength and ν_i are the frequencies of the lines that produce
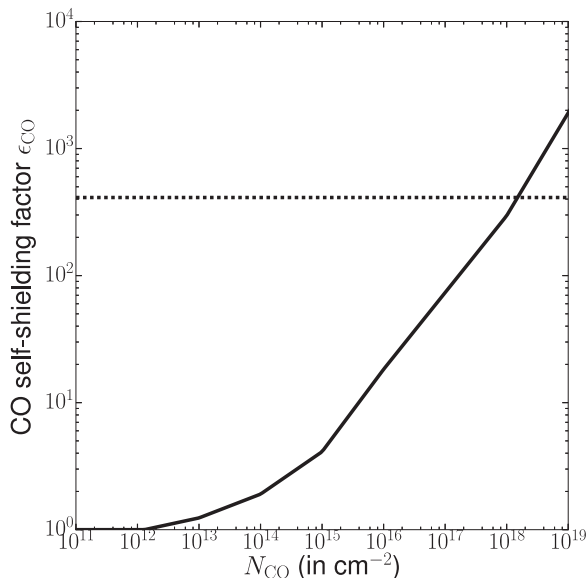
Figure 2. CO self-shield factor ϵ_{CO} versus CO column densities N_{CO} (in cm^{-2}) in the vertical direction (solid line). Values taken from Visser et al. (2009) and interpolated. The dashed line shows the maximum ϵ_{CO} that can be reached before photodissociation and viscous time-scales are equal, limiting the growth of ϵ_{CO} (see text for details).

photodissociation (mostly in the UV). The cross-sections are taken from van Hemert & van Dishoeck (2008).

Also, CO can self-shield against photodissociation if CO column densities in the vertical direction N_{CO} are $\gtrsim 10^{12}$ cm^{-2} (Visser et al. 2009). We define the self-shielding factor ϵ_{CO} as being equal to one when CO is optically thin to UV radiation and scales as shown on Fig. 2. For this calculation we assume that radiation is coming from all directions (from the IRF), that there is no H$_2$ around (as it is secondary gas), that $T_{ex} = 5$ K (small NLTE excitation temperature) and that the CO linewidth is 0.3 km s^{-1}. However, for a specific system, one can use different values for the linewidth or T_{ex} (see fig. 3 in Visser et al. 2009) to refine the estimate of ϵ_{CO}, which could vary by a factor ∼1.5. The total mass of CO in the disc at any one time M_{CO} (in M$_\oplus$) is calculated assuming a steady-state balance of gas production and loss so that

$$M_{CO} = \dot{M}_{CO} t_{ph} \epsilon_{CO}, \tag{7}$$

where the ϵ_{CO} factor accounts for the fact that the photodissociation time-scale from equation (6) must be increased by this factor due to self-shielding.

To check from which CO input rate self-shielding starts to matter, we plot M_{CO} as a function of $\dot{M}_{CO}$ in Fig. 3. We assume that $t_{ph} = 120$ yr and use different disc locations (from 0 to 50 au in dashed, from 50 to 100 au in solid and from 100 to 150 au in dotted) to convert from M_{CO} to N_{CO} (CO column density in the vertical direction) assuming a constant surface density in the disc. We iterate a couple of times as M_{CO} depends on N_{CO}, to reach convergence. For $\dot{M}_{CO} \gtrsim 5 \times 10^{-3}$ M$_\oplus$ Myr^{-1}, this effect will become important and the CO mass will increase steeply.

However, when CO self-shielding is important, CO photodissociation time-scales become very long and CO may have time to spread viscously, hence reducing the vertical column density. We also implement self-shielding into our model. To do so, we compute the viscous time-scale [see equation (10), where we assume $\alpha = 0.5$] for each system (depending on the location of the parent belt) and compare it to the CO photodissociation time-scale that
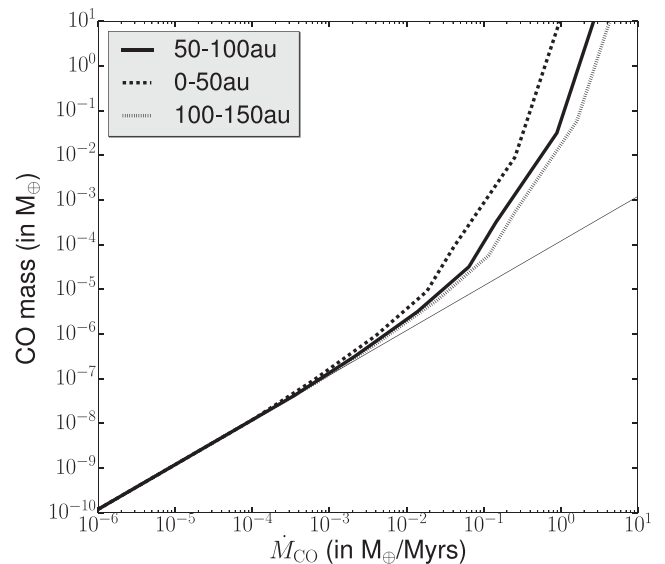
Figure 3. M_{CO} (in M$_\oplus$) versus $\dot{M}_{CO}$ (in M$_\oplus$ Myr^{-1}) taking into account CO self-shielding at high input rates. We compute the relation for three disc locations, from 0 to 50 au (dashed), from 50 to 100 au (solid) and from 100 to 150 au (dotted). The thin line shows the unshielded values.

includes self-shielding. If the latter becomes longer than the viscous time-scale, we assume no more shielding from CO and keep the value where these two time-scales are equal. We added a dashed line in Fig. 2 showing the maximum ϵ_{CO} that can be reached before photodissociation and viscous time-scales are equal assuming $R_0 = 85$ au, $T = 100$ K and $\alpha = 0.5$ around a β Pic-like star. Therefore, the CO self-shielding factor ϵ_{CO} cannot grow to extremely large values.

3.3 CO predictions compared with observations

We compare our CO predictions (small red points using equation 7) with observed CO masses (large green points) in Fig. 4 that are computed from the most recent CO integrated line fluxes in NLTE (see Table 1 for references). On this plot, the systems with CO detected are also labelled in blue. Other systems with gas detected but no CO are labelled in black. HR 4796 is labelled in orange for informational purposes, as it stands out in most of our predictions (except for CO), but no gas has been detected yet. Observed masses and predictions are linked by a thin black line for each individual system with CO detected. We also plot detection thresholds for APEX (orange) and ALMA (green) at different wavelengths to check for the detectability of each individual system but we detail that in a coming Section 3.5. For now, we focus on comparing mass predictions with observed masses.

Comparing the CO predictions with observations, we find that 7/10 systems have $0.1 \lesssim M_{observed}/M_{predicted} \lesssim 10$, and can be explained by a secondary gas model. Specifically, we find that β Pic, HD 181327, 49 Ceti, HD 32297, HD 110058, HD 156623 and HD 146897 can be well explained with secondary gas being produced within the debris belt already known to be present.

The 3/10 systems left have $M_{observed}/M_{predicted} > 100$, while others are generally within a factor 10 or slightly more. We check later (see Section 3.6) that varying the parameters of the model can account for a factor ∼10 difference but we consider systems that have $M_{observed}/M_{predicted} > 100$ as not possible to explain with a secondary gas model. Specifically, HD 21997, HD 131835 and
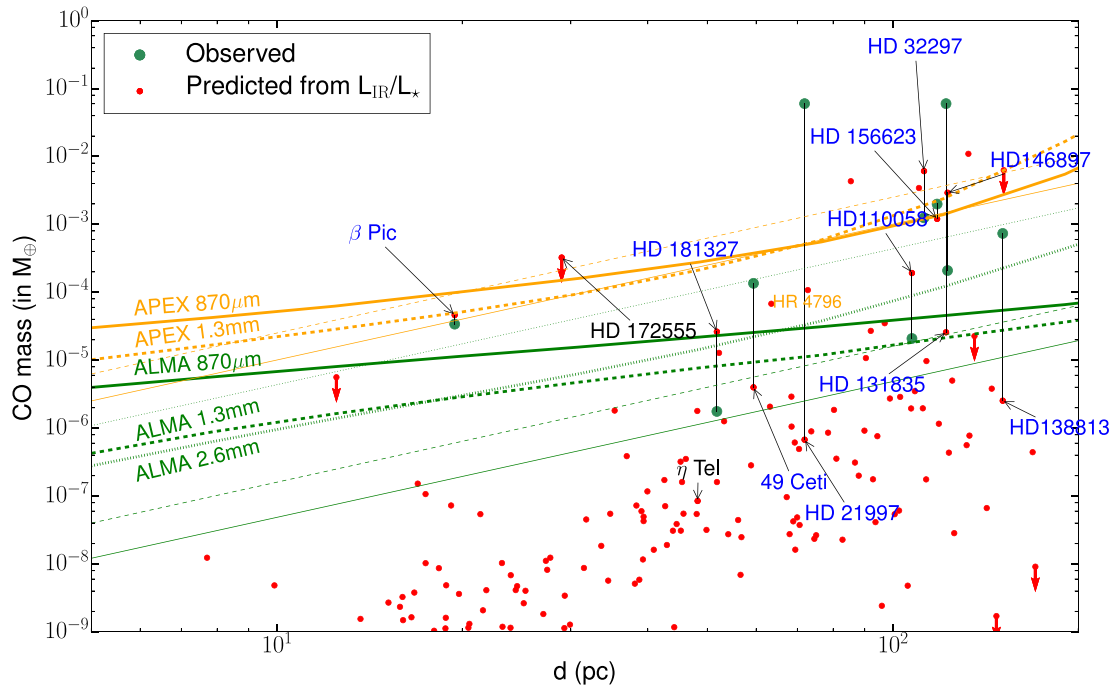
Figure 4. CO mass (in $M_\oplus$) as a function of distance to Earth (*d*). Planetary systems with gas detections are labelled with their names. If CO is detected, the label is in blue (black otherwise). The CO mass worked out from observations are shown as green points (see Table 2). The red points are predictions from our model. The red downward arrows show systems that are in the blue hatched area on Fig. 1, which cannot keep CO trapped on solid bodies. The thin orange lines show detection limits (assuming LTE and $T = 100$ K) with APEX at 1.3 mm and 870 μm (5σ in 1 h) and the thin green lines are for ALMA at the same wavelengths and 2.6 mm. We also compute the detection thresholds in NLTE, assuming an ionization fraction of 0.1 and $R_0 = 85$ au. The corresponding thick lines are in orange for APEX and green for ALMA and we keep the same line style for the different wavelengths.

HD 138813 are in this category. We note for instance that for HD 21997, for which the CO mass is relatively well known (thanks to the detection of an optically thin $C^{18}O$ line), the 5 orders of magnitude that separate the observation from our prediction will never be accounted for by our model. This reinforces the conclusion of Kóspál et al. (2013), who suggested that CO observations in this system can only be explained if the CO is of primordial origin. Thus, our model can also be used to identify systems that show anomalous behaviour when predictions do not match observations by orders of magnitude. For these systems, it may well indicate that they are of primordial origin.

Our model also finds that the predicted CO mass around η Tel is well below the predictions for systems where CO gas is detected. This is owing to the early stellar type (A0V) of η Tel, which reduces the CO photodissociation time-scale to a small value so that CO cannot accumulate in this system. This may explain the non-detection of CO in this system so far (see Section 3.5.3).

We also find that the CO mass in HD 172555 is predicted to be relatively high ($\sim 3 \times 10^{-4}$ $M_\oplus$) possibly at a detectable level. However, as the debris belt in this system is very close in, it might be optically thick and the line flux not detectable with APEX (see Section 3.5.3). Also, as explained in Section 3.1, it may be that grains in this system are just too warm (in the blue hatched area in Fig. 1) to retain any CO.

Our simple analytical model is thus able to reproduce CO observations (within uncertainties, see Section 3.6) for these specific systems and to flag anomalous systems which may be of primordial origin or have a secondary origin that fails to be modelled by the gas production mechanism assumed in this paper.

The variations between our predictions and observations were expected as we do not fit our model to the observations but rather

use fiducial values to see if the model reproduces the bulk of observations. For instance, we assumed that $\gamma = 6$ per cent of dust is converted into CO (as found for β Pic Matrà et al. 2017). This value might vary from one system to another and could potentially explain differences between some observed values and our predictions. For example, γ may vary with age as the more CO is depleted from grains, the less is exposed and the less comes off grains. γ also varies with initial composition, which depends on initial abundances in the extra-solar nebula in which grains formed, and depends also on planetesimal formation mechanisms. We note that gas detections provide a way to get back to the value of γ and then to the amount of CO in planetesimals.

3.4 Model predictions for a large sample of debris disc stars

We selected a sample of 189 debris disc host stars to determine which of these is predicted to have CO at a detectable level according to our model. The goal of our star selection process is to choose any star for which gas is likely to be detectable. So the nearby stars were included as they are close, and the bright systems because they are still potentially detectable [as $\dot{M}_{CO} \propto (L_{IR}/L_\star)^2$] despite being farther away. We assume the same fiducial parameters as in Section 3.3 to compute CO masses. These systems without gas detected are also shown as red points in Fig. 4 but they are not labelled (except for HR 4796). If the systems lie in the blue hatched area in Fig. 1 (i.e. the blackbody temperature of grains is greater than 140 K), we use red downward arrows as CO masses predicted are then only upper limits. In these cases, we do not necessarily expect to be able to detect CO.

The parameters assumed for the sample of stars can be found in Table C1. Most debris disc systems in our sample are not spatially

resolved and we cannot measure R_0 (the planetesimal belt location) directly from images. Rather, for this sample, R_0 comes from an SED fit of each individual spectrum. For the parent belt radius, we do not use the blackbody radius, which is always underestimated but rather use equation 8 in Pawellek & Krivov (2015) to correct this radius (assuming a composition of 50 per cent ice and 50 per cent astrosilicate, see their table 4).

We see that the predicted CO masses for $\sim$20 stars in this sample are comparable to the level of observed CO masses in other systems. Other stars from the sample have lower CO masses that according to our model should not be detectable with current instruments. We will study in more detail their detectability in the next section.

3.5 Detection thresholds for APEX and ALMA

In this section, we first describe in Section 3.5.1 how we computed the APEX/ALMA detection thresholds in Fig. 4. In Section 3.5.2, we then explain how we compute flux predictions from our mass predictions. We can then assess in Section 3.5.3 the detectability of the CO mass predicted for each system. In Section 3.5.4, we quantify the location of the LTE/NLTE transition. In Section 3.5.5, we explain in more detail the NLTE calculations used throughout the paper and describe how the NLTE regime varies compared to LTE. Finally, in Section 3.5.6, we explain how we compute the optical thickness of CO transitions.

3.5.1 Detection threshold calculation

To assess the detectability of each system in Fig. 4, we compute the detection thresholds with APEX (orange lines) and ALMA (green lines), assuming gas both in LTE (thin lines, see Section 3.5.4) and NLTE (thick lines, see Section 3.5.5). While NLTE provides the most accurate estimate of the line fluxes, LTE might be a valid approximation in certain regions of parameter space and is much simpler to calculate. Thus, we plot both to emphasize their differences (see Matrà et al. 2015).

For an optically thin line, the integrated line flux seen at Earth is

$$F_{u,l} = \frac{h\nu_{u,l}A_{u,l}x_u M}{4\pi d^2 m}, \tag{8}$$

where $A_{u,l}$ is the Einstein A coefficient for spontaneous emission, $\nu_{u,l}$ is the frequency of the transition and x_u is the fraction of molecules that are in the upper energy level u, M is the total mass and m is the mass of the studied molecule (or atom). We assume a typical gas temperature of 100 K and show assumed sensitivities (5σ in 1 h from the APEX and ALMA online calculators) in Table 3. The assumed PWV and elevation are given in the description of Table 3. The sensitivity is, here, independent of baseline configuration as we assumed that the gas discs would be unresolved, which yields maximum detectability. Using a Boltzmann distribution for the LTE case (thin orange and green lines) or solving the full statistical equilibrium (NLTE, thick orange and green lines), one can find the total number of CO molecules (or CO mass) that would create a certain flux at Earth.

If the LTE approximation is valid, Fig. 4 shows that for a gas temperature of 100 K, the 870 µm transition is more sensitive than the 1.3 and 2.6 mm transitions (but this changes in NLTE) and the ALMA detection threshold is better than APEX by 2 orders of magnitude. However, for most debris disc systems, CO is likely out of LTE (Matrà et al. 2015). In this case, detection limits depend on the electron density (which can be computed from our model, see Section 4) and do not simply scale as d^2 (see thick lines). Also,

Table 3. Instrument sensitivities to reach 5σ in 1 h on source (overhead excluded) at $45°$ elevation assuming unresolved gas discs. We assumed a PWV of 2 mm for CO observations and 0.5 mm for C I. We used 40 antennas for ALMA. For species observed with *Herschel*, we assumed the typical sensitivities reached by real observations (Riviere-Marichalar et al. 2014). For SPICA and for FIRS, the sensitivities are taken from the SPICA and FIR surveyor documentations.

Instrument	Line	Sensitivity (W m^{-2})
APEX	CO (1.3 mm)	3.3×10^{-20}
	CO (870 µm)	8.5×10^{-20}
	C I (610 µm)	3.9×10^{-19}
	C I (370 µm)	1.2×10^{-18}
ALMA	CO (2.6 mm)	2.0×10^{-22}
	CO (1.3 mm)	2.1×10^{-22}
	CO (870 µm)	4.1×10^{-22}
	C I (610 µm)	2.5×10^{-21}
	C I (370 µm)	7.9×10^{-21}
Herschel/PACS	C II (158 µm)	8×10^{-18}
	O I (63 µm)	6×10^{-18}
SPICA/SAFARI	C II (158 µm)	3×10^{-19}
	O I (63 µm)	3×10^{-19}
FIRS (10 m)	C II (158 µm)	1.5×10^{-21}
	O I (63 µm)	1.5×10^{-21}

Table 4. List of ALMA promising targets to look for CO and their predicted masses and fluxes at 1.3 mm and 870 µm.

Star's name	CO mass ($M_\oplus$)	$F_{CO\ 1.3\ mm}$ (W m^{-2})	$F_{CO\ 870\ µm}$ (W m^{-2})
HR 4796	1.1×10^{-04}	3.8×10^{-21}	1.4×10^{-20}
HD 15745	6.8×10^{-05}	2.1×10^{-21}	2.5×10^{-21}
HD 172555	3.2×10^{-04}	1.9×10^{-21}	3.2×10^{-21}
HD 114082	4.3×10^{-03}	1.2×10^{-21}	1.9×10^{-21}
HD 191089	1.3×10^{-05}	1.1×10^{-21}	1.1×10^{-21}
HD 129590	1.1×10^{-02}	9.9×10^{-22}	1.6×10^{-21}
HD 117214	3.4×10^{-03}	9.2×10^{-22}	1.6×10^{-21}
HD 106906	2.7×10^{-05}	6.9×10^{-22}	7.8×10^{-22}
HD 69830	5.6×10^{-06}	4.6×10^{-22}	9.2×10^{-22}
HD 121191	6.3×10^{-03}	3.3×10^{-22}	8.7×10^{-22}
HD 95086	1.1×10^{-05}	2.2×10^{-22}	8.4×10^{-23}
HD 143675	9.7×10^{-06}	1.5×10^{-22}	2.3×10^{-22}
HD 61005	1.8×10^{-06}	1.4×10^{-22}	2.2×10^{-23}
HD 169666	1.3×10^{-06}	1.3×10^{-22}	2.9×10^{-22}
HD 221853	2.9×10^{-06}	1.2×10^{-22}	5.0×10^{-23}

for the NLTE detection thresholds, we take account of the optical thickness of lines as explained in Section 3.5.6.

3.5.2 Flux predictions

In Table 4, we provide mass and flux predictions for the targets with the largest predicted CO fluxes (and later in Table C2 for all our targets). We use the CO NLTE code developed in Matrà et al. (2015) to convert from a given CO mass (outcome of our model) to a flux observed from Earth. To do so, we must provide to the code the amount of radiation seen by the gas. When modelling low rotational transitions of CO, their excitation is likely to be dominated by the cosmic microwave background (CMB, see Matrà et al. 2015) and our conversion will be accurate. We also account for the optical thickness of lines along the line of sight to Earth in our flux calculations using the method described in Section 3.5.6.

When making predictions for C I, C II and O I masses, the conversion to fluxes is more complicated (see Section 4.1).

3.5.3 Detectability of the specific sources used in this paper

We can now look at the relative position of our CO mass predictions against the detection thresholds in Fig. 4. Red points need to be above the ALMA NLTE detection threshold for a given transition to be detected at $>5\sigma$ within 1 h. We note that the NLTE lines assume a certain electron density (computed assuming a carbon ionization fraction equal to 0.1 and that $R_0 = 85$ au, KWC16) so these lines can move up or down if the electron density is smaller or higher, respectively (unless the lines are in a purely radiative regime where only the CMB excites the lines). That is why we leave the LTE detection thresholds (best case scenario) as a guide to check the range of detection thresholds that could be spanned if more colliders were around.

We find that systems that are predicted to be detectable by APEX are also close to being optically thick. Both the low sensitivity and high optical thickness explains the difficulty to detect CO with single-dish aperture telescopes.

Our model explains why β Pic was not detected by single dish telescopes (Dent et al. 1995; Liseau & Artymowicz 1998) as it lies below the APEX detection limits. CO was detected with APEX around HD 21997 (Moór et al. 2011) and HD 131835 (Moór et al. 2015) and with the JCMT around HD 32297 (Greaves et al. 2016). We predict that it should be the case for HD 32297. However, HD 21997 and HD 131835 are not predicted to be detectable and yet CO was detected. This is because they have larger masses than predicted likely because the CO is primordial.

We can now check whether the CO APEX non-detection in η Tel (Moór et al. 2015) is predicted by our model. Our prediction lies well below the APEX detection threshold. Even ALMA should not be able to detect CO as there is roughly 2 orders of magnitude between the 1.3 mm NLTE limit and the CO mass inferred by our model.

Looking at Table 4, we see that if CO can remain on grains, HD 172555 is one of the most promising targets to look for CO. Though, we note that our flux prediction is still lower (by a factor 5) than the APEX upper limit of 1.6×10^{-20} W m^{-2} (Moór et al. 2011). This is because the CO in this system is very close in and so optically thick (see Section 3.5.6 for more details on how the optical thickness was computed).

From our mass predictions, ~ 3 more systems (HD 114082, HD 117214 and HD 129590) are above the APEX detection threshold plotted in Fig. 4. However, that detection threshold was computed for a system at 85 au with an ionization fraction of 0.1, and computing the fluxes of these three systems at the correct radius, we find that their CO is optically thick and so not detectable with APEX. These stars are part of the Sco-Cen association and were observed recently with ALMA, but this led to no detections (Lieman-Sifry et al. 2016). These CO observations reached a sensitivity of $\sim 5 \times 10^{-22}$ W m^{-2} (5σ) for these three systems which is still a factor 2 below our predictions. We note that for these three systems, CO self-shielding is high but limited by viscous spreading of CO.

The NLTE detection thresholds for ALMA are at least 10 times more sensitive in mass than for APEX at a given distance d. This is not only due to the different instrument sensitivities but also to the electron density and τ_ν being smaller for systems that lie close to the ALMA detection thresholds compared to systems that are close

to the APEX thresholds. Our model predicts that ~ 15 systems from the sample lie above or close to the ALMA detection thresholds. Furthermore, the NLTE lines could be closer to the LTE regime for systems that are closer in than $R_0 = 85$ au, due to the higher electron density. Therefore, systems under the NLTE lines could still be detectable. We provide a list of the 15 most promising systems in Table 4 for which we predict CO could be detected with ALMA. For instance, we see that the CO around HR 4796A (labelled in orange) as well as HD 15745 may be detectable with ALMA.

3.5.4 Validity of LTE

To understand when CO is out of LTE, we computed the CO-electron critical density (for the different transitions) for an optically thin system assuming a two level system. This critical density is simply equal to A/γ_c, where A is the Einstein coefficient of the considered transition and γ_c the collisional rate coefficient (from upper to lower level, taken from Dickinson & Richards 1975). We can compute the CO mass $M_{CO, LTE}$ required by our model to create an electron density equal to this critical density. To compute the LTE limit, we further assume that all electrons come from C I photoionization, that the ionization fraction equals 0.1, that $R_0 = 85$ au and that the photodissociation time-scale is ~ 120 yr (and then use equation (14) derived later).

We find that the LTE limit (for the 870 μm transition, solid line) is located at $M_{CO} \sim 5 \times 10^{-4}$ M$_\oplus$ in Fig. 4, above which LTE likely applies (i.e. in almost no systems). Note that $M_{CO,LTE}$ scales as $T_{gas}^{3/2} t_{ph} f^{-1} L_\star^{-1/4} R_0^3$ and so the LTE limit is different for different systems. For instance, for a system with a debris belt at $R_0 = 10$ au, the LTE limit might be expected to go down by a factor 600. However, for such close-in systems, the ionization fraction would also drop (because of higher C I densities closer in). So overall, our prediction that almost all debris discs with gas are not in LTE for CO is generally true, reinforcing the conclusion of Matrà et al. (2015), and motivating the need for line ratios to test if the gas has an exocometary origin (Matrà et al. 2017).

3.5.5 Calculations in non-LTE

We here give more details on how we computed the NLTE detection thresholds but also give the reader a feel for the differences it implies compared to the LTE regime. We used the code presented in Matrà et al. (2015) to solve the statistical equilibrium and work out the population of rotational levels. For the low CO transitions considered here, it was shown in Matrà et al. (2015) that for β Pic, the excitation will be dominated by the CMB radiation rather than dust emission and stellar radiation (see Fig. B1). The same also applies to other systems as β Pic is among the most luminous debris discs and the CMB is even more dominant in less dusty systems.

Looking at the differences with LTE is instructive. The APEX sensitivity lines are close to LTE at larger distances. However, there are not enough colliders (assumed to be electrons) to be in full LTE even though the lines are above the LTE limit derived above (located at $M_{CO} \sim 5 \times 10^{-4}$ M$_\oplus$). This is owing to the two population level assumption made when computing the LTE limit. Also, for almost all distances, the APEX 1.3 mm transition in NLTE is actually more sensitive than LTE. This is expected as for these given higher masses or electron densities (10–10^4 cm^{-3}), the CMB excites the 1.3 mm transition more than collisions do (see Fig. 5). Also, the 2.6 mm transition is much more excited in NLTE for electron densities smaller than $\sim 10^5$ cm^{-3} (see Fig. 5). This was already shown in
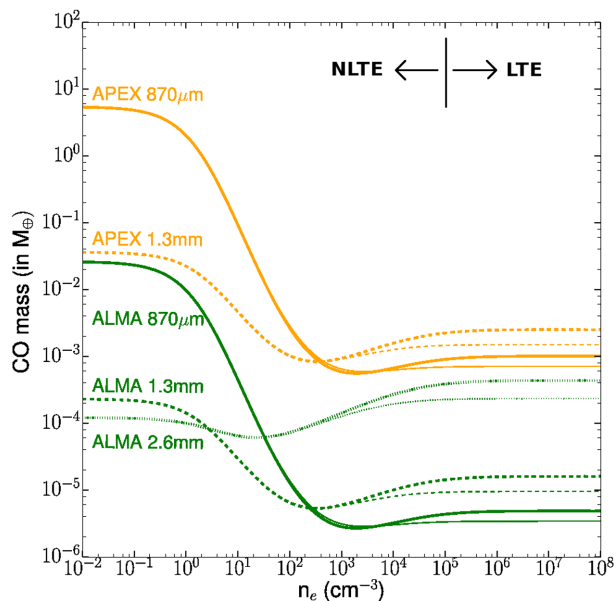
Figure 5. Mass in CO (in $M_\oplus$) required to result in a predicted line flux equal to the sensitivity threshold of APEX (in orange) and ALMA (in green) as a function of electron density (in cm^{-3}). The assumed sensitivities for different transitions that can be found in Table 3. Thinner lines are for $T = 50$ K and thicker lines for $T = 100$ K. The black vertical line shows the transition between the LTE and NLTE regimes.

Matrà et al. (2015) in their fig. 6. Therefore, quite strikingly, for very low electron densities, ALMA is more sensitive in the 2.6 mm transition rather than the 870 μm.

We also notice that in NLTE, the 1.3 mm transition is more sensitive than the 870 μm transition for lower masses (unlike the LTE case). This is also expected from Fig. 5, which shows the mass needed to reproduce a given flux as a function of the electron density. Indeed, for electron densities $\lesssim 5 \times 10^2$ cm^{-3}, the 1.3 mm transition needs less CO mass than the 870 μm transition and is thus more sensitive. Hence, when observing a particular system, one should consider carefully which transition is more suited.

3.5.6 Optical thickness of lines

When considering detectability, one has to take into account the optical thickness of CO lines. An optically thick line will saturate and become harder to detect given its mass compared to an optically thin line. To estimate the optical thickness τ_ν for a given CO mass, we assume a rectangular line profile and use the τ_ν definition (Matrà et al. 2017)

$$\tau_\nu = \frac{h\nu_{ul}}{4\pi\Delta\nu}(x_l B_{lu} - x_u B_{ul})N, \tag{9}$$

where $\Delta\nu$ is the linewidth in Hz, x_u and x_l are the fractional populations of the upper and lower levels of the given transition, B_{lu} and B_{ul} are the Einstein B coefficients for the upward and downward transitions (that can be expressed as a function of the Einstein A coefficient) and N is the column density along the line of sight. We fix $\tau_\nu = 1$ and compute the column density N of CO needed to become optically thick. In order to do this, we assume a disc located between 70 and 100 au, with a constant surface density, and a constant scale height equal to $0.2R$ (as found for β Pic, Nilsson et al. 2012) and work out the CO mass needed to reproduce this column density along the densest line of sight for an edge-on con-

figuration. We choose the linewidth to be 2 km s^{-1}, which is close to the intrinsic linewidth found for β Pic (see Crawford et al. 1994; Cataldi et al. 2014). This linewidth is the combination of thermal and turbulent broadening. This $\tau_\nu = 1$ line will vary depending on the extension of the disc, its scale height, the linewidth and gas temperature. Also, we assumed LTE to compute the population levels. We can check a posteriori that the approximation works as we find that the $\tau_\nu = 1$ line for CO masses is $\sim 8 \times 10^{-4}$ $M_\oplus$, which is dense enough to be above the LTE threshold (see Section 3.5.4).

Thus, we are able to compute τ_ν for every given mass and transition in Fig. 4 and take the optical thickness into account when computing mass detection limits from the telescope flux sensitivities. We applied the correction when plotting the NLTE detection thresholds in Fig. 4, assuming that systems are edge-on, by applying a factor $\tau_\nu/(1 - e^{-\tau_\nu})$ to the previously computed mass detection limit. Therefore, when M_{CO} is much above the $\tau_\nu = 1$ limit, the mass detection limit at a given distance is increased by a factor τ_ν. One can see that our NLTE detection limits in Fig. 4 start increasing more steeply with distance when approaching CO masses of 10^{-3} $M_\oplus$ due to this reason, which hinders CO detections with APEX for targets at large distances. τ_ν is computed for every transition and the corrections are applied with the corresponding τ_ν. This is why the APEX 1.3 mm line starts steepening before the 870 μm line.

3.6 CO mass variation when changing parameters

Fig. 6 can be used to work out the effect of varying one parameter of the model while keeping others fixed. For each parameter, the fiducial values and range of variations used to make the plot are listed in Table 5. The downwards and upwards arrows in Fig. 6 show the sense of CO mass variation if a parameter is increased. The blue boxes are for parameters that can be deduced from observations. For those, the rate of variation will correspond to the error bars from observations. We assume that L_* is known within 10 per cent (Heiter et al. 2015), R_0 is computed from the SED (temperature) for the sample, and is known within a factor 2 (Pawellek & Krivov 2015). Also, if the SED has more than 2–3 far-IR detections (which is the case for the sample we use), the fractional luminosity is known within about 10 per cent (most discs in our sample are bright so have far-IR photometry with a signal-to-noise ratio >10, meaning that the disc temperature and normalization, and thus the fractional luminosity, are well constrained).

For the fawn boxes in Fig. 6, we vary the parameters over a larger region (see Table 5). Note that each parameter is varied across a reasonable range for the given parameter so that the planetesimal eccentricity varies by a factor 20, while L_* varies by 10 per cent and t_{ph} by 300 per cent (because of uncertainties on the IRF around these far-away discs). We assume a uniform distribution while varying each parameter. We then compute the result for each variation. Then, the box sizes show where 50 per cent of the distribution lies and the whiskers contain 95 per cent of the distribution. The red line shows the median of the distribution.

The parameters imposing the biggest variations (see equation 1) are the planetesimal eccentricity e, the width of the belt and the factor γ giving the composition of planetesimals. Thus, a factor ~ 10 variation can be explained if the parameter values are different from the fiducial values we picked. This can explain some discrepancies between our model predictions and the observations. A thorough study of each individual system would be needed to reduce these uncertainties but this is not the aim of this general study.
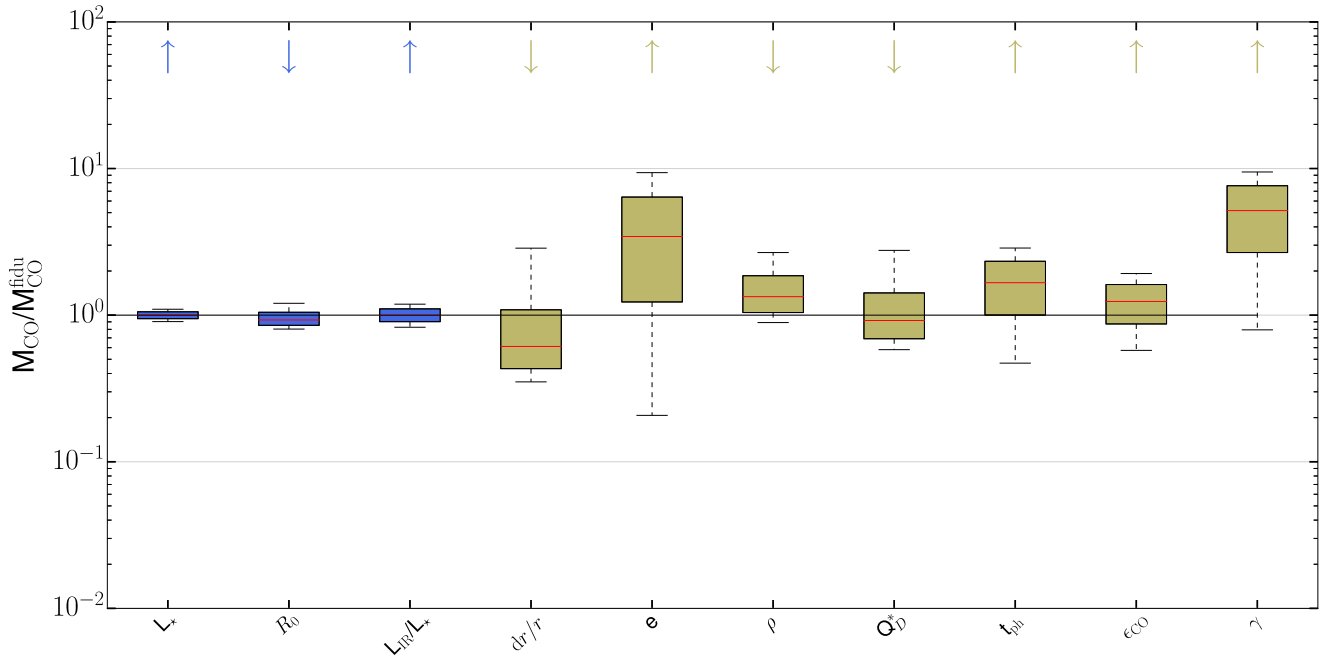
Figure 6. CO mass variation whilst varying parameters one by one. The fiducial values and amplitude of variations of the different parameters are given in Table 5. The blue boxes are for parameters where we have a good observational handle and only error bars on the predicted values are taken into account. For fawn boxes, there are more uncertainties and we allow for a large physical variation for each parameter. Box sizes show where 50 per cent of the distribution is located, while the whiskers contain 95 per cent of the distribution. The red line is the median value. We indicate with an upwards or downwards arrow the sense of variation for M_{CO} if a given parameter is increased.

Table 5. Parameters of the CO model that can be varied. We indicate the fiducial value picked for each parameter as well as a typical range of variations.

Parameters	Fiducial value	Range of variation
L_* ($L_\odot$)	10	10 per cent
R_0 (au)	85	Factor 2
L_{IR}/L_*	10^{-4}	10 per cent
dr/r	0.5	0.1–1.5
e	0.05	0.01–0.2
ρ (kg m^{-3})	3000	1000–3500
$Q_D^\star$ (J kg^{-1})	500	100–1000
t_{ph} (yr)	120	Factor 3
ϵ_{CO}	1	Factor 2
γ (in per cent)	6	2–60

3.7 CO succinct conclusion

To conclude, using a simple model with L_{IR}/L_*, R_0, L_* and d as free parameters, we are able to explain most CO observations to date. We also explain why CO was not easy to detect with single dish telescopes (e.g. Dent, Greaves & Coulson 2005; Moór et al. 2011; Hales et al. 2014; Moór et al. 2015; Greaves et al. 2016). Given a large sample of debris disc systems, we show that ALMA will still detect CO over the next few years but one expects integration times longer than 1 h to reach a large number of systems. In Fig. 1, we show the part of the L_*, R_0 parameter space that should be avoided when looking for CO, and in Fig. 4 we study the rest of the parameter space and give a way to calculate the predicted CO mass within each individual system and compare to detection thresholds. With our method, the whole parameter space is then studied and we show that the most important parameters (if one excludes the hatched

zones plotted in Fig. 1) are the fractional luminosities L_{IR}/L_* and the distance to Earth d that have a quadratic dependence on CO mass. One should therefore look for CO with ALMA by picking systems with large IR-excesses, close to Earth and having L_* small enough and R_0 large enough not to lie in the hatched exclusion areas in Fig. 1. We also show that the parameters that are not observable directly that matter the most are the dynamical excitation of the disc, γ and the belt width (see Fig. 6). The belt width is not known for unresolved debris discs. For systems that have their main belt resolved, the less extended, the better. The composition of planetesimals (γ) is also an important parameter as it provides the CO mass content in planetesimals.

4 UNDERSTANDING CARBON

In the same way as we calculated CO predictions from a simple analytical model, we will now do the same for carbon observations (C I and C II). To do so, we use the scenario presented in KWC16 where CO is input within the system and photodissociates quickly into carbon and oxygen, which viscously spreads. As deduced from β Pic observations, α, which parametrizes the viscous evolution, should be high and the corresponding viscous time-scale is $\sim 10^5$ yr (see KWC16). We will assume that $\alpha = 0.5$ throughout this paper, which sets the viscous time-scale

$$t_\nu = R_0^2 \Omega/(\alpha c_s^2), \tag{10}$$

where Ω is the orbital frequency and $c_s = \sqrt{R_g T/\mu}$, the sound speed fixed by the gas temperature T (both estimated at R_0), with R_g being the ideal gas constant and μ the mean molecular mass of the carbon + oxygen fluid (assumed to be 14). Assuming steady state,

one can then estimate the amount of carbon within each system from the CO mass, as follows:

$$M_{\mathrm{totC}} = 0.43 \times \dot{M}_{\mathrm{CO}} t_\nu, \tag{11}$$

where $0.43 = 12/28$ is the molar mass ratio between carbon and CO, and $\dot{M}_{\mathrm{CO}}$ is worked out using equation (2). Thus, we can already conclude from equation (1) that a high carbon mass is favoured by a high fractional luminosity, a dynamically hot belt, a high $L_\ast$ and a small belt width-to-distance ratio $\mathrm{d}r/r$. The blue hatched area in Fig. 1 should still be avoided as all CO should be removed rapidly and no replenishment is possible over time (unless carbon or oxygen is produced through other less volatile molecules). On the contrary, systems that have a high carbon mass can be located in the green hatched zone in Fig. 1 as at steady state the carbon mass does not depend on t_{ph}.

To compare our model to observations we must compute the carbon ionization fraction for each system to work out the C I and C II masses. To do so, we assume that the recombination rate R_{recomb} equals the ionization rate R_{ion}. The total recombination rate (in $\mathrm{m}^{-3}\,\mathrm{s}^{-1}$) is dominated by C II recombination and is equal to

$$R_{\mathrm{recomb}} = \alpha_{R_C}(T) n_{\mathrm{C\,II}} n_{\mathrm{e}}, \tag{12}$$

where $\alpha_{R_C}(T)$ is the recombination rate coefficient for C II that depends slightly on temperature and is taken from Badnell (2006). $n_{\mathrm{C\,II}}$ and n_{e} are the number densities of C II and electrons, respectively, which we assume are equal, as in our model we assume that electrons are only produced when C I photoionizes into C II. The photoionization rate for carbon is

$$R_{\mathrm{ion}} = n_{\mathrm{C\,I}} \int_{\nu_{\mathrm{ion}}}^{\infty} \frac{4\pi J_\nu}{h\nu} \sigma_{\mathrm{ion}}\,\mathrm{d}\nu, \tag{13}$$

where $n_{\mathrm{C\,I}}$ is the neutral carbon number density, $\nu_{\mathrm{ion}} = 11.26$ eV is the smallest energy that can ionize C I and σ_{ion} is the carbon ionization cross-section taken from van Hemert & van Dishoeck (2008). Also, at steady state as the gas disc is an accretion disc, the surface density $\Sigma = \dot{M}_{\mathrm{CO}}/(3\pi\nu') = 2\rho_{\mathrm{g}}H$, with ν' the gas disc viscosity and ρ_{g} the gas number density. To convert between Σ and the particle number density n, we use $n = \rho_{\mathrm{g}}/(\mu m_{\mathrm{p}})$ to find the carbon number density at steady state

$$n_C = \frac{0.43 \dot{M}_{\mathrm{CO}} \Omega^2}{3\pi \mu m_{\mathrm{p}} c_{\mathrm{s}}^3}, \tag{14}$$

where m_{p} is the proton mass and we assumed $\alpha = 0.5$. From this equation, one can compute the electron density anywhere in the system as $n_{\mathrm{e}} = f n_C$. One can solve for the carbon ionization fraction f by equating R_{ion} to R_{recomb} and using $f = n_{\mathrm{C\,II}}/(n_{\mathrm{C\,I}} + n_{\mathrm{C\,II}})$ to find that

$$f = \frac{-R_{\mathrm{ion}}^{*} + \sqrt{R_{\mathrm{ion}}^{*\,2} + 4 R_{\mathrm{ion}}^{*} n_C \alpha_{R_C}}}{2 n_C \alpha_{R_C}}, \tag{15}$$

where $R_{\mathrm{ion}}^{*} = R_{\mathrm{ion}}/n_{\mathrm{C\,I}}$, and $n_C = n_{\mathrm{C\,I}} + n_{\mathrm{C\,II}}$. Hence, the ionization fraction can be calculated knowing the radiation impinging on the disc J_ν and the carbon number density. There is also a slight temperature dependence through α_{R_C}.

We estimate the temperature T_{gas} at each location in the disc by equating cooling by the C II fine structure line and heating by C I photoionization and iterate a few times with the ionization fraction calculation until it converges. The calculations are described in Appendix A and we check that the analytical formulation reproduces well previous published numerical simulations (see Fig. A1) for the gas disc around β Pictoris (see KWC16).

We are now able to compute the C I mass $M_{\mathrm{totC}}(1 - f)$ and the C II mass $M_{\mathrm{totC}} f$ for any given system. f depends on R and is taken to be an average of the ionization fraction along R, by weighting with the surface density R-dependence. We thus find that $M_{\mathrm{C\,II}} \propto (L_{\mathrm{IR}}/L_\star)^{1/8} R_0^{1/2} \dot{M}_{\mathrm{CO}} T_{\mathrm{gas}}^{-1} f$, where T_{gas} is the gas temperature. As explained in the previous paragraph, we computed the temperature in the disc numerically but as a convenience for the reader, the following formula gives the C II mass (in $M_\oplus$) when assuming a power law for the gas temperature

$$M_{\mathrm{C\,II}} = \delta' \left(\frac{L_\star}{L_\odot}\right)^{1/8} \left(\frac{R_0}{1\,\mathrm{au}}\right)^{1/2+\zeta} \left(\frac{\dot{M}_{\mathrm{CO}}}{0.23\,M_\oplus\,\mathrm{Myr}^{-1}}\right) f, \tag{16}$$

where $\delta' = 0.024/(\alpha T_0 (R_{T_0}/1\,\mathrm{au})^\zeta)$. In this equation, the temperature profile is fixed to $T_{\mathrm{gas}} = T_0(R/R_{T_0})^{-\zeta}$, where ζ is taken to be 0.5 in most studies, and we assume $\alpha = 0.5$. Substituting $\dot{M}_{\mathrm{CO}}$ from equations (1) and (2), we find that $M_{\mathrm{C\,II}} \propto L_\star^{13/12} R_0^{1/6+\zeta}(L_{\mathrm{IR}}/L_\star)^{17/8} f$ for a fixed $\mathrm{d}r/r$.

Also, we can define the total C I mass with the same parameters using

$$M_{\mathrm{C\,I}} = M_{\mathrm{C\,II}} \frac{1 - f}{f}. \tag{17}$$

This set of equations will be used in the coming sections to predict the C II and C I abundances in different systems. They can also be used theoretically to understand the system's parameters that matter the most to optimize the chances of finding new systems with gas.

4.1 Flux predictions for atoms

When making predictions for C I, C II and O I masses, the conversion to fluxes is more complicated than with CO where the excitation is dominated by the CMB (see Section 3.5.2). Since these lines are at shorter wavelengths, the dust radiation field can become dominant (see Fig. B1). While the dust radiation field seen by the gas is not easy to assess, especially as most of our targets are unresolved, it is well known for β Pic. Thus, we use the same radiation field as found in Matrà et al. (in preparation) for that system. For other targets, we fit each SED individually and use the ratio of the dust fluxes at 158, 610 and 63 μm to those of β Pic to scale up or down the β Pic radiation field and so get predictions for the fluxes of each individual system for C II, C I and O I (see Appendix B). Note that we also take account of the optical thickness of each line in our flux calculations using the method described in Section 3.5.6.

4.2 C II model predictions and results

We start off by comparing our C II model predictions to *Herschel* observations. In Fig. 7, we plot our predictions of C II mass as a function of distance to the star. To do so, we use our analytical model using equation (11) to get the total carbon mass and equation (15) to get the ionization fraction and then compute $M_{\mathrm{C\,II}}$. The predicted C II masses are shown as red points in Fig. 7. We keep the same style as the CO plot (Fig. 4), i.e. systems with gas detected are labelled with their names. If in addition, they have C II detected, the label is blue (not black). NLTE detection thresholds are computed using the same code as described to compute CO population levels in NLTE (see Appendix B for details). We overplot the detection limits at 5σ in 1 h in both LTE (thin lines) and NLTE (thick lines) for *Herschel*/PACS (in red) where we assumed the typical sensitivity reached for non-detections (Riviere-Marichalar et al. 2014), for SPICA/SAFARI (in orange) and for a future far-IR mission (such as FIRS) with a 10 m aperture (in green) where the sensitivities
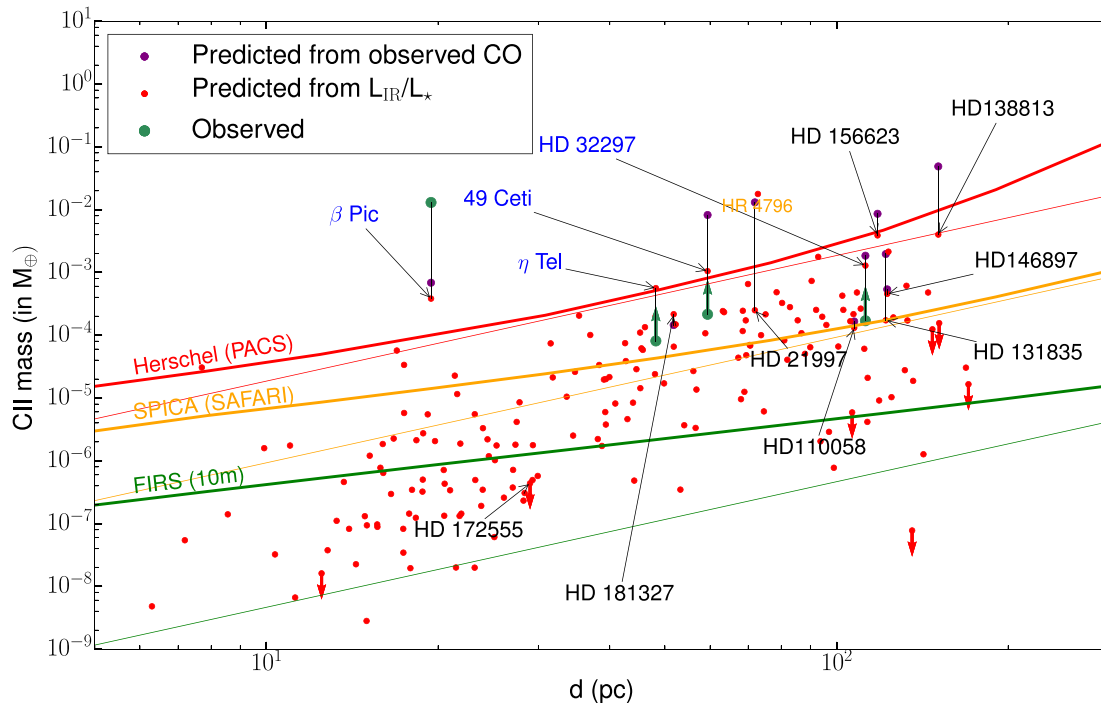
Figure 7. C II mass (in $M_\oplus$) as a function of distance to Earth (d). Planetary systems with gas detections are labelled with their names. If C II is detected, the label is in blue (black otherwise). The C II mass lower limits worked out from observations are shown as green arrows, and for β Pic we show the mass derived from *Herschel* observations using Kral et al. (2016) as a green point. The red points are predictions from our model. The red downward arrows show systems that are in the blue hatched area on Fig. 1, which cannot keep CO trapped on solid bodies. The purple points show predictions from our model when the observed CO mass is used rather than the CO mass predicted from L_{IR}/L_*. Detection limits at 5σ in 1 h are shown for *Herschel*/PACS (in red), SPICA/SAFARI (in orange) and FIRS (in green) for a 10 m aperture. The thin lines are for LTE calculations and thick lines for more realistic NLTE calculations (using the same assumptions as described in Section 3.5).

are taken from the SPICA and FIR surveyor documentation.[4] The assumed sensitivities are summarized in Table 3. We compute the electron density as a function of the C II mass (using equation 14) with our model to compute the NLTE lines.

We also compute the LTE limit in the same way as described in the previous section for CO. We find that the transition between LTE and NLTE is at $M_{C\,II} \sim 7 \times 10^{-5}\,M_\oplus$. Note that all the debris disc systems above the PACS detection threshold are most likely in LTE. The LTE *Herschel* detection threshold is, therefore, a good indicator of detectability unlike the case with CO.

We also compute when the C II line becomes optically thick for an edge-on configuration. We use the same assumptions as for CO. Most of our predictions lie below the $\tau_\nu = 1$ (edge-on) line located at $M_{C\,II} \sim 2 \times 10^{-3}\,M_\oplus$. Therefore, we do not predict C II gas discs to be highly optically thick. The NLTE lines are corrected for optical thickness (which is why the PACS sensitivity line steepens for large d). When the C II mass reaches $\sim 10^{-4}\,M_\oplus$, NLTE effects start affecting the *Herschel* and SPICA detection thresholds. New instruments as sensitive as FIRS will be able to detect gas discs in the NLTE regime.

Fig. 7 shows that our predictions for η Tel, 49 Ceti, HD 32297 and β Pic all lie above or close to the PACS detection threshold. The *Herschel* archive shows that these targets were observed for at least 1.2 h with PACS (HD 32997, which lies a bit below the threshold was observed for 2.6 h). Note that the LTE mass detection threshold is for a temperature of 100 K but scales as $T^{1/2}$.

For C II detections, only lower limits on C II masses can be calculated from observations (as the excitation temperature is not known), which are represented as green arrows in Fig. 7. Our predictions are all above these lower limits. For the C II mass in β Pic, our prediction is about 1 order of magnitude below that observed. This can be explained from KWC16, where it was found that the UV flux impinging on the disc should be higher than that assumed here to explain the C II observation. However, to be as general as possible in this study, we assume standard spectra for stars and a standard IRF. This illustrates that our predictions have roughly order of magnitude uncertainty.

In addition to using our CO predictions to compute the C II masses, we show the results when using the observed CO masses M_{COobs} as purple points. We can then calculate $\dot{M}_{CO}$ ($= M_{COobs}/(t_{ph}\epsilon_{CO})$) in equation (11) to make another prediction for C II. For most cases, a higher observed CO mass than predicted means a higher C II mass prediction. However, this is not straightforward for small CO mass variations (between the predicted and observed masses) as increasing the CO mass will also decrease the ionization fraction (due to a higher carbon mass), which might be stronger than the increase in carbon mass. Also, increasing the CO mass can create more self-shielding, reducing the CO input rate and hence the C II mass. Using these new predictions does not change our previous conclusion that the four systems with C II detected should have been detected. Three other systems, namely HD 21997, HD 138813 and HD 156623 cross the PACS detection threshold with these new predictions. However, as explained before, we cannot fit HD 21997 with a second generation scenario and this new prediction reinforces this idea as C II was not detected by *Herschel*.

Table 6. List of the promising C II targets and their predicted masses, fluxes and observed fluxes.

Star's name	C II mass ($M_\oplus$)	$F_{\text{C II 158 }\mu\text{m}}$ (W m^{-2})	$F_{\text{C II(obs) 158 }\mu\text{m}}$ (W m^{-2})
Fomalhaut A	3.1×10^{-05}	1.2×10^{-18}	$<2.2 \times 10^{-18\,a}$
HD 86087	1.8×10^{-03}	1.2×10^{-18}	–
HD 61005	2.0×10^{-04}	1.0×10^{-18}	–
HD 156623	3.9×10^{-03}	8.3×10^{-19}	–
HD 182681	6.5×10^{-04}	8.3×10^{-19}	–
HR 4796	1.8×10^{-02}	8.2×10^{-19}	$<2.2 \times 10^{-18\,b}$
HD 131885	2.1×10^{-03}	7.6×10^{-19}	–
HD 38678	1.2×10^{-05}	5.9×10^{-19}	$<4.2 \times 10^{-18\,b}$
HD 95086	7.3×10^{-04}	5.7×10^{-19}	–
HD 138813	4.0×10^{-03}	5.7×10^{-19}	–
HD 164249	2.0×10^{-04}	5.7×10^{-19}	$<3.6 \times 10^{-18\,c}$
HD 181327	2.2×10^{-04}	5.3×10^{-19}	$<7.6 \times 10^{-18\,c}$
HD 138965	4.8×10^{-04}	4.6×10^{-19}	–
HD 221354	5.7×10^{-05}	4.6×10^{-19}	–
HD 10647	3.4×10^{-05}	4.2×10^{-19}	–
HD 124718	2.4×10^{-04}	3.8×10^{-19}	–
HD 15745	2.3×10^{-04}	3.8×10^{-19}	–
HD 191089	1.5×10^{-04}	3.8×10^{-19}	–
HD 21997	2.5×10^{-04}	3.4×10^{-19}	$<1.4 \times 10^{-18\,b}$
HD 76582	1.3×10^{-04}	3.3×10^{-19}	–
HD 192758	2.4×10^{-04}	3.0×10^{-19}	–
HD 30447	3.3×10^{-04}	3.0×10^{-19}	–
HD 6798	2.8×10^{-04}	2.7×10^{-19}	–
HD 161868	7.4×10^{-05}	2.6×10^{-19}	$<2.8 \times 10^{-18\,b}$
HD 54341	4.3×10^{-04}	2.3×10^{-19}	–
HD 111520	4.8×10^{-04}	2.0×10^{-19}	–
HD 38206	2.1×10^{-04}	2.0×10^{-19}	–
HD 106906	2.5×10^{-04}	2.0×10^{-19}	–

[a]Cataldi et al. (2015).

[b]We obtained *Herschel* PACS C II data from the *Herschel* Science archive, and extracted spectra from Level 2 data products following the procedure described in the PACS Data Reduction Manual using HIPE v15.0.0. For pointed observations, spectra were obtained from the central 9.4 arcsec spaxel (HD38678, HD164249, HR4796, HD161868) of the rebinned data cubes. For mapping observations (HD21997), we extracted a spectrum from the drizzle map by spatially integrating over spaxels over which continuum emission is detected. For all spectra, we first removed edge channels with extreme noise levels, then checked that the continuum level is in agreement with published measurements from the PACS photometer and subtracted it using a second-order polynomial fit in spectral regions sufficiently distant from the C II line wavelength. As any emission present is expected to be spectrally unresolved at the resolution of the instrument (239 km s^{-1}), the 3σ upper limits reported are simply the RMS of the final spectrum multiplied by the spectral resolution of the data.

[c]Riviere-Marichalar et al. (2014).

Indeed, for a primordial gas origin, H$_2$ will shield CO photodissociation and carbon atoms will not be as abundant. As for HD 138813 and HD 156623, the line was not observed with *Herschel*.

HR 4796 (labelled in orange) is the only star from the sample well above the PACS detection threshold in the optically thick region. However, we note that the flux will be lower than predicted because the C II line becomes optically thick. We find that indeed, C II could not be detected with PACS but could be with SPICA. However, HR 4796 is an A0V star and the radiation pressure on C I is high and could force C I to leave the system on dynamical time-scales (Fernández et al. 2006). We discuss radiation pressure effects in more detail in Section 6.1.

Fomalhaut (the non-labelled red dot at 7.7 pc) lies close to the detection threshold. Our flux prediction in Table 6 is still lower than

the published upper limit from PACS (2.2×10^{-18} W m^{-2}, Cataldi et al. 2015). Other systems lie below the PACS detection threshold and, for those observed are indeed not detected.

New far-IR instruments such as SPICA or FIRS are needed to detect more C II gas discs. It is interesting to note that an instrument such as SPICA would increase our number of detections by a factor $\sim$7. For SPICA, targets with small C II masses will be out of LTE. According to our flux predictions, SPICA could detect $\sim$25 new C II gas discs among which are Fomalhaut, HD 156623, HD 181327 and HR 4796. Using the NLTE detection threshold for FIRS, we predict that it could detect C II in at least 100 systems. In Table 6, we provide a list of the most promising targets to look for C II with new missions.

4.3 C I model predictions and results

C I has only been observed around β Pic and 49 Ceti in absorption with the HST/STIS (Roberge et al. 2000, 2014). APEX has only provided upper limits so far (KWC16). We here investigate whether ALMA is likely to detect C I around other debris disc hosts, and which are the favoured systems in which to search for it.

In Fig. 8, we repeat the same procedure as for CO and C II. We also compute the critical density for the C I to be in LTE and find that $M_{\text{C I}} \sim 3 \times 10^{-2} \, M_\oplus$ is required. This is high enough that most detections that can be made with APEX and ALMA will be in NLTE. We computed the population levels in NLTE in equation (9) to work out the $\tau_\nu = 1$ line. For an edge-on configuration, we find that $M_{\text{C I}} \sim 3 \times 10^{-4} \, M_\oplus$. Thus, the C I line is likely to be optically thick for the most distant systems with CO detected. For this reason, the C I detection limits increase faster than distance squared beyond some distance, meaning that these systems should not be detected with APEX even for the most CO-rich debris discs. Only β Pic, 49 Ceti and HD 21997 for the predictions from the observed CO in purple, and HR 4796 are close to the APEX detection threshold (though note that HD 21997 is thought to be made of primordial gas). For other systems, only ALMA will be able to offer detections as can be seen from our flux predictions in Table 7.

One can see that the C I mass predicted for β Pic in KWC16, shown as a green point in Fig. 8, is well below the APEX detection threshold. Indeed, C I in β Pic was not detected with APEX (20 min on source, KWC16). Similarly to C II, we expect the flux impinging on the β Pic gas disc to be higher than assumed here (as was found in KWC16[5]), therefore, the C I mass will go down and our β Pic prediction will in reality be closer to the observation and even farther below the 20 min APEX threshold (not shown here but $\sim$1.7 times higher than the 1 h line). Our flux prediction of 2.3×10^{-19} W m^{-2} (even without increasing the impinging radiation) is close to the APEX upper limit from KWC16 and ALMA should detect C I easily in this system.

From our sample of debris disc stars, we find that with ALMA we could detect at least 30 systems (at 5σ in an hour) that are listed in Table 7. By pushing the integration time to 5 h, we could reach $\sim$45 systems. We also plot the detection limits at 370 µm, which correspond to the higher C I transition. This transition can be more sensitive with APEX for temperatures higher than $\sim$65 K.

---

[5] Here, we emphasize that this is a specific feature of β Pic, probably due to its high stellar activity as explained in KWC16. However, we expect the flux impinging on other debris discs to be closer to the sum of the standard interstellar and stellar radiation fields.
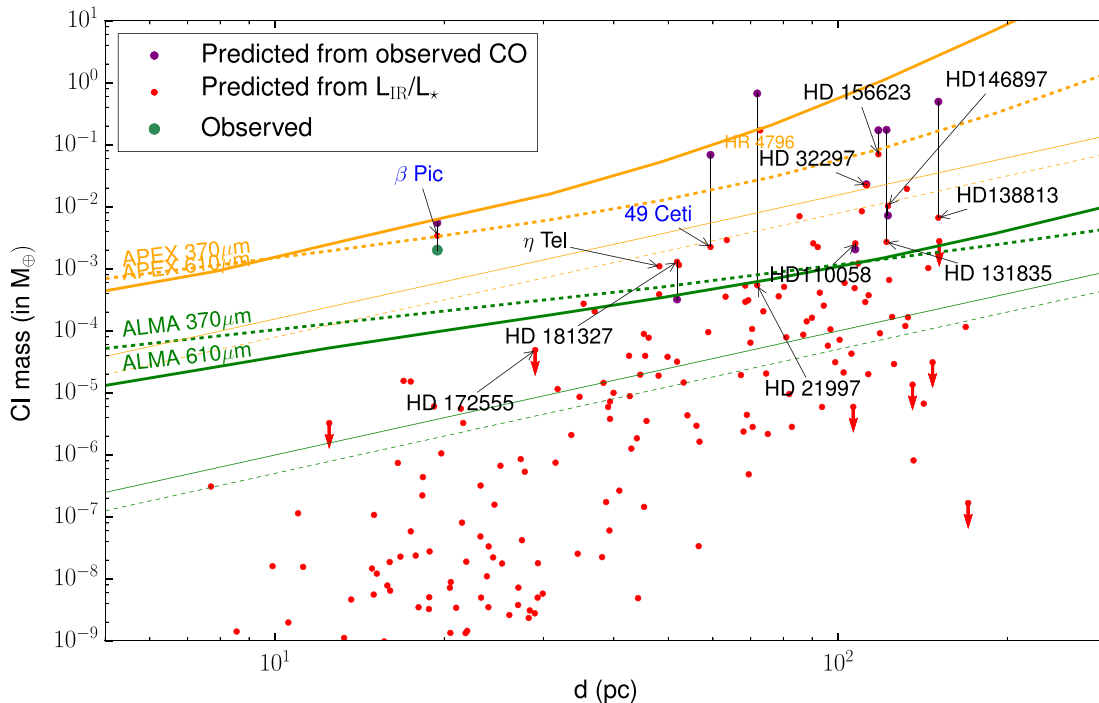
Figure 8. C I mass (in $M_\oplus$) as a function of distance to Earth (*d*). Planetary systems with gas detections are labelled with their names. If C I is detected, the label is in blue (black otherwise). The C I mass for β Pic, derived from Kral et al. (2016) is shown as a green point. The red points are predictions from our model. The red downward arrows show systems that are in the blue hatched area on Fig. 1, which cannot keep CO trapped on solid bodies. The purple points show predictions from our model when the observed CO mass is used rather than the CO mass predicted from L_{IR}/L_*. Detection limits at 5σ in 1 h are shown for APEX (in orange) and ALMA (in green) at 370 (dotted) and 610 microns (solid). The thin lines are for LTE calculations and thick lines for more realistic NLTE calculations (using the same assumptions as described in Section 3.5).

Our flux predictions in Table 7 show that β Pic and 49 Ceti, the two systems with C I detected, are indeed among the three most favourable targets. Systems such as η Tel, HD 156623, HD 172555, HD 32297, HD 181327, HD 110058 that have detected gas should be searched for C I first, as a combination of CO+C I or C II+C I (for η Tel) can provide much more information on the systems (e.g. value of the viscosity α, ionization fraction).

Therefore, we predict that ALMA observations of C I are a promising way to detect secondary gas in debris discs. Also, thanks to ALMA's very high resolution, it will be possible to explore the inner parts of planetary systems and might provide a new complementary picture compared to dust observations. These C I observations could be used to study the gas distribution in the inner regions of planetary systems, which might trace the location of new inner planets (if structures are observed in these atomic gas discs). Also, the discovery of more of these new atomic gas discs will enrich our knowledge of the gas dynamics and more values for α (which parametrizes the viscosity) could be calculated and compared to the MRI theory (e.g. Kral & Latter 2016).

4.4 Atomic mass variation when changing parameters

We here study the impact on our atomic mass predictions when varying parameters. Fig. 9 shows the variations expected when parameters vary from their fiducial values within the allowed range (see Table 8). The upwards and downwards arrows show the direction of a change in atomic mass when a given parameter is increased. Compared to CO, some new parameters come into play. Indeed, the atomic masses depend on α, T_{gas} and f but do not depend on t_{ph} or ϵ_{CO}.

One can see that for atoms, the most important parameters are α, the belt width and γ. By varying these parameters, one can account for a factor $\sim$10 in either direction between our predictions and observations. These variations are the same for C I, C II or O I except for the last two parameters f_{CI} and f_{CII} listed in Fig. 9, which are the variations implied by a change of f on C I and C II masses, respectively.

5 UNDERSTANDING OXYGEN

We proceed in the same way as described in previous sections to produce Fig. 10. We assume that oxygen stays neutral as its ionization potential is 13.6 eV and UV photons with such high energies are depleted around A-type or later-type than A star (Zagorovsky et al. 2010). O I was detected in absorption with HST around 49 Ceti. *Herschel* only detected O I around β Pic and HD 172555. We know that HD 172555 is in the blue hatched area in Fig. 1 and so grain temperatures might be too high to maintain CO on solids. In this particular system, it could be that O I is created from SiO photodissociation or evaporation of O-rich refractories rather than CO (Lisse et al. 2009). However, we decided to show our model prediction for O I if CO could survive on solid bodies in HD 172555. We notice that HD 172555 stands out compared to other systems with gas detected as the O I mass predicted is the lowest.

The LTE limit for O I (63 µm) is at 38 $M_\oplus$. Indeed, the O I critical electron density is very high because the Einstein *A* coefficients (and hence spontaneous decays) are higher than other cases. Therefore, the whole parameter space shown in Fig. 10 is out of LTE. LTE is a very bad approximation for O I and should not be used. The LTE/NLTE detection thresholds are shown in red for PACS, orange

Table 7. List of ALMA promising C I targets and their predicted masses and fluxes.

Star's name	C I mass ($M_\oplus$)	$F_{\text{C I } 610\,\mu\text{m}}$ (W m^{-2})
β Pic	3.4×10^{-03}	2.3×10^{-19}
HR 4796	1.7×10^{-01}	4.9×10^{-20}
49 Ceti	2.2×10^{-03}	4.9×10^{-20}
HD 156623	7.0×10^{-02}	4.3×10^{-20}
η Tel	1.1×10^{-03}	2.1×10^{-20}
HD 138813	6.7×10^{-03}	2.0×10^{-20}
HD 21997	5.4×10^{-04}	1.5×10^{-20}
HD 131835	2.7×10^{-03}	1.4×10^{-20}
HD 191089	1.2×10^{-03}	1.4×10^{-20}
HD 15745	2.9×10^{-03}	1.3×10^{-20}
HD 172555	4.9×10^{-05}	1.2×10^{-20}
HD 32297	2.2×10^{-02}	9.6×10^{-21}
HD 181327	1.3×10^{-03}	9.6×10^{-21}
HD 114082	7.0×10^{-03}	7.9×10^{-21}
HD 95086	2.6×10^{-03}	7.9×10^{-21}
HD 86087	4.1×10^{-04}	7.6×10^{-21}
HD 61005	2.7×10^{-04}	6.8×10^{-21}
HD 106906	2.2×10^{-03}	6.5×10^{-21}
HD 129590	1.9×10^{-02}	6.5×10^{-21}
HD 107146	2.1×10^{-04}	6.4×10^{-21}
HD 117214	8.5×10^{-03}	6.3×10^{-21}
HD 146897	1.0×10^{-02}	5.7×10^{-21}
HD 164249	3.9×10^{-04}	5.6×10^{-21}
HD 110058	2.6×10^{-03}	5.4×10^{-21}
HD 131885	6.6×10^{-04}	4.9×10^{-21}
HD 221853	5.4×10^{-04}	4.4×10^{-21}
HD 121191	2.8×10^{-03}	3.8×10^{-21}
HD 69830	3.3×10^{-06}	3.2×10^{-21}
HD 170773	2.1×10^{-04}	2.7×10^{-21}
HD 124718	3.6×10^{-04}	2.6×10^{-21}
HD 38678	3.3×10^{-06}	2.0×10^{-21}
HD 182681	6.4×10^{-05}	1.8×10^{-21}
HD 35841	5.9×10^{-04}	1.8×10^{-21}
HD 106036	7.2×10^{-05}	1.8×10^{-21}

for SAFARI and green for FIRS (10 m). The thick NLTE lines are ∼3 orders of magnitude less sensitive than LTE. Therefore, one needs a 1000 times higher O I mass (compared to LTE) to detect a system that is out of LTE.

The PACS NLTE detection threshold shows that indeed the detection of O I around β Pic is above the 1-h detection limit. We note however that our prediction for β Pic (in red) lies below the detection threshold. Indeed, in KWC16, we found by fitting the OI PACS spectrum that the O I mass needed some extra oxygen coming from water in addition to the oxygen coming from CO to fully explain the observed flux (1.7×10^{-17} W m^{-2}) with a total oxygen mass of 5×10^{-2} M$_\oplus$ (green point in Fig. 10). Including oxygen coming from water photodissociation in other targets would increase their O I mass and the extra H I may act as an extra collider together with electrons to make the O I line easier to detect. Our flux prediction for β Pic would change from 1.1×10^{-18} to 1.4×10^{-17} W m^{-2} when adding extra water (see Table 9). We discuss this idea further in Section 6. We find that HR 4796 lies well below the PACS detection limit. O I observations for this system were attempted with PACS but led to no detection, as predicted by our model. This system is however the most promising as shown in Table 9 which shows our flux predictions for systems that could be observed with SPICA. Other systems lie below the PACS detection threshold. This is once again consistent with observations that have been made so far.

For HD 172555, we recomputed a new mass from the observed PACS flux equal to 9×10^{-18} W m^{-2} (Riviere-Marichalar et al. 2012), taking into account NLTE effects and optical thickness of the line. We find an O I mass of 3×10^{-3} M$_\oplus$ (green point on Fig. 10). We also compute the observed mass if some extra water (and then hydrogen) comes off the grain while releasing CO (see Section 6) and find an O I mass of 3×10^{-5} M$_\oplus$ (second green point for HD 172555), which is closer to our prediction. From Table 9, we see that we also predict that the O I flux for HD 172555 is ∼3×10^{-19} W m^{-2}, which is below the PACS sensitivity and ∼ 2.5×10^{-17} W m^{-2} with extra water, which is detectable with PACS (see Section 6). The flux prediction for this system is high given its low predicted mass in Fig. 10. Because HD 172555 parent belt is within a few au, the electron density will be much higher than assumed when plotting the detection threshold in Fig. 10, making this oxygen line much closer to the LTE regime and the new detection threshold much closer to the thin lines shown in Fig. 10. While HD 172555 is not predicted to have detectable levels of O I, it is the third highest flux prediction and it could be that (as in β Pic), some water is also released together with CO, which would boost our prediction and explain the PACS detection (see Section 6). O I could also be produced from gas released from refractory elements as suggested in Lisse et al. (2009).

Fig. 10 also shows that the new far-IR instrument SAFARI on SPICA may lead to a few more detections. The orange line is 20 times more sensitive than PACS and would obtain ∼3 new detections if we integrate on source 5 h. More detections would be possible if water is released together with CO. A mission such as FIRS could detect debris disc stars with O I. The NLTE FIRS detection threshold (thick green) is ∼200 times more sensitive than the NLTE SAFARI (thick orange) line and could enable detection of ∼35 new systems.

Detections of O I with SPICA would be a great way to assess the amount of water in these systems and see how much it contributes to the overall O I flux. In Table 9, we provide a list of the most promising targets that should be looked for with any new facility that can target the O I 63 μm line.

6 DISCUSSION

6.1 Radiation pressure on C I, C II and O I

Here, we discuss the effect of having an accretion disc which extends all the way to the star on the radiation pressure force felt by atoms.

In Fig. 11, we show how β, the radiation pressure force relative to gravity, varies with the CO input rate $\dot{M}_{\text{CO}}$ and L_* for different species. The radiation pressure on atoms comes from the star as the IRF is assumed to be isotropic so has a zero net overall effect on radiation pressure. For high enough $\dot{M}_{\text{CO}}$, the accretion disc will become optically thick to UV radiation in the radial direction, decreasing the effectiveness of the star's radiation pressure.

For β Pic, it is predicted that with sufficiently high C II mass in the system, metals will brake due to Coulomb collisions with C II, which is not affected by radiation pressure (Fernández et al. 2006). However, for early stellar types (earlier than A5V), $\beta_{\text{C I}}$, the effective β for C I, can become greater than 0.5. Therefore, without any shielding from the star, C I would be blown out from the system. Carbon could not be kept in its ionized form C II as it constantly transforms into C I on an ionization time-scale but rather all the carbon would be blown out. In Fig. 11, we quantify the luminosity at which this transition happens and also how much mass is required
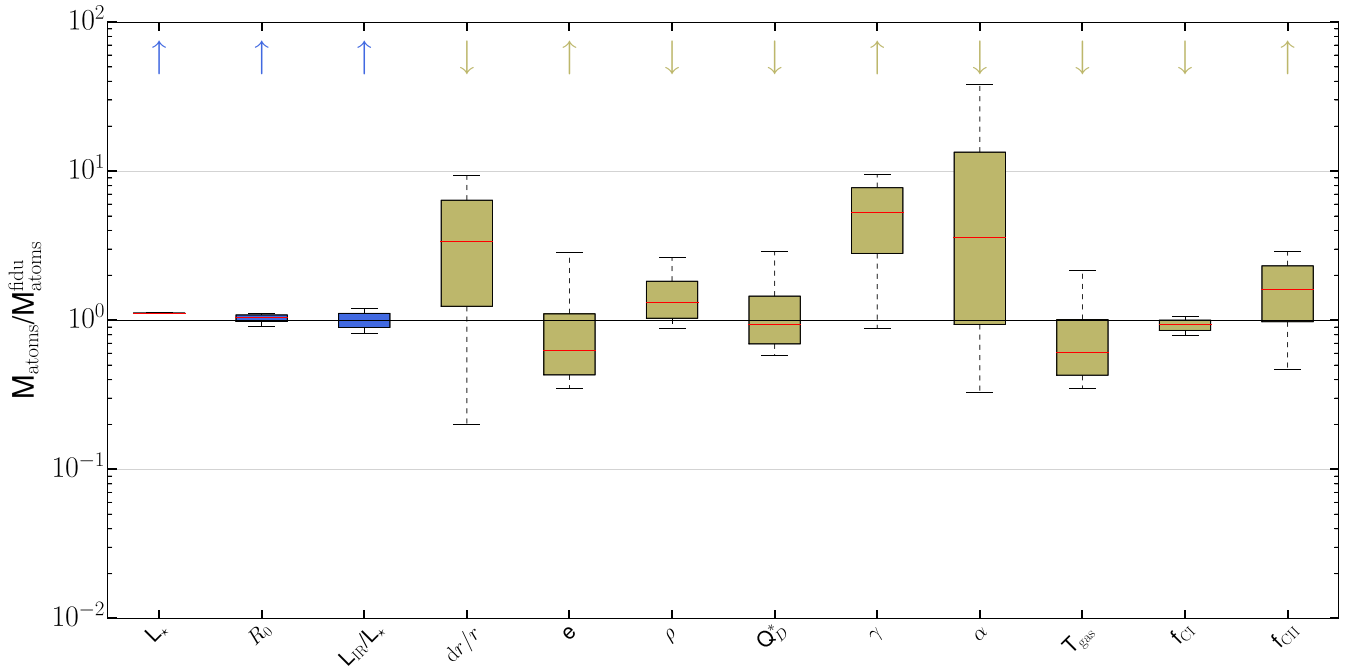
Figure 9. C I, C II or O I mass variations whilst varying parameters one by one. The fiducial values and amplitude of variations of the different parameters are given in Table 8. The blue boxes are for parameters where we have a good observational handle and only error bars on the predicted values are taken into account. For fawn boxes, there are more uncertainties and we allow for a large physical variation for each parameter. Box sizes show where 50 per cent of the distribution is located, while the whiskers contain 95 per cent of the distribution. The red line is the median value. We indicate with an upwards or downwards arrow the sense of variation for M_{atoms} if a given parameter is increased.

Table 8. Parameters of the C I, C II, O I model that can be varied. We indicate the fiducial value picked for each parameter as well as a typical range of variations.

Parameters	Fiducial value	Range of variation
L_* ($L_\odot$)	10	10 per cent
R_0 (au)	85	Factor 2
L_{IR}/L_*	10^{-4}	10 per cent
dr/r	0.5	0.1–1.5
e	0.05	0.01–0.2
ρ (kg m^{-3})	3000	1000–3500
$Q_D^\star$ (J kg^{-1})	500	100–1000
γ (in per cent)	6	2–60
α (log)	0.5	0.01–2
T_{gas} (K)	10	Factor 3
f	0.1	Factor 3

to stop C I from being blown out. To do so, we compute β as (Fernández et al. 2006)

$$\beta = \frac{R^2}{8\pi c^2 \, GM_\star m} \sum_{i<j} \frac{g_j}{g_i} A_{ji} \lambda_{ij}^4 F_\lambda, \tag{18}$$

where M_* is the stellar mass and m is the mass of the considered atom (here, carbon or oxygen) for which β is computed. g_j and g_i are the jth and ith statistical weights, A_{ji} the Einstein A coefficient corresponding to the j to i transition and λ_{ij} the transition wavelength (all the transitions were downloaded from the NIST data base[6]). Note that β does not depend upon R as the stellar flux F_λ and gravity both scale as R^{-2}.

[6] https://www.nist.gov/pml/atomic-spectra-data base

We find that without shielding, C I should start to be blown out in systems with stellar luminosity greater than $\sim 8 \, L_\odot$. However, for a relatively small value of $\dot{M}_{CO}$, $\beta_{C\,I}$ goes below 0.5 even around these highly luminous stars because of self-shielding. We predict that in all systems with $\dot{M}_{CO} > 10^{-4} \, M_\oplus \, Myr^{-1}$, C I can be protected from being blown out. We also predict that without shielding C II would be blown out for systems with $L_* > 15 \, L_\odot$ but O I would stay bound up to 25 $L_\odot$.

According to our predictions, a system with a CO mass input rate ~ 1000 times smaller than in β Pic is enough to keep C I or C II from being blown out. Thus, it is likely that this effect will only affect systems with very low CO mass input rates. We can check on Fig. 4 that a system with one thousandth of the β Pic mass would not be detectable with ALMA.

6.2 Caveats

Analytical version of the code: The semi-analytical model presented here has a few caveats. First of all, we assume equation (1) to compute the mass lost through the cascade. This equation is only valid at steady state for a typical -3.5 size distribution. Some more refined numerical models could be used to derive the lost mass using more realistic particle size distributions (e.g. Wyatt, Clarke & Booth 2011) or departing from the steady-state assumption (e.g. Thébault & Augereau 2007; Löhne, Krivov & Rodmann 2008; Kral et al. 2015). In this equation, some parameters are not directly accessible to observers such as the planetesimal eccentricity, their bulk density or their collisional strength Q_D^*. Also, in equation (2), we assume that a fraction γ of the dust mass is converted into CO. For instance, varying γ can give us a way to fit the prediction with the observation and thus constrain the amount of CO on planetesimals. However, through Figs 6 and 9, we were able to quantify the impact

Figure 10. O I mass (in $M_\oplus$) as a function of distance to Earth (d). Planetary systems with gas detections are labelled with their names. If O I is detected, the label is in blue (black otherwise). The O I mass for β Pic, derived from PACS observations (Brandeker et al. 2016; Kral et al. 2016) is shown as a green point as well as the observed mass for HD 172555 considering the flux observed with PACS (Riviere-Marichalar et al. 2012). The second green point (at a lower mass) for HD 172555 considers that some extra hydrogen comes off the grains at the same time as CO is released (see Section 6). The red points are predictions from our model. The red downward arrows show systems that are in the blue hatched area on Fig. 1, which cannot keep CO trapped on solid bodies. The purple points show predictions from our model when the observed CO mass is used rather than the CO mass predicted from L_{IR}/L_*. Detection limits at 5σ in 1 h are shown for *Herschel*/PACS (in red), SPICA/SAFARI (in orange) and FIRS (in green) for a 10 m aperture. The thin lines are for LTE calculations and thick lines for more realistic NLTE calculations (using the same assumptions as described in Section 3.5).

Table 9. List of SPICA promising targets to look for O I and their predicted masses and fluxes without (2 first columns) and with extra water released together with CO (2 following columns). The last column gives observed fluxes or upper limits when systems were observed with *Herschel*.

Star's name	O I mass ($M_\oplus$)	$F_{\text{O I 63 }\mu m}$ (W m^{-2})	O I mass (with H$_2$O) ($M_\oplus$)	$F_{\text{O I 63 }\mu m}$ (with H$_2$O) (W m^{-2})	$F_{\text{O I(obs) 63 }\mu m}$ (W m^{-2})
β Pic	5.1×10^{-03}	1.1×10^{-18}	1.5×10^{-02}	1.4×10^{-17}	1.7×10^{-17} (1)
HR 4796	2.5×10^{-01}	3.7×10^{-19}	7.5×10^{-01}	4.4×10^{-18}	$<4.7 \times 10^{-18}$ (2)
HD 172555	6.6×10^{-05}	3.1×10^{-19}	2.0×10^{-04}	2.5×10^{-17}	$9.2 \pm 2.4 \times 10^{-18}$ (3)
HD 121191	3.9×10^{-03}	9.9×10^{-20}	1.2×10^{-02}	1.7×10^{-18}	–
η Tel	2.2×10^{-03}	8.9×10^{-20}	6.6×10^{-03}	1.6×10^{-18}	6.2×10^{-18} (4)
Fomalhaut A	4.1×10^{-05}	5.9×10^{-20}	1.2×10^{-04}	2.4×10^{-19}	1.0×10^{-17} (5)
HD 138923	1.6×10^{-05}	4.3×10^{-20}	4.7×10^{-05}	2.7×10^{-18}	–
HD 156623	9.9×10^{-02}	4.2×10^{-20}	3.0×10^{-01}	3.0×10^{-18}	–
49 Ceti	4.4×10^{-03}	3.5×10^{-20}	1.3×10^{-02}	3.2×10^{-18}	$<1.1 \times 10^{-17}$ (6)
HD 106036	1.8×10^{-04}	1.3×10^{-20}	5.5×10^{-04}	1.1×10^{-18}	–
HD 138813	1.4×10^{-02}	1.2×10^{-20}	4.3×10^{-02}	1.2×10^{-18}	$<1.3 \times 10^{-17}$ (7)
HD 181327	2.0×10^{-03}	1.1×10^{-20}	6.0×10^{-03}	5.5×10^{-19}	$<8.2 \times 10^{-18}$ (4)

(1) KWC16, (2) Riviere-Marichalar et al. (2013), (3) Riviere-Marichalar et al. (2012), (4) Riviere-Marichalar et al. (2014), (5) Cataldi et al. (2015), (6) Roberge et al. (2013), (7) Mathews et al. (2013).

of each parameter variation. We concluded that for a given system, the predicted mass can vary by a factor 10. This can explain some of the differences between observations and predictions and ultimately could lead to constraints on some of these free parameters.

Cooling/heating: Another assumption is that the only coolant is the C II fine structure line and that the only heating mechanism is C I photoionization. For the low temperatures expected in debris discs and given the amount of dust in these systems, this is likely to be a good approximation. Indeed, as shown in

KWC16, one needs very dusty discs for photoelectric heating to dominate over C I photoionization. To be more specific, one needs dustier systems than β Pic with an optical depth $\gtrsim 10^{-2}$, which is never the case for debris discs (by definition). Thus, this assumption is likely to always be valid. Cooling by the O I fine structure line at 63.2 μm may also be important. However, when carbon is present, and for the range of temperatures expected in these gas discs, the C II line is always the dominant coolant as shown in Zagorovsky et al. (2010) and using CLOUDY simulations in
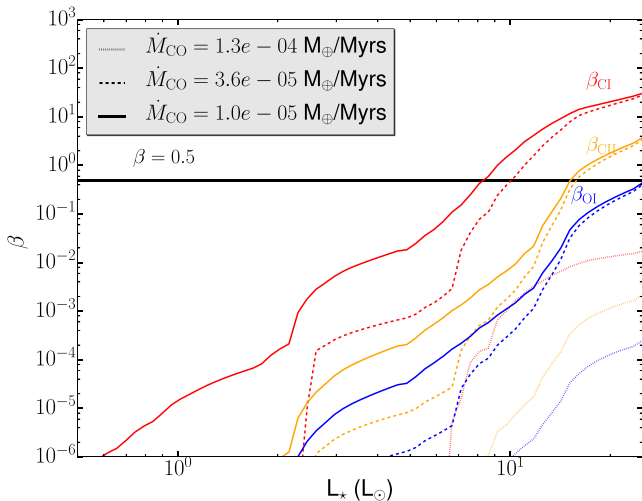
Figure 11. β as a function of L_* computed for three different atomic species C I (in red), C II (in yellow) and O I (in blue) for different CO input rates 10^{-5} $M_\oplus$ Myr^{-1} (solid line), 3.6×10^{-5} (dashed) and 1.3×10^{-4} (dotted). The black line shows the location of $\beta = 0.5$, above which atoms are unbound.

KWC16. It is mainly due to the O I line being in strong NLTE in debris discs.

Extra water released together with CO: In this paper, we assumed that there was no extra water released at the same time as CO. However, if CO ($+CO_2$ that contributes to providing more CO when photodissociating) is trapped in water ice, a certain amount of H_2O may also be released in the process (see KWC16). Water photodissociates a lot faster than CO and this will add more oxygen in the system, but also excite the O I line more due to extra collisions with neutral hydrogen. The amount of water released at the same time as CO is not known yet and thus the amount of extra colliders or extra oxygen can only be assumed.

We compute new predictions for O I assuming that the $(CO+CO_2)/H_2O$ abundance ratio is $\sim$30 per cent (i.e. an average Solar system composition, 2–60 per cent, Mumma & Charnley 2011). Therefore, the new oxygen mass released is $\sim$3 times higher than without extra water. The new O I predictions are plotted in Fig. 12 and the most favourable targets are listed in Table 9. We see that the new prediction for β Pic is closer to the observation. Also, SPICA would be able to detect O I in more systems due to both higher O I masses and higher excitation of the O I energy levels. Indeed, in this case, we computed the NLTE lines taking into account the extra H I colliders that will further excite the O I energy levels. We assume that the ionization fraction is 0.1 so the corresponding $n_H/n_e \sim 60$ is input in the NLTE code. In this case, the detection thresholds go down and it becomes easier to detect O I as it is more excited. If the amount of water released is close to that assumed, SPICA could detect $\sim$30 systems with O I (see Table 9 or Table C2 to get the full list) instead of 3 for the case without extra water.

When adding extra water in HD 172555, our flux prediction comes closer to the observed flux (see Section 5 for the calculations without extra water). This can already be seen in Fig. 12, where we computed the mass from the observed flux by PACS (Riviere-Marichalar et al. 2012) taking into account some extra hydrogen in the same proportion as given in the previous paragraph. This new mass is much smaller than when there is no water (3×10^{-5} $M_\oplus$) but will produce the observed flux as it is more excited (by H I). Our prediction for HD 172555 when extra water is released provides a total O I mass of 2.0×10^{-4} $M_\oplus$ and a flux of 2.5×10^{-17} W m^{-2}

that is close to the observed flux. We find that assuming a standard CO/H_2O abundance ratio consistent with the composition of Solar system's comets is able to explain the observed flux and we then predict that the O I mass in HD 172555 is $\sim 10^{-4}$ $M_\oplus$. A better knowledge of the position of the gas in this system could help to know whether water can still remain on these warm grains.

Interestingly, new missions such as SPICA could assess the amount of water released together with CO (as was done in KWC16 using the O I line). We notice that the more colliders, the more the NLTE lines get closer to the LTE regime, which is favourable for detections. However, in Fig. 12 the NLTE line is still 3 orders of magnitude above LTE even when assuming a Solar system comet composition to derive the amount of extra water released. Releasing water together with CO will not affect our predictions for C I, C II and CO masses but it may slightly change the NLTE lines that are plotted on the corresponding figures. It would make systems that are in NLTE easier to detect. We concluded in KWC16 that the hydrogen was not playing any role in the thermal budget of the gas disc and we assume the same here, i.e. that the temperature will not vary when adding more water in the system.

Mass predictions: The predictions presented in this paper are not guaranteed to exactly fit all new coming observations as there are some uncertain free parameters. However, our default set of parameters still allows our model to work for a wide range of systems. For instance, we fixed the planetesimal eccentricity to be 0.05 but from one system to another, this could easily vary from 0.01 to 0.2. The masses predicted vary as $e^{5/3}$ and could explain part of the differences with observations. For an individual system, one can refine the estimates for the free parameters. For instance, for a resolved belt, its width dr is known better than within a factor 15 (that was assumed here in our error calculations). Therefore, our results should be used with caution (large error bars should be given) when dealing with the fiducial values rather than the specific parameters derived from a given system. However, all general results given here can be used as a guide to further our understanding of gas and increase the amount of actual detections.

Flux predictions: The flux predictions given in this paper should also be taken with caution. Our model computes a prediction for the mass that has to be converted to a flux. For CO, where the CMB dominates the excitation, the conversion is straightforward when the line is optically thin. However, when lines become optically thick, the predicted flux will depend on optical thickness τ_ν. To compute τ_ν, we here assume that CO is in a ring centred at R_0 with a width $dr/r = 0.5$ and that the surface density is constant. This could be refined for some systems in the future when ALMA provides resolved CO maps. Also, we assume an edge-on configuration when computing τ_ν, which is the most constraining case and so some of our flux predictions could be slightly underestimated.

The conversion from mass to fluxes for C I, C II and O I is more complicated and thus more uncertain. On top of the optical thickness assumptions cited above, the dust radiation field matters. The CMB at these shorter wavelengths is not dominant and it is mainly the dust radiation field that drives the excitation of the lines. The dust radiation field that we know best at these wavelengths is for β Pic. Thus, we assume that dust radiation field and scale it up or down for the different systems by comparing the flux found by fitting an SED to the β Pic flux. We thus do not expect that our flux predictions match exactly future observations but they rather give an order of magnitude estimate to check which systems are most likely to be detectable. One should not rule out a target with a slightly lower predicted flux as this could go up if we underestimated the dust radiation field impinging on the gas disc.
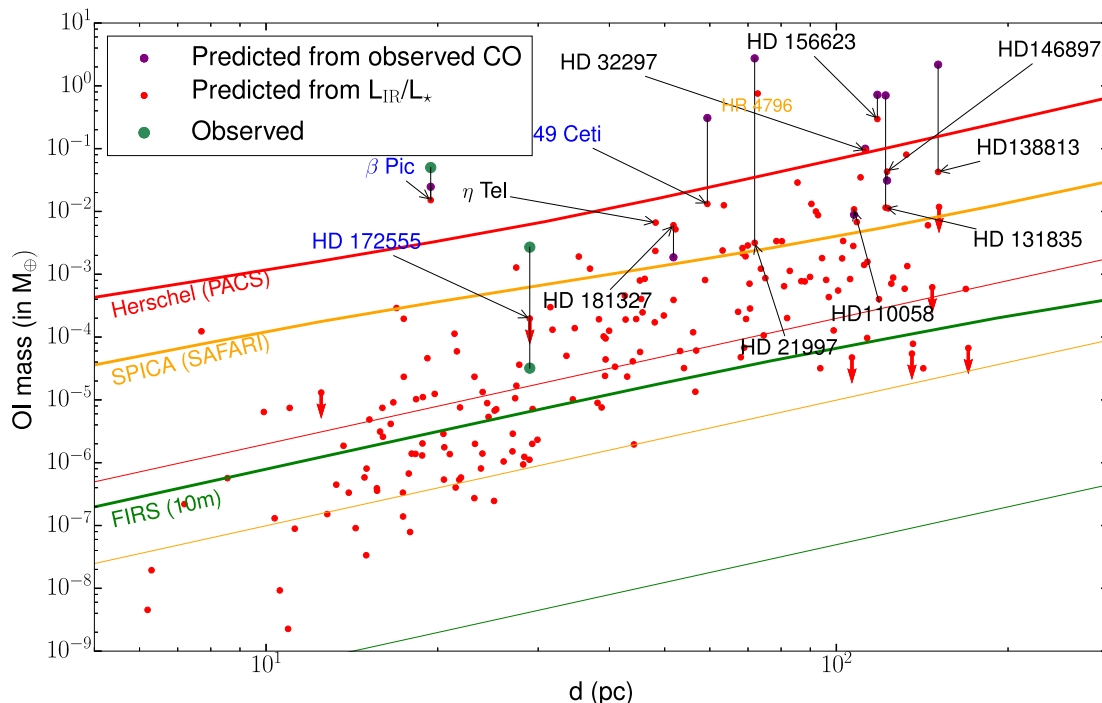
Figure 12. O I mass (in $M_\oplus$) as a function of distance to Earth (d) when water + CO are released from solid bodies. Planetary systems with gas detections are labelled with their names. If O I is detected, the label is in blue (black otherwise). The O I mass for β Pic, derived from PACS observations (Brandeker et al. 2016; Kral et al. 2016) is shown as a green point as well as the observed mass for HD 172555 considering the flux observed with PACS (Riviere-Marichalar et al. 2012). The second green point (at a lower mass) for HD 172555 considers that some extra hydrogen comes off the grains at the same time as CO is released (see Section 6). The red points are predictions from our model. The red downward arrows show systems that are in the blue hatched area on Fig. 1, which cannot keep CO trapped on solid bodies. The purple points show predictions from our model when the observed CO mass is used rather than the CO mass predicted from $L_{\rm IR}/L_*$. Detection limits at 5σ in 1 h are shown for *Herschel*/PACS (in red), SPICA/SAFARI (in orange) and FIRS (in green) for a 10 m aperture. The thin lines are for LTE calculations and thick lines for more realistic NLTE calculations (using the same assumptions as described in Section 3.5).

Value of the viscosity parameter α: The atomic mass predicted will vary depending on α. Throughout this paper, we assumed that $\alpha = 0.5$ as predicted for the gas disc around β Pic. α could be smaller around less ionized systems and our mass predictions for C I or C II could go up by a factor $0.5/\alpha$. From our results, α is constrained to be relatively large for systems with high atomic masses as otherwise these could have been detected with PACS (for C II) or APEX (for C I). However, for systems lying at the bottom of our plots, one cannot rule out that α is smaller. The mean free path of a gas atom goes up and one might reach another regime to transport angular momentum. Thus our atomic mass predictions could go up and increase the numbers predicted for discoveries by ALMA, SPICA and FIRS.

If the sample with CO+CI gas detected grows significantly thanks to ALMA, and some free parameters can be refined (e.g. dr, ionization fraction, $T_{\rm gas}$, . . .) with these same observations, our model will lead to an estimate for α. It could also show how α varies with ionization fraction. These new α estimates could then be compared to the most promising models at transporting angular momentum in discs, such as the MRI (e.g. Kral & Latter 2016).

Detectability: We emphasize that our predictions for detectability are to be taken as a guide rather than a fixed threshold. Indeed, the NLTE lines depend on the electron density, which vary with radial location. We picked $R_0 = 85$ au in our study to plot the different lines but this should be updated when targeting a specific system, or one should rather look at the flux predictions bearing in mind the caveats described above concerning these fluxes. Also, the optical thickness that is predicted depends on the system's geometry. Thus,

these predictions should be made for each system individually when computing, for instance, the required total integration time to detect a specific transition of a specific species. Finally, the fluxes we provide in Table C2 are also to be taken with caution. The outcome of our model are masses and we have to convert to a flux making some assumptions, as explained in the flux prediction caveat paragraph above.

6.3 Link to future observations

The spatial distribution of the gas compared to the dust is very important to distinguish between different gas release mechanisms (since gas and dust will be co-located or at different positions for different scenarios), making ALMA the perfect tool to understand the origin of the gas.

One of the main outcomes of this study is that we find that ALMA could detect C I gas around at least 30 systems (and ~15 with CO). Using ALMA's high resolution to resolve gas in inner regions of planetary systems could reveal some hidden components of planetary systems. It would enable us to probe the inner parts of planetary systems (for the brightest systems that can be spatially resolved) in a way that cannot be done using dust observations because the dust is located farther from the central star. This could, for instance, enable to resolve structures in gas discs that are created by giant planets located in the inner regions.

We predict that O I observations with SPICA will give only a handful of detections if no water is released in the process of releasing CO, or ~30 detections otherwise. However, having CO, C I

or C II and O I detections can lead to predictions of the amount of water in exocomets and the amount of hydrogen in the gas phase as we have already shown for β Pic in KWC16. Our prediction from KWC16 that hydrogen (together with carbon and oxygen) should be accreted on β Pic has just been confirmed observationally by Wilson et al. (2017). Our model could be used to make predictions on the detectability of H I around other systems than β Pic. Probing the composition of exocomets and the amount of hydrogen observationally using the O I line provides motivation for a sensitive far-IR mission (such as FIRS). This would lead to the first extensive taxonomy of exocomets.

We find that only a small CO input rate ($>10^{-4}$ M$_\oplus$ Myr^{-1}) is sufficient to prevent C I from being pushed away by radiation pressure. However, we note that the implications of this depend on the formation history of the gas in the system. Indeed, if there were no shielding from the very beginning, the C I or C II gas disc that would be building up over a viscous time-scale would be blown out before reaching a sufficient amount of self-shielding. One can imagine that these secondary discs are born at the end of the protoplanetary disc phase and that there were already some shielding from the star at that stage to prevent carbon from being blown out (Wyatt et al. 2015). It is not clear yet which is the right scenario and it might be that both scenarios can be found around different systems and explain why some early-type stars would have carbon observed and some others not. HR 4796 could be a case where a gas disc was never optically thick enough to prevent carbon gas from being blown out. However, the narrowness of the disc could be explained if gas was present (Takeuchi & Artymowicz 2001). New observations with APEX or ALMA of the C I line could distinguish between these two scenarios.

We here suggest a new method to distinguish between a primordial versus secondary origin. Indeed, if our model cannot reproduce observations even assuming extreme values for our free parameters, we claim that the specific systems are likely to have a primordial origin. In this paper, we show that this is the case for HD 21997, HD 131835 and HD 138813. It is complementary to other methods such as observing optically thin line ratios to check whether there is enough molecular hydrogen around to be in LTE (Matrà et al. 2017).

7 CONCLUSION

We tested our new gas model developed for β Pic in KWC16 on all systems with gas detected to check whether our model could explain all observations so far and then give predictions concerning future observations. The model assumes that CO gas observed around debris disc stars is secondary and is created from the solid volatile-rich bodies residing in the parent belt of the discs. Once CO gas is created, it photodissociates into carbon and oxygen atoms, which viscously spread to form an atomic accretion disc inside the parent belt and a decretion disc outside. The model calculates the ionization fraction of carbon, the gas temperature and population levels at different radial locations in the disc. It also takes into account CO self-shielding against photodissociation and CI self-shielding against photoionization. When computing the detectability, we take into account NLTE effects and optical thickness of lines.

We find that our model is able to explain most current observations. Systems that we predict to be detectable are indeed detected and systems that lie under the detection threshold are not. Only for three systems our model cannot reproduce observations. We suggest that these three systems, HD 21997, HD 131835 and HD 138813 are not made only of secondary gas but

still possess some primordial gas. In this sense, our model can rule out a secondary origin for some discs, suggesting rather a primordial origin.

We provide an analytical formulation of our model through a set of equations in this paper. We clearly identify the most important parameters that lead to enhance CO, C I, C II or O I abundances. We define some regions of the parameter space in terms of star's luminosity versus planetesimal belt location where CO is not expected to be observed. For instance, if grains are too warm ($\gtrsim$140 K), we do not expect CO to be retained on grains (e.g. HD 172555) or if the star is too luminous, the CO photodissociation time-scale gets too short to detect CO (e.g. η Tel). We find that we should observe systems with the highest fractional luminosities, closest to Earth and having L_* small enough and the parent belt radial location far enough not to lie in the hatched exclusion areas defined in Fig 1. Also, we study the effect of a change in the assumed fiducial parameter values and give the maximum variations expected for each parameter.

Someone wanting to make predictions for the amount of CO in a specific system can use equation (7) (that uses equations 1 and 2). The CO photodissociation time-scale can be assumed to be 120 yr for systems with debris far from their host star, with the latter not being too luminous (see Fig. 1). The self-shielding factor ϵ_{CO} can be computed using Fig. 3. To derive the total carbon mass or O I mass (assuming no extra water), one should use equation (11). If extra water is assumed to be released together with CO, the O I mass will increase and depends on the assumed H/C ratio. equations (16) and (17) can be used to predict the C II and C I masses in a specific system, where the carbon ionization fraction f can be computed using equation (15) (or assumed to have a typical value of 0.1 for a first guess).

Based on these results, we can use our model to make predictions for systems that have no gas detected so far. To this aim, we have taken a sample of 189 debris disc stars and ran our model for each of them. We make predictions for new detections with ALMA, and with potential future missions such as SPICA and a far-IR 10 m telescope (e.g. FIRS). We predict that ALMA could detect at least 15 systems with CO and 30 with C I (with less than an hour of integration time for each target). C I seems the most promising avenue for the near future and one could use ALMA's high resolution to probe the inner regions of planetary systems through C I that extends all the way to the star (accretion disc), which may indirectly reveal some hidden planets. SPICA will enable us to detect at least 25 new systems with C II and ~30 with O I (depending on the amount of water released together with CO). To detect O I around a fair number of stars, a new far-IR 10 m telescope (such as FIRS) is needed. We give a list of the systems that are most likely to be detected with ALMA in CO and C I in Tables 4 and 7 and with SPICA in C II and O I in Tables 6 and 9.

We also recomputed the O I mass in HD 172555 with our NLTE model from the observed flux with PACS and find 3×10^{-5} M$_\oplus$, which can be explained with our second generation gas model.

We find that CO, C I, C II and O I gas should be modelled in non-LTE for almost all systems, and for the most gas-rich debris discs, CO, C I and O I lines will be optically thick.

In this paper, we also study the effect of radiation pressure on carbon and oxygen. Around luminous stars, C I is expected to be blown out. We find that a small CO input rate (~1000 times smaller than in β Pic) is enough to create a shielding from the star that significantly reduces radiation pressure and allows for C I to stay bound. Therefore, our model explains self-consistently for the first time why carbon was detected around early-type stars.

REFERENCES

Badnell N. R., 2006, ApJS, 167, 334
Beust H., Vidal-Madjar A., Ferlet R., Lagrange-Henri A. M., 1990, A&A, 236, 202
Brandeker A. et al., 2016, A&A, 591, A27
Castelli F., Kurucz R. L., 2004, preprint (arXiv:astro-ph/0405087)
Cataldi G. et al., 2014, A&A, 563, A66
Cataldi G., Brandeker A., Olofsson G., Chen C. H., Dent W. R. F., Kamp I., Roberge A., Vandenbussche B., 2015, A&A, 574, L1
Collings M. P., Dever J. W., Fraser H. J., McCoustra M. R. S., Williams D. A., 2003, ApJ, 583, 1058
Crawford I. A., Spyromilio J., Barlow M. J., Diego F., Lagrange A. M., 1994, MNRAS, 266, L65
Czechowski A., Mann I., 2007, ApJ, 660, 1541
Dent W. R. F., Greaves J. S., Mannings V., Coulson I. M., Walther D. M., 1995, MNRAS, 277, L25
Dent W. R. F., Greaves J. S., Coulson I. M., 2005, MNRAS, 359, 663
Dent W. R. F. et al., 2013, PASP, 125, 477
Dent W. R. F. et al., 2014, Science, 343, 1490
Dickinson A. S., Richards D., 1975, J. Phys. B At. Mol. Phys., 8, 2846
Draine B. T., 2011, in Draine B. T. ed., Physics of the Interstellar and Intergalactic Medium. Princeton Univ. Press, Princeton, NJ (ISBN: 978-0-691-12214-4)
Ferland G. J. et al., 2013, Rev. Mex. Astron. Astrofis., 49, 137
Fernández R., Brandeker A., Wu Y., 2006, ApJ, 643, 509
Freudling W., Lagrange A.-M., Vidal-Madjar A., Ferlet R., Forveille T., 1995, A&A, 301, 231
Gorti U., Hollenbach D., 2004, ApJ, 613, 424
Greaves J. S. et al., 2016, MNRAS, 461, 3910
Grigorieva A., Thébault P., Artymowicz P., Brandeker A., 2007, A&A, 475, 755
Hales A. S. et al., 2014, AJ, 148, 47
Heiter U., Jofré P., Gustafsson B., Korn A. J., Soubiran C., Thévenin F., 2015, A&A, 582, A49
Hughes A. M., Wilner D. J., Kamp I., Hogerheijde M. R., 2008, ApJ, 681, 626
Jackson A. P., Wyatt M. C., Bonsor A., Veras D., 2014, MNRAS, 440, 3757
Kalas P., 2005, ApJ, 635, L169
Kamp I., Bertoldi F., 2000, A&A, 353, 276
Kennedy G. M., Wyatt M. C., 2014, MNRAS, 444, 3164
Kóspál Á et al., 2013, ApJ, 776, 77
Kral Q., Latter H., 2016, MNRAS, 461, 1614
Kral Q., Thébault P., Charnoz S., 2013, A&A, 558, A121
Kral Q., Thébault P., Augereau J.-C., Boccaletti A., Charnoz S., 2015, A&A, 573, A39
Kral Q., Wyatt M., Carswell R. F., Pringle J. E., Matrà L., Juhász A., 2016, MNRAS, 461, 845 [KWC16]
Lecavelier des Etangs A. et al., 2001, Nature, 412, 706
Lieman-Sifry J., Hughes A. M., Carpenter J. M., Gorti U., Hales A., Flaherty K. M., 2016, ApJ, 828, 25
Liseau R., Artymowicz P., 1998, A&A, 334, 935
Lisse C. M., Chen C. H., Wyatt M. C., Morlok A., Song I., Bryden G., Sheehan P., 2009, ApJ, 701, 2019
Löhne T., Krivov A. V., Rodmann J., 2008, ApJ, 673, 1123
Marino S. et al., 2016, MNRAS, 460, 2933

Marino S. et al., 2017, MNRAS, 465, 2595
Mathews G. S., Pinte C., Duchêne G., Williams J. P., Ménard F., 2013, A&A, 558, A66
Matrà L., Panić O., Wyatt M. C., Dent W. R. F., 2015, MNRAS, 447, 3936
Matrà L. et al., 2017, MNRAS, 464, 1415
Montgomery S. L., Welsh B. Y., 2012, PASP, 124, 1042
Moór A., 2016, Zenodo. Available at: http://doi.org/10.5281/zenodo.58429
Moór A. et al., 2011, ApJ, 740, L7
Moór A. et al., 2015, ApJ, 814, 42
Mumma M. J., Charnley S. B., 2011, ARA&A, 49, 471
Nilsson R., Brandeker A., Olofsson G., Fathi K., Thébault Ph., Liseau R., 2012, A&A, 544, A134
Olofsson G., Liseau R., Brandeker A., 2001, ApJ, 563, L77
Pawellek N., Krivov A. V., 2015, MNRAS, 454, 3207
Redfield S., 2007, ApJ, 656, L97
Riviere-Marichalar P. et al., 2012, A&A, 546, L8
Riviere-Marichalar P. et al., 2013, A&A, 555, A67
Riviere-Marichalar P. et al., 2014, A&A, 565, A68
Roberge A., Feldman P. D., Lagrange A. M., Vidal-Madjar A., Ferlet R., Jolly A., Lemaire J. L., Rostas F., 2000, ApJ, 538, 904
Roberge A., Feldman P. D., Weinberger A. J., Deleuil M., Bouret J.-C., 2006, Nature, 441, 724
Roberge A. et al., 2013, ApJ, 771, 69
Roberge A., Welsh B. Y., Kamp I., Weinberger A. J., Grady C. A., 2014, ApJ, 796, L11
Schöier F. L., van der Tak F. F. S., van Dishoeck E. F., Black J. H., 2005, A&A, 432, 369
Swinyard B., Nakagawa T., Merken P. et al., 2009, Exp. Astron., 23, 193
Takeuchi T., Artymowicz P., 2001, ApJ, 557, 990
Thébault P., Augereau J.-C., 2007, A&A, 472, 169
van Hemert M. C., van Dishoeck E. F., 2008, Chem. Phys., 343, 292
Visser R., van Dishoeck E. F., Black J. H., 2009, A&A, 503, 323
Wilson P. A. et al., 2017, A&A, 599, A75
Wyatt M. C., 2008, ARA&A, 46, 339
Wyatt M. C., Clarke C. J., Booth M., 2011, Celest. Mech. Dyn. Astron., 111, 1
Wyatt M. C., Panić O., Kennedy G. M., Matrà L., 2015, Ap&SS, 357, 103
Zagorovsky K., Brandeker A., Wu Y., 2010, ApJ, 720, 923
Zuckerman B., Song I., 2012, ApJ, 758, 77

APPENDIX A: CALCULATIONS OF THE TEMPERATURE IN OUR MODEL

The main heating mechanism in our model is assumed to be photoionization of carbon (see KWC16). Each ionized neutral will give away an electron that will contribute to heating the gas. The amount of energy given to the gas is the difference between the initial photon energy and the ionization potential needed to get ionized. Therefore, the total rate of energy created per unit volume due to photoionization is

$$\Gamma_{\mathrm{ion}} = n_{\mathrm{C\,I}} \int_{\nu_{\mathrm{IP}}}^{\infty} \frac{4\pi J_\nu}{h\nu} h(\nu - \nu_{\mathrm{IP}}) \sigma_{\mathrm{ion}}(\nu)\, \mathrm{d}\nu, \qquad (A1)$$

where $\nu_{\mathrm{IP}} = c/\lambda_{\mathrm{IP}}$ is the minimum frequency to get ionized. $\lambda_{\mathrm{IP}} = 1100$ Å, which corresponds to an ionization potential of 11.26 eV. For carbon, the ionization cross-section does not vary with wavelength and is equal to $\sigma_{\mathrm{ion}}(\nu) = 1.6 \times 10^{-17}$ cm^2 between 912 (Lyman break) and 1100 Å (van Hemert & van Dishoeck 2008).

The main coolant in our model is assumed to be the C II fine structure line at 157.7 μm (see KWC16). Cooling by the O I fine structure line at 63.2 μm can also be important. However, when carbon is present, and for the range of temperatures expected in gas discs, the C II line is always the dominant coolant (Zagorovsky et al. 2010). Statistical equilibrium requires that the upward transitions (collisional excitations) balance the downwards ones
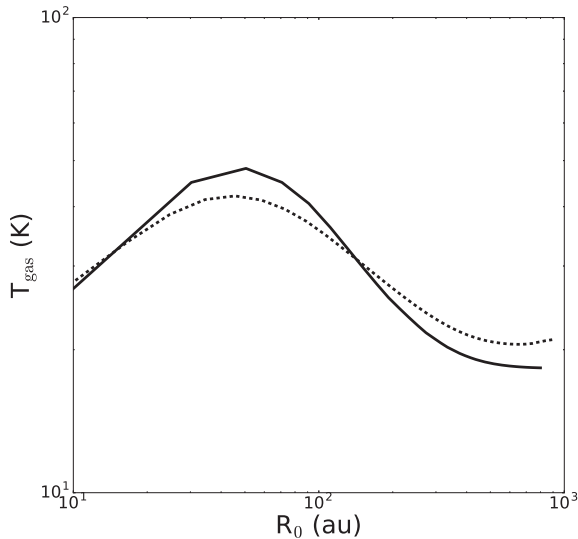
Figure A1. Gas temperature radial profile predicted with our analytical model (solid line) and from the numerical model CLOUDY (dashed line).

(collisional de-excitations and spontaneous radiative decays). For a two-level atom model that represents well the C II line, it gives (following Zagorovsky et al. 2010)

$$n_e n_1 q_{1,2} = n_e n_2 q_{2,1} + n_2 A_{2,1}, \tag{A2}$$

where n_e, n_1 and n_2 are the number densities of electrons and atoms in the lower and upper levels, respectively. $q_{1,2}$ and $q_{2,1}$ are the collisional excitation and de-excitation rates and $A_{2,1}$ is the Einstein coefficient. The gas cooling rate is then defined as (Zagorovsky et al. 2010)

$$\Lambda_{1,2} = (n_2 q_{2,1} - n_1 q_{1,2}) n_e h \nu_{1,2}, \tag{A3}$$

which can be expressed in terms of C II number density $n_{C_{II}} = n_1 + n_2$ using equation (A2)

$$\Lambda_{1,2} = \xi \left(1 - \frac{A_{2,1} + n_e q_{2,1}}{A_{2,1} + n_e (q_{2,1} + q_{1,2})} \right. $$
$$\left. \times \left(1 + \frac{g_2}{g_1} e^{-h\nu_{1,2}/k_B T_{gas}} \right) \right), \tag{A4}$$

where g_1 and g_2 are the statistical weight of the lower and upper level, $\xi = q_{2,1} n_e n_{C_{II}} h \nu_{1,2}$ and $q_{1,2} = q_{2,1} e^{-h\nu_{1,2}/k_B T_{gas}}$.

We can then solve for T_{gas} equating Γ_{ion} to $\Lambda_{1,2}$ to get the temperature as a function of the radial position in the gas disc. We applied this method and compare with the numerically calculated temperature profile (using CLOUDY) for β Pictoris.

In KWC16, the best-fitting model was for an IRF that was ~60 times the standard value. To have a meaningful comparison, we do not use the best-fitting model but rather one of the other models with a standard IRF presented in KWC16. In Fig. A1, we plot the gas temperature for this case coming from a CLOUDY numerical simulation (dashed line) and compare it to the gas profile we obtain from our analytical model (solid line). We find that our analytical model well reproduces the overall shape of the gas profile.

APPENDIX B: NLTE CALCULATIONS

Deriving a total gas mass from an observed integrated line flux for a particular transition of a given species requires knowledge of the fractional population of the upper energy level of the transition. In

other words, we need to know the fraction of mass populating the upper level in question relative to the total mass of the species. Non-local thermodynamic equilibrium treatment of the excitation of gas species is crucial for calculating these fractional level populations in low density astrophysical environments, where the density of collisional partners is likely to drop below the critical density necessary for the LTE approximation to be valid. Here, based on the formalism developed in Matrà et al. (2015) for the CO molecule, we extend our excitation code to solve the full NLTE statistical equilibrium for atomic species O I, C I and C II. Given the local radiation field $J_{\nu_{ul}}$ at the frequency of each transition between any two upper (u) and lower (l) levels, the density of main collisional partners n_{coll} and the kinetic temperature of the gas T_{kin}, the code solves the statistical equilibrium and outputs the fractional population x_i of all energy levels i of the species considered. We direct the reader to section 2 in Matrà et al. (2015) for a more extensive description of the method and the theory behind it.

For each species, we obtain energy levels, transition frequencies and Einstein coefficients from the Leiden Atomic and Molecular DAtabase (Schöier et al. 2005). In addition, we assume electrons released from carbon photoionization to be the dominant collisional partner (see Section 6), and obtain collisional rate coefficients from the same data base. The radiation field $J_{\nu_{ul}}$ at the wavelengths of each transition between any two levels is made up of three contributions; the CMB, the dust emission and the stellar emission. The stellar emission is calculated using stellar models matching the spectral type of the star as described in Section 3.2, whereas the radiation field due to dust emission is calculated using the RADMC-3D code[7] for the best-fitting model to high-resolution 1.3 mm observations of the β Pictoris disc (Matrà et al. in preparation). We then assume that the spatial distribution of dust emission is independent of wavelength (i.e. there is no spatial segregation of grains), and calculate the radiation field at other wavelengths by simply scaling it using fluxes from the SED (Kennedy & Wyatt 2014). For other stars, we scale this radiation field up or down to match the total intensity predicted from the SED of the star at the given wavelength. Fig. B1 shows an example comparison of the stellar, CMB and dust contributions for the β Pictoris disc as a function of distance from the central star, for transitions of the species relevant to this work. As expected, we see that the CMB dominates the radiation field at long mm wavelengths, with the dust contribution from the β Pic belt becoming more important already at 610 μm and shorter wavelengths. The stellar contribution, on the other hand, only becomes comparable to that of the dust within a few au from the star.

Given this total radiation field for all transitions, the assumed electron density and temperature as discussed in Sections 3.5.1 and 3.5.3, we solve the full NLTE statistical equilibrium for O I, C I and C II to derive the fractional level population x_i for all levels i of each species. For a given observed transition, the upper level fractional population can then be used through equation (8) to derive a gas mass from an observed flux, and vice versa.

---

[7] http://www.ita.uni-heidelberg.de/dullemond/software/radmc-3d
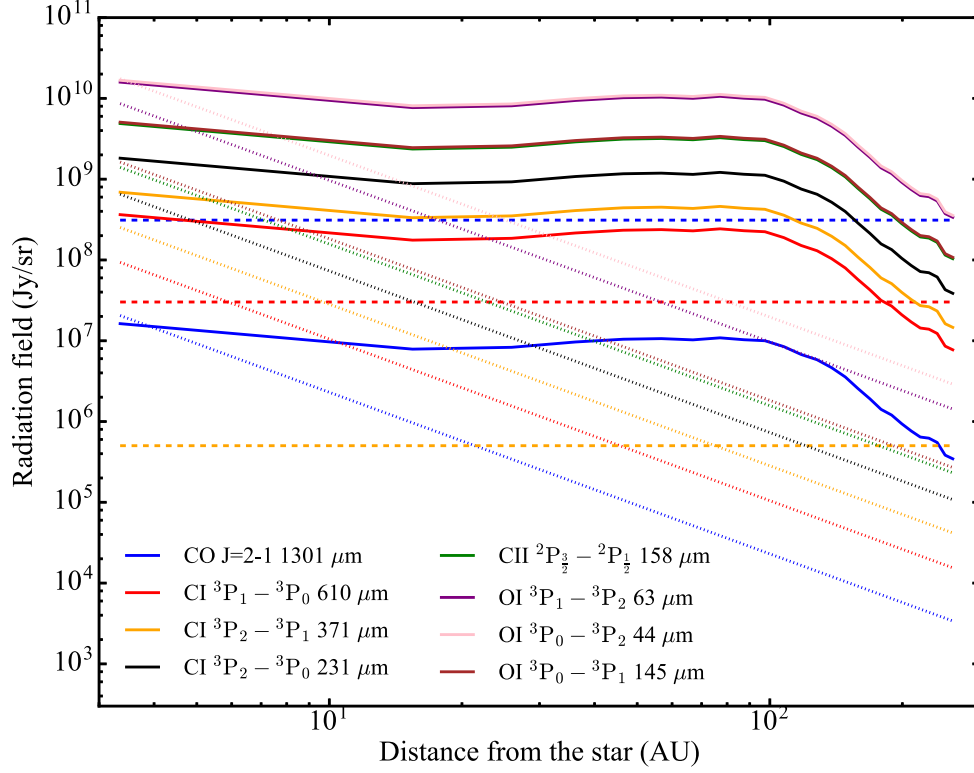
Figure B1. Radiation field impinging for different species assuming a β Pic like dust and star emission. Solid lines are for dust radiation, dashed for the CMB and dotted for star's radiation at the transition wavelength.

APPENDIX C: TABLES DESCRIBING OUR SAMPLE OF 189 STARS AND GIVING OUR PREDICTIONS FOR EACH STAR

Table C1. Description of the 189 stars used in this study.

Name	d (pc)	T_{eff} (K)	L_* ($L_\odot$)	L_{IR}/L_*	R_0 (au)	F_{60} (Jy)	F_{160} (Jy)	F_{610} (Jy)
β Pic	19.4	7405	8.7	1.7×10^{-03}	85	$1.3 \times 10^{+01}$	$4.1 \times 10^{+00}$	1.7×10^{-01}
η Tel	48.2	9379	22	7.6×10^{-04}	24	4.7×10^{-01}	7.6×10^{-02}	2.0×10^{-03}
49 Ceti	59.4	8922	15.5	1.1×10^{-03}	100	$1.8 \times 10^{+00}$	$1.1 \times 10^{+00}$	3.7×10^{-02}
HD 110058	107	8006	5.9	1.9×10^{-03}	50	3.7×10^{-01}	4.8×10^{-02}	1.2×10^{-03}
HD 131835	122	7984	9.2	1.5×10^{-03}	50	6.3×10^{-01}	3.7×10^{-01}	2.3×10^{-02}
HD 138813	150.8	8941	24.5	1.5×10^{-04}	100	4.1×10^{-01}	6.7×10^{-02}	1.7×10^{-03}
HD 146897	122.7	6256	3.1	5.4×10^{-03}	100	6.6×10^{-01}	1.0×10^{-01}	2.8×10^{-03}
HD 156623	118	8576	14.8	5.5×10^{-03}	75	9.8×10^{-01}	1.1×10^{-01}	2.7×10^{-03}
HD 172555	29	7120	7.8	7.8×10^{-04}	6	3.2×10^{-01}	2.9×10^{-02}	8.1×10^{-04}
HD 181327	51.8	6507	3.1	2.0×10^{-03}	85	$1.4 \times 10^{+00}$	9.3×10^{-01}	8.7×10^{-02}
HD 21997	71.9	8412	14.4	5.9×10^{-04}	60	6.0×10^{-01}	4.3×10^{-01}	2.5×10^{-02}
HD 32297	112	7676	5.6	5.4×10^{-03}	110	$1.0 \times 10^{+00}$	5.2×10^{-01}	4.5×10^{-02}
AU Mic	9.91	3280	0.0878	3.9×10^{-04}	107	1.8×10^{-01}	1.8×10^{-01}	2.6×10^{-02}
CE Ant	19.2	3592	0.0463	1.7×10^{-03}	42	9.2×10^{-02}	4.4×10^{-02}	1.7×10^{-03}
Fomalhaut A	7.7	8579	16.5	7.1×10^{-05}	138	$9.7 \times 10^{+00}$	$5.9 \times 10^{+00}$	2.2×10^{-01}
Fomalhaut C	11.2	3239	0.0112	1.4×10^{-04}	387	3.1×10^{-03}	2.1×10^{-02}	2.5×10^{-03}
HD 10008	24	5336	0.465	7.0×10^{-05}	59.4	3.2×10^{-02}	6.7×10^{-03}	2.2×10^{-04}
HD 102647	11	8560	13.9	2.1×10^{-05}	53.2	9.2×10^{-01}	1.6×10^{-01}	5.2×10^{-03}
HD 102870	10.9	6185	3.58	6.7×10^{-07}	670	1.4×10^{-01}	4.6×10^{-02}	3.7×10^{-03}
HD 103703	98.9	6536	3.2	2.9×10^{-04}	11.1	5.2×10^{-03}	4.8×10^{-04}	1.8×10^{-05}
HD 104600	106	10000	48.5	1.1×10^{-04}	47.3	1.1×10^{-01}	1.5×10^{-02}	3.9×10^{-04}
HD 10472	67.2	6751	3.3	2.6×10^{-04}	168	1.3×10^{-01}	4.5×10^{-02}	1.7×10^{-03}

Table C1 – *continued*

Name	d (pc)	$T_{\rm eff}$ (K)	L_* (L$_\odot$)	$L_{\rm IR}/L_*$	R_0 (au)	F_{60} (Jy)	F_{160} (Jy)	F_{610} (Jy)
HD 104860	45.5	5990	1.19	6.1×10^{-04}	200	1.5×10^{-01}	2.3×10^{-01}	1.5×10^{-02}
HD 105	39.4	6024	1.29	2.9×10^{-04}	153	1.2×10^{-01}	1.2×10^{-01}	5.8×10^{-03}
HD 105211	19.8	7030	6.91	3.6×10^{-05}	239	4.5×10^{-01}	2.1×10^{-01}	8.6×10^{-03}
HD 106036	101	8625	14	3.0×10^{-04}	20.5	3.2×10^{-02}	2.9×10^{-03}	7.7×10^{-05}
HD 10638	69.3	7625	7.77	4.2×10^{-04}	218	3.5×10^{-01}	3.1×10^{-01}	1.2×10^{-02}
HD 10647	17.4	6183	1.57	3.8×10^{-04}	105	9.4×10^{-01}	6.3×10^{-01}	7.7×10^{-02}
HD 106797	96	9552	34.7	1.6×10^{-04}	24.2	4.7×10^{-02}	4.4×10^{-03}	1.2×10^{-04}
HD 106906	92.1	6515	5.28	1.4×10^{-03}	63.8	3.4×10^{-01}	5.1×10^{-02}	1.4×10^{-03}
HD 10700	3.65	5478	0.492	7.4×10^{-06}	75.6	3.6×10^{-01}	1.1×10^{-01}	1.1×10^{-02}
HD 107146	27.5	5902	0.999	1.2×10^{-03}	244	5.6×10^{-01}	$1.2 \times 10^{+00}$	7.7×10^{-02}
HD 107649	93.7	6423	2.07	1.5×10^{-04}	27.9	8.5×10^{-03}	2.3×10^{-03}	6.1×10^{-05}
HD 108857	97	5943	3.18	4.8×10^{-04}	11.5	8.9×10^{-03}	8.1×10^{-04}	2.8×10^{-05}
HD 109085	18.3	6802	5.21	1.4×10^{-05}	340	2.5×10^{-01}	2.1×10^{-01}	2.8×10^{-02}
HD 109832	112	6930	5.9	4.9×10^{-04}	50	7.6×10^{-02}	1.2×10^{-02}	3.1×10^{-04}
HD 110897	17.4	5929	1.1	1.9×10^{-05}	111	5.2×10^{-02}	2.8×10^{-02}	1.3×10^{-03}
HD 111520	109	6353	2.5	1.6×10^{-03}	188	2.1×10^{-01}	8.7×10^{-02}	3.4×10^{-03}
HD 111631	10.6	3927	0.0917	1.3×10^{-05}	588	1.6×10^{-02}	1.9×10^{-02}	2.5×10^{-03}
HD 11171	23.2	7102	5.83	5.7×10^{-06}	382	5.0×10^{-02}	5.8×10^{-02}	1.0×10^{-02}
HD 112429	29.3	7186	5.65	1.8×10^{-05}	65.6	6.6×10^{-02}	1.1×10^{-02}	4.1×10^{-04}
HD 114082	85.5	6637	3.07	3.3×10^{-03}	40.8	4.0×10^{-01}	1.3×10^{-01}	3.4×10^{-03}
HD 115617	8.56	5609	0.833	3.0×10^{-05}	82.2	2.3×10^{-01}	1.0×10^{-01}	1.2×10^{-02}
HD 117214	110	6341	5.91	2.5×10^{-03}	45.2	3.6×10^{-01}	5.3×10^{-02}	1.3×10^{-03}
HD 118972	15.7	5215	0.403	4.0×10^{-05}	43.7	3.8×10^{-02}	6.4×10^{-03}	2.4×10^{-04}
HD 119124	25.3	6189	1.59	7.2×10^{-05}	91	8.6×10^{-02}	1.8×10^{-02}	6.2×10^{-04}
HD 119718	132	6534	9.13	2.6×10^{-04}	33.1	2.0×10^{-02}	2.2×10^{-03}	6.3×10^{-05}
HD 120534	73.7	7252	6.79	4.0×10^{-04}	80.6	2.3×10^{-01}	3.9×10^{-02}	1.1×10^{-03}
HD 121189	119	6603	3.78	3.7×10^{-04}	25.4	1.2×10^{-02}	1.2×10^{-03}	3.5×10^{-05}
HD 121191	151	7724	9.59	2.7×10^{-03}	12.1	8.1×10^{-02}	1.7×10^{-02}	4.7×10^{-04}
HD 122652	39.3	6222	1.75	1.2×10^{-04}	123	8.9×10^{-02}	2.5×10^{-02}	8.8×10^{-04}
HD 12467	70.6	8297	16	1.1×10^{-04}	172	2.0×10^{-01}	7.0×10^{-02}	2.4×10^{-03}
HD 124718	63.2	5639	0.969	1.8×10^{-03}	107	2.1×10^{-01}	1.5×10^{-01}	6.6×10^{-03}
HD 125451	26.1	6748	3.85	1.6×10^{-05}	110	6.7×10^{-02}	1.6×10^{-02}	6.1×10^{-04}
HD 125541	113	7245	2.9	2.1×10^{-04}	24.8	6.2×10^{-03}	6.4×10^{-04}	1.9×10^{-05}
HD 126265	70.4	5987	5.46	3.5×10^{-04}	78.3	1.8×10^{-01}	3.1×10^{-02}	9.1×10^{-04}
HD 127821	31.8	6616	3.03	2.0×10^{-04}	210	2.8×10^{-01}	2.9×10^{-01}	1.2×10^{-02}
HD 129590	133	5836	2.79	5.7×10^{-03}	59.7	3.6×10^{-01}	6.7×10^{-02}	1.8×10^{-03}
HD 131885	123	8913	23.6	5.4×10^{-04}	136	3.6×10^{-01}	7.9×10^{-02}	2.4×10^{-03}
HD 132254	25.1	6286	2.9	9.5×10^{-06}	73.6	3.4×10^{-02}	5.3×10^{-03}	2.5×10^{-04}
HD 13246	44.2	6189	1.63	3.8×10^{-05}	81.5	2.9×10^{-02}	8.0×10^{-03}	2.4×10^{-04}
HD 133803	125	6984	6.94	3.8×10^{-04}	18.9	2.2×10^{-02}	5.0×10^{-03}	1.2×10^{-04}
HD 134888	89.9	6429	2.01	7.3×10^{-04}	67.8	8.1×10^{-02}	1.7×10^{-02}	4.8×10^{-04}
HD 135599	15.8	5262	0.388	1.1×10^{-04}	75	1.0×10^{-01}	2.7×10^{-02}	8.8×10^{-04}
HD 135953	133	6242	2.58	7.3×10^{-04}	120	5.1×10^{-02}	3.6×10^{-02}	3.7×10^{-03}
HD 136482	136	10000	39.7	3.6×10^{-05}	59.9	3.1×10^{-02}	8.6×10^{-03}	2.9×10^{-04}
HD 137057	169	6634	9.75	2.5×10^{-04}	34.3	1.2×10^{-02}	1.3×10^{-03}	3.9×10^{-05}
HD 138923	106	10000	34.8	1.1×10^{-04}	9.83	1.1×10^{-02}	9.7×10^{-04}	4.0×10^{-05}
HD 138965	78.5	8849	13.7	4.1×10^{-04}	160	4.5×10^{-01}	3.3×10^{-01}	1.4×10^{-02}
HD 139006	23	9287	60.2	1.6×10^{-05}	49.6	5.8×10^{-01}	7.5×10^{-02}	2.6×10^{-03}
HD 139664	17.4	6728	3.46	8.0×10^{-05}	124	5.6×10^{-01}	1.5×10^{-01}	5.0×10^{-03}
HD 140817	147	9047	36.9	1.4×10^{-04}	22.8	2.9×10^{-02}	3.0×10^{-03}	8.1×10^{-05}
HD 14082B	27.3	5843	0.487	2.0×10^{-04}	37.8	4.8×10^{-02}	7.9×10^{-03}	2.2×10^{-04}
HD 140840	126	10000	18.4	1.9×10^{-04}	73	8.3×10^{-02}	1.5×10^{-02}	4.0×10^{-04}
HD 141943	38.8	5808	0.935	1.1×10^{-04}	56.7	3.2×10^{-02}	6.2×10^{-03}	1.9×10^{-04}
HD 143675	113	7932	6.2	5.4×10^{-04}	27.5	5.1×10^{-02}	5.4×10^{-03}	1.3×10^{-04}
HD 144981	170	7538	14.1	2.1×10^{-04}	12.1	7.9×10^{-03}	7.1×10^{-04}	2.3×10^{-05}
HD 145229	34.5	5966	1.07	1.1×10^{-04}	104	5.2×10^{-02}	3.3×10^{-02}	1.1×10^{-03}
HD 1461	23.2	5773	1.2	4.5×10^{-05}	89	6.5×10^{-02}	1.6×10^{-02}	5.5×10^{-04}
HD 147594	142	5681	3.34	1.2×10^{-04}	17.7	2.5×10^{-03}	2.7×10^{-04}	1.2×10^{-05}
HD 151044	29.3	6157	1.86	6.4×10^{-05}	124	8.8×10^{-02}	2.9×10^{-02}	1.0×10^{-03}
HD 15115	45.2	6666	3.26	4.7×10^{-04}	167	3.9×10^{-01}	2.7×10^{-01}	9.8×10^{-03}
HD 151376	136	6231	3.67	3.4×10^{-04}	6.34	3.5×10^{-03}	6.0×10^{-04}	2.1×10^{-05}

Table C1 – *continued*

Name	d (pc)	T_{eff} (K)	L_* ($L_\odot$)	L_{IR}/L_*	R_0 (au)	F_{60} (Jy)	F_{160} (Jy)	F_{610} (Jy)
HD 15257	49.8	7295	14.7	9.4×10^{-05}	340	2.8×10^{-01}	4.3×10^{-01}	2.5×10^{-02}
HD 15745	63.5	6870	3.34	2.0×10^{-03}	62.6	6.3×10^{-01}	2.5×10^{-01}	2.3×10^{-02}
HD 157728	42.7	7726	7.67	1.4×10^{-04}	139	5.2×10^{-01}	1.1×10^{-01}	3.5×10^{-03}
HD 158633	12.8	5331	0.418	2.3×10^{-05}	135	5.1×10^{-02}	1.9×10^{-02}	8.0×10^{-04}
HD 159492	44.6	7916	12.5	1.2×10^{-04}	47.6	2.1×10^{-01}	5.5×10^{-02}	1.4×10^{-03}
HD 161868	31.5	8923	26.1	8.3×10^{-05}	148	$1.2 \times 10^{+00}$	5.8×10^{-01}	1.8×10^{-02}
HD 164249	48.1	6295	3.12	8.7×10^{-04}	101	5.8×10^{-01}	1.9×10^{-01}	6.0×10^{-03}
HD 165908	15.6	5951	2.06	1.4×10^{-05}	195	9.2×10^{-02}	7.2×10^{-02}	4.9×10^{-03}
HD 165908B	7.19	4592	0.19	4.5×10^{-05}	120	1.2×10^{-01}	9.1×10^{-02}	4.6×10^{-03}
HD 166	13.7	5515	0.629	6.8×10^{-05}	53.7	1.2×10^{-01}	2.6×10^{-02}	8.4×10^{-04}
HD 16743	58.9	6979	5.38	3.5×10^{-04}	183	2.9×10^{-01}	2.1×10^{-01}	7.7×10^{-03}
HD 169666	53.2	6565	4.91	2.1×10^{-04}	9.73	2.8×10^{-02}	2.8×10^{-03}	9.8×10^{-05}
HD 170773	37	6697	3.62	5.3×10^{-04}	241	5.8×10^{-01}	9.1×10^{-01}	6.7×10^{-02}
HD 17390	48	6918	4.71	1.7×10^{-04}	222	2.1×10^{-01}	1.2×10^{-01}	4.7×10^{-03}
HD 17925	10.4	5145	0.401	2.2×10^{-05}	122	7.1×10^{-02}	3.0×10^{-02}	1.2×10^{-03}
HD 182681	69.9	9621	25.6	2.7×10^{-04}	98.3	5.8×10^{-01}	2.6×10^{-01}	1.3×10^{-02}
HD 191089	52.2	6513	3.01	1.4×10^{-03}	56.8	5.5×10^{-01}	2.2×10^{-01}	1.2×10^{-02}
HD 191849	6.2	3786	0.0532	1.2×10^{-05}	530	2.9×10^{-02}	2.6×10^{-02}	1.0×10^{-02}
HD 192758	68.5	7149	5.87	5.5×10^{-04}	136	3.5×10^{-01}	1.8×10^{-01}	6.1×10^{-03}
HD 195627	27.8	7278	7.66	6.0×10^{-05}	168	3.1×10^{-01}	2.5×10^{-01}	3.2×10^{-02}
HD 199260	22	6323	2.12	1.8×10^{-05}	58.8	4.8×10^{-02}	1.5×10^{-02}	6.1×10^{-04}
HD 201219	38.1	5663	0.796	1.2×10^{-04}	107	3.8×10^{-02}	1.5×10^{-02}	5.2×10^{-04}
HD 202628	24.4	5815	1.03	1.0×10^{-04}	151	9.0×10^{-02}	8.9×10^{-02}	4.4×10^{-03}
HD 202917	43	5508	0.594	2.5×10^{-04}	57.8	3.8×10^{-02}	7.9×10^{-03}	2.3×10^{-04}
HD 203	39.4	6854	4.22	1.1×10^{-04}	30.2	7.4×10^{-02}	1.3×10^{-02}	3.5×10^{-04}
HD 205674	51.8	6753	2.93	3.5×10^{-04}	149	1.9×10^{-01}	1.6×10^{-01}	1.1×10^{-02}
HD 206860	17.9	5989	1.13	9.9×10^{-06}	51.3	3.0×10^{-02}	7.5×10^{-03}	5.9×10^{-04}
HD 206893	38.3	6608	2.55	2.7×10^{-04}	183	2.3×10^{-01}	2.1×10^{-01}	8.1×10^{-03}
HD 207129	16	5977	1.28	8.0×10^{-05}	162	2.2×10^{-01}	1.8×10^{-01}	1.8×10^{-02}
HD 218340	56.6	5904	1.16	1.2×10^{-04}	121	2.6×10^{-02}	9.0×10^{-03}	3.2×10^{-04}
HD 218511	15	4307	0.159	1.8×10^{-05}	374	1.2×10^{-02}	1.4×10^{-02}	1.1×10^{-03}
HD 219482	20.5	6302	1.92	3.4×10^{-05}	51.5	7.6×10^{-02}	1.4×10^{-02}	4.8×10^{-04}
HD 219623	20.5	6196	2.04	1.8×10^{-05}	57.6	5.6×10^{-02}	9.5×10^{-03}	3.7×10^{-04}
HD 22049	3.22	5099	0.336	9.3×10^{-05}	84.9	$1.7 \times 10^{+00}$	$1.0 \times 10^{+00}$	1.0×10^{-01}
HD 221354	16.9	5253	0.543	8.5×10^{-04}	141	8.9×10^{-01}	3.7×10^{-01}	1.4×10^{-02}
HD 22179	68.9	5867	1.12	2.8×10^{-04}	82.2	3.5×10^{-02}	8.7×10^{-03}	2.7×10^{-04}
HD 221853	68.4	6785	4.32	7.8×10^{-04}	70.2	2.9×10^{-01}	1.2×10^{-01}	3.3×10^{-03}
HD 223340	44	5259	0.427	3.9×10^{-04}	72.5	4.2×10^{-02}	2.3×10^{-02}	7.5×10^{-04}
HD 22484	14	6036	3.16	1.1×10^{-05}	51.5	1.4×10^{-01}	2.9×10^{-02}	1.2×10^{-03}
HD 2262	23.8	8011	11.9	7.9×10^{-06}	43.3	8.7×10^{-02}	1.2×10^{-02}	5.4×10^{-04}
HD 23484	16	5169	0.401	9.8×10^{-05}	125	8.2×10^{-02}	7.4×10^{-02}	6.5×10^{-03}
HD 24636	54.1	6781	3.35	1.1×10^{-04}	41.2	4.0×10^{-02}	5.8×10^{-03}	1.7×10^{-04}
HD 25457	18.8	6307	2.06	7.4×10^{-05}	143	2.8×10^{-01}	1.5×10^{-01}	5.3×10^{-03}
HD 25998	21	6317	2.25	2.6×10^{-05}	77.3	7.7×10^{-02}	1.3×10^{-02}	4.9×10^{-04}
HD 27290	20.5	7224	6.57	1.9×10^{-05}	128	1.8×10^{-01}	1.0×10^{-01}	9.6×10^{-03}
HD 274255	18.8	4025	0.0892	1.8×10^{-04}	81.2	3.0×10^{-02}	8.6×10^{-03}	3.1×10^{-04}
HD 27638B	45.3	5616	0.69	3.3×10^{-04}	127	6.1×10^{-02}	2.1×10^{-02}	7.7×10^{-04}
HD 30447	80.3	6760	3.75	9.0×10^{-04}	143	2.6×10^{-01}	2.0×10^{-01}	1.9×10^{-02}
HD 30495	13.3	5835	0.971	2.3×10^{-05}	147	9.6×10^{-02}	4.7×10^{-02}	1.9×10^{-03}
HD 3126	40.9	6468	2.38	1.2×10^{-04}	115	1.0×10^{-01}	3.0×10^{-02}	1.0×10^{-03}
HD 31392	25.2	5367	0.533	1.3×10^{-04}	253	5.4×10^{-02}	5.8×10^{-02}	3.0×10^{-03}
HD 33636	28.4	5978	1.08	3.6×10^{-05}	191	2.9×10^{-02}	2.2×10^{-02}	9.5×10^{-04}
HD 34324	74.6	8231	9.07	8.7×10^{-05}	378	1.1×10^{-01}	7.6×10^{-02}	3.8×10^{-03}
HD 35650	18	4195	0.126	1.5×10^{-04}	99.7	3.3×10^{-02}	2.7×10^{-02}	1.0×10^{-03}
HD 35841	103	6585	2.39	1.2×10^{-03}	102	1.3×10^{-01}	8.0×10^{-02}	9.0×10^{-03}
HD 35850	27	6090	1.87	3.0×10^{-05}	88.4	4.7×10^{-02}	2.2×10^{-02}	2.4×10^{-03}
HD 3670	86.8	6492	3.16	4.7×10^{-04}	168	1.1×10^{-01}	5.8×10^{-02}	2.1×10^{-03}
HD 36968	145	6839	4.01	1.2×10^{-03}	142	1.2×10^{-01}	4.6×10^{-02}	1.6×10^{-03}
HD 37484	56.8	6742	3.27	1.3×10^{-04}	148	1.2×10^{-01}	3.2×10^{-02}	1.1×10^{-03}
HD 37594	42.6	7247	6.01	2.5×10^{-04}	150	4.2×10^{-01}	2.7×10^{-01}	9.1×10^{-03}

Table C1 – *continued*

Name	d (pc)	T_{eff} (K)	L_* ($L_\odot$)	L_{IR}/L_*	R_0 (au)	F_{60} (Jy)	F_{160} (Jy)	F_{610} (Jy)
HD 377	39.1	5876	1.2	3.2×10^{-04}	92.2	1.2×10^{-01}	7.4×10^{-02}	8.9×10^{-03}
HD 38206	75.1	9850	27.3	1.4×10^{-04}	153	3.5×10^{-01}	1.8×10^{-01}	5.8×10^{-03}
HD 38207	94.4	6794	2.96	7.5×10^{-04}	181	1.5×10^{-01}	7.2×10^{-02}	2.7×10^{-03}
HD 38678	21.6	8477	15	8.9×10^{-05}	20.9	3.9×10^{-01}	3.7×10^{-02}	1.2×10^{-03}
HD 38858	15.2	5780	0.829	8.7×10^{-05}	112	1.7×10^{-01}	1.2×10^{-01}	1.6×10^{-02}
HD 40136	14.9	7108	5.83	1.1×10^{-05}	23.8	1.2×10^{-01}	1.6×10^{-02}	8.2×10^{-04}
HD 40540	81	7262	4.69	3.5×10^{-04}	102	1.4×10^{-01}	7.2×10^{-02}	2.2×10^{-03}
HD 45184	21.9	5859	1.16	8.9×10^{-05}	108	1.2×10^{-01}	6.2×10^{-02}	2.1×10^{-03}
HD 50554	29.9	6030	1.38	4.5×10^{-05}	100	4.0×10^{-02}	2.2×10^{-02}	2.2×10^{-03}
HD 50571	33.6	6601	3.29	1.2×10^{-04}	181	2.0×10^{-01}	9.7×10^{-02}	3.7×10^{-03}
HD 52265	29	6143	2.11	2.5×10^{-05}	75.8	3.8×10^{-02}	1.5×10^{-02}	6.0×10^{-04}
HD 53143	18.3	5415	0.581	1.7×10^{-04}	53.4	1.4×10^{-01}	2.3×10^{-02}	7.1×10^{-04}
HD 54341	102	9757	26.7	2.0×10^{-04}	167	2.7×10^{-01}	9.2×10^{-02}	3.0×10^{-03}
HD 59967	21.8	5826	0.894	2.8×10^{-05}	81.1	3.7×10^{-02}	8.6×10^{-03}	3.1×10^{-04}
HD 60491	24.6	5037	0.337	1.7×10^{-04}	56.4	4.7×10^{-02}	1.1×10^{-02}	3.4×10^{-04}
HD 61005	35.3	5491	0.584	2.2×10^{-03}	100	4.8×10^{-01}	3.6×10^{-01}	3.0×10^{-02}
HD 6798	82.8	9095	35.2	1.4×10^{-04}	115	3.2×10^{-01}	1.5×10^{-01}	1.6×10^{-02}
HD 6963	27.1	5549	0.569	8.6×10^{-05}	94.7	4.1×10^{-02}	1.3×10^{-02}	4.3×10^{-04}
HD 69830	12.5	5439	0.597	2.7×10^{-04}	2.8	3.5×10^{-02}	4.1×10^{-03}	2.4×10^{-04}
HD 71722	69.4	8924	16.6	9.0×10^{-05}	116	1.6×10^{-01}	4.5×10^{-02}	1.4×10^{-03}
HD 72905	14.4	5899	0.987	1.1×10^{-05}	59.5	4.8×10^{-02}	8.0×10^{-03}	3.5×10^{-04}
HD 73350	24	5818	0.989	1.3×10^{-04}	126	1.2×10^{-01}	9.6×10^{-02}	3.4×10^{-03}
HD 7590	23.2	5996	1.05	1.6×10^{-04}	167	1.9×10^{-01}	9.7×10^{-02}	3.8×10^{-03}
HD 76151	17.4	5815	1.03	1.4×10^{-05}	52.6	3.7×10^{-02}	5.9×10^{-03}	2.6×10^{-04}
HD 76543	45.7	8145	13.2	1.2×10^{-04}	108	3.4×10^{-01}	1.7×10^{-01}	5.0×10^{-03}
HD 76582	46.1	7758	8.88	2.7×10^{-04}	129	5.4×10^{-01}	3.4×10^{-01}	3.1×10^{-02}
HD 80950	82	9681	28.1	8.1×10^{-05}	30.8	6.8×10^{-02}	1.6×10^{-02}	5.0×10^{-04}
HD 82443	17.8	5294	0.458	5.1×10^{-05}	35.4	3.5×10^{-02}	5.5×10^{-03}	2.0×10^{-04}
HD 82943	27.5	5987	1.52	1.1×10^{-04}	125	1.2×10^{-01}	9.0×10^{-02}	3.1×10^{-03}
HD 84075	68	5991	1.47	2.0×10^{-04}	90.7	3.4×10^{-02}	9.1×10^{-03}	2.9×10^{-04}
HD 84870	88	7482	7.65	2.6×10^{-04}	291	1.5×10^{-01}	2.0×10^{-01}	1.6×10^{-02}
HD 85672	107	8096	8.39	5.3×10^{-04}	95	1.9×10^{-01}	3.7×10^{-02}	1.1×10^{-03}
HD 86087	92.9	9465	39.8	3.5×10^{-04}	111	6.9×10^{-01}	3.2×10^{-01}	1.2×10^{-02}
HD 87696	28.2	7920	10.3	1.6×10^{-05}	19.7	5.3×10^{-02}	9.7×10^{-03}	3.9×10^{-04}
HD 8907	34.8	6323	2.17	2.5×10^{-04}	173	2.1×10^{-01}	2.3×10^{-01}	2.1×10^{-02}
HD 90089	21.5	6714	3.07	1.0×10^{-05}	463	3.6×10^{-02}	7.3×10^{-02}	1.4×10^{-02}
HD 92945	21.4	5118	0.37	6.6×10^{-04}	184	2.2×10^{-01}	3.4×10^{-01}	2.4×10^{-02}
HD 95086	90.4	7416	6.97	1.2×10^{-03}	126	5.0×10^{-01}	3.2×10^{-01}	3.9×10^{-02}
HD 95418	24.4	9255	59.3	1.5×10^{-05}	69	5.4×10^{-01}	7.0×10^{-02}	2.5×10^{-03}
HD 95698	56.1	7127	8.19	1.1×10^{-04}	135	1.4×10^{-01}	9.1×10^{-02}	3.0×10^{-03}
HIP 11437	40	4283	0.223	1.0×10^{-03}	71.4	6.9×10^{-02}	4.2×10^{-02}	1.4×10^{-03}
HIP 1368	15	3975	0.108	1.1×10^{-04}	302	1.8×10^{-02}	6.4×10^{-02}	5.2×10^{-03}
HIP 32480	16.7	6048	1.88	7.0×10^{-05}	163	2.6×10^{-01}	2.0×10^{-01}	7.8×10^{-03}
HIP 43534	16.5	4151	0.0995	2.6×10^{-04}	376	1.6×10^{-02}	1.1×10^{-01}	3.2×10^{-02}
HIP 63942	18.8	4087	0.118	1.9×10^{-04}	88.6	4.1×10^{-02}	1.4×10^{-02}	5.2×10^{-04}
HIP 74995	6.3	3245	0.0121	7.0×10^{-05}	137	1.5×10^{-02}	2.0×10^{-02}	1.0×10^{-03}
HR 4796	72.8	8763	23.4	4.9×10^{-03}	56.8	$6.3 \times 10^{+00}$	$1.6 \times 10^{+00}$	4.1×10^{-02}

Column 1: star's name. *Column 2:* distance to Earth (in pc). *Column 3:* star's temperature (in K). *Column 4:* star's luminosity (in $L_\odot$). *Column 5:* dust fractional luminosity. *Column 6:* location of the belt (au). *Columns 7–9:* flux at 60, 160, 610 microns (in W m^{-2}).

Table C2. Model predictions for the 189 stars used in this study (masses are in $M_\oplus$ and fluxes in W m^{-2}).

Name	M_{CO} ($M_\oplus$)	$F_{CO\ 1300}$ (W m^{-2})	$F_{CO\ 870}$ (W m^{-2})	$M_{C\,I}$ ($M_\oplus$)	$F_{C\,I\ 610}$ (W m^{-2})	$M_{C\,II}$ ($M_\oplus$)	$F_{C\,II\ 158}$ (W m^{-2})	$M_{O\,I}$ ($M_\oplus$)	$F_{O\,I\ 63}$ (W m^{-2})
β Pic	4.6×10^{-05}	2.4×10^{-20}	1.9×10^{-20}	3.4×10^{-03}	2.3×10^{-19}	3.8×10^{-04}	6.9×10^{-18}	1.5×10^{-02}	1.4×10^{-17}
η Tel	8.5×10^{-08}	1.1×10^{-23}	4.9×10^{-23}	1.1×10^{-03}	2.1×10^{-20}	5.6×10^{-04}	4.0×10^{-19}	6.6×10^{-03}	1.6×10^{-18}
49 Ceti	4.0×10^{-06}	3.6×10^{-22}	3.7×10^{-22}	2.2×10^{-03}	4.9×10^{-20}	1.0×10^{-03}	1.8×10^{-18}	1.3×10^{-02}	3.2×10^{-18}
HD 110058	1.9×10^{-04}	9.5×10^{-22}	1.3×10^{-21}	2.6×10^{-03}	5.4×10^{-21}	1.3×10^{-04}	8.1×10^{-20}	1.1×10^{-02}	3.0×10^{-19}
HD 131835	2.6×10^{-05}	5.6×10^{-22}	8.5×10^{-22}	2.7×10^{-03}	1.4×10^{-20}	1.7×10^{-04}	8.8×10^{-20}	1.2×10^{-02}	8.5×10^{-19}
HD 138813	2.5×10^{-06}	4.2×10^{-23}	1.0×10^{-22}	6.7×10^{-03}	2.0×10^{-20}	4.0×10^{-03}	5.7×10^{-19}	4.3×10^{-02}	1.2×10^{-18}
HD 146897	2.9×10^{-03}	1.1×10^{-21}	1.4×10^{-21}	1.0×10^{-02}	5.7×10^{-21}	4.6×10^{-04}	1.9×10^{-19}	4.3×10^{-02}	3.3×10^{-19}
HD 156623	1.2×10^{-03}	5.7×10^{-21}	1.2×10^{-20}	7.0×10^{-02}	4.3×10^{-20}	3.9×10^{-03}	8.3×10^{-19}	3.0×10^{-01}	3.0×10^{-18}
HD 172555	3.2×10^{-04}	1.9×10^{-21}	3.2×10^{-21}	4.9×10^{-05}	1.2×10^{-20}	4.4×10^{-07}	2.2×10^{-20}	2.0×10^{-04}	2.5×10^{-17}
HD 181327	2.6×10^{-05}	1.2×10^{-21}	6.1×10^{-22}	1.3×10^{-03}	9.6×10^{-21}	2.2×10^{-04}	5.3×10^{-19}	6.0×10^{-03}	5.5×10^{-19}
HD 21997	6.8×10^{-07}	4.6×10^{-23}	6.1×10^{-23}	5.4×10^{-04}	1.5×10^{-20}	2.5×10^{-04}	3.4×10^{-19}	3.2×10^{-03}	1.3×10^{-18}
HD 32297	6.1×10^{-03}	1.8×10^{-21}	2.3×10^{-21}	2.2×10^{-02}	9.6×10^{-21}	1.3×10^{-03}	5.6×10^{-19}	9.4×10^{-02}	5.5×10^{-19}
AU Mic	4.8×10^{-09}	4.7×10^{-25}	8.4×10^{-27}	1.6×10^{-08}	6.3×10^{-25}	1.6×10^{-06}	3.3×10^{-21}	6.4×10^{-06}	3.1×10^{-22}
CE Ant	7.3×10^{-08}	9.9×10^{-24}	8.4×10^{-25}	6.0×10^{-06}	2.8×10^{-22}	5.5×10^{-06}	8.4×10^{-20}	4.6×10^{-05}	2.2×10^{-20}
Fomalhaut A	1.2×10^{-08}	3.4×10^{-24}	9.9×10^{-26}	3.1×10^{-07}	4.8×10^{-22}	3.1×10^{-05}	1.2×10^{-18}	1.2×10^{-04}	2.4×10^{-19}
Fomalhaut C	4.6×10^{-11}	3.3×10^{-27}	5.6×10^{-29}	1.6×10^{-08}	8.9×10^{-26}	6.6×10^{-09}	1.3×10^{-26}	8.9×10^{-08}	2.1×10^{-25}
HD 10008	1.2×10^{-09}	2.0×10^{-26}	3.7×10^{-28}	3.5×10^{-09}	5.1×10^{-27}	3.5×10^{-07}	2.4×10^{-22}	1.4×10^{-06}	1.1×10^{-23}
HD 102647	7.4×10^{-10}	1.3×10^{-25}	4.6×10^{-27}	1.1×10^{-07}	7.8×10^{-24}	1.7×10^{-06}	4.8×10^{-20}	7.4×10^{-06}	3.4×10^{-21}
HD 102870	4.3×10^{-13}	3.3×10^{-29}	5.6×10^{-31}	5.1×10^{-10}	5.1×10^{-27}	5.5×10^{-11}	2.2×10^{-28}	2.3×10^{-09}	1.3×10^{-26}
HD 103703	2.7×10^{-06}	5.4×10^{-23}	9.2×10^{-23}	3.1×10^{-05}	5.0×10^{-22}	7.7×10^{-07}	1.3×10^{-21}	1.3×10^{-04}	2.0×10^{-20}
HD 104600	4.8×10^{-09}	1.6×10^{-25}	2.9×10^{-25}	4.3×10^{-05}	8.7×10^{-22}	1.7×10^{-04}	1.1×10^{-19}	8.4×10^{-04}	2.4×10^{-19}
HD 10472	9.7×10^{-08}	2.8×10^{-25}	7.0×10^{-27}	1.9×10^{-05}	1.3×10^{-23}	4.4×10^{-05}	1.5×10^{-20}	2.5×10^{-04}	1.2×10^{-21}
HD 104860	1.6×10^{-07}	9.2×10^{-25}	2.0×10^{-26}	3.9×10^{-05}	1.1×10^{-22}	6.2×10^{-05}	3.4×10^{-20}	4.0×10^{-04}	3.2×10^{-21}
HD 105	4.3×10^{-08}	3.1×10^{-25}	6.7×10^{-27}	3.8×10^{-06}	8.8×10^{-24}	2.0×10^{-05}	1.3×10^{-20}	9.5×10^{-05}	8.0×10^{-22}
HD 105211	3.6×10^{-09}	8.5×10^{-26}	1.5×10^{-27}	1.1×10^{-06}	1.1×10^{-23}	2.1×10^{-06}	2.1×10^{-22}	1.2×10^{-05}	1.1×10^{-22}
HD 106036	5.4×10^{-08}	1.8×10^{-24}	7.9×10^{-24}	7.2×10^{-05}	1.8×10^{-21}	6.6×10^{-05}	1.5×10^{-19}	5.5×10^{-04}	1.1×10^{-18}
HD 10638	6.1×10^{-07}	2.2×10^{-24}	7.1×10^{-26}	3.1×10^{-04}	5.8×10^{-22}	1.7×10^{-04}	9.3×10^{-20}	1.9×10^{-03}	1.7×10^{-20}
HD 10647	1.1×10^{-07}	8.8×10^{-24}	3.9×10^{-25}	1.5×10^{-05}	9.0×10^{-22}	3.4×10^{-05}	4.2×10^{-19}	2.0×10^{-04}	5.2×10^{-20}
HD 106797	2.4×10^{-09}	8.5×10^{-26}	3.7×10^{-25}	5.8×10^{-05}	1.6×10^{-21}	1.5×10^{-04}	1.4×10^{-19}	8.1×10^{-04}	3.3×10^{-19}
HD 106906	2.7×10^{-05}	6.9×10^{-22}	7.8×10^{-22}	2.2×10^{-03}	6.5×10^{-21}	2.5×10^{-04}	2.0×10^{-19}	1.0×10^{-02}	3.7×10^{-19}
HD 10700	1.3×10^{-11}	8.6×10^{-27}	1.5×10^{-28}	4.3×10^{-11}	7.6×10^{-27}	4.3×10^{-09}	1.1×10^{-24}	1.7×10^{-08}	2.1×10^{-24}
HD 107146	4.8×10^{-07}	7.6×10^{-24}	1.7×10^{-25}	2.1×10^{-04}	6.4×10^{-21}	1.1×10^{-04}	1.8×10^{-19}	1.3×10^{-03}	5.3×10^{-20}
HD 107649	4.1×10^{-08}	5.2×10^{-25}	1.0×10^{-25}	5.9×10^{-06}	2.8×10^{-23}	2.0×10^{-06}	1.8×10^{-21}	3.2×10^{-05}	1.7×10^{-21}
HD 108857	3.5×10^{-05}	9.1×10^{-23}	1.5×10^{-22}	1.1×10^{-04}	7.4×10^{-22}	2.9×10^{-06}	3.5×10^{-21}	4.3×10^{-04}	3.3×10^{-20}
HD 109085	3.5×10^{-10}	9.5×10^{-27}	1.6×10^{-28}	2.2×10^{-07}	2.8×10^{-24}	1.2×10^{-07}	1.2×10^{-24}	1.4×10^{-06}	1.3×10^{-23}
HD 109832	2.0×10^{-06}	4.0×10^{-23}	2.7×10^{-23}	2.9×10^{-04}	1.4×10^{-21}	6.1×10^{-05}	3.6×10^{-20}	1.4×10^{-03}	8.4×10^{-20}
HD 110897	1.8×10^{-10}	5.4×10^{-27}	9.4×10^{-29}	8.3×10^{-10}	2.4×10^{-27}	8.2×10^{-08}	3.8×10^{-24}	3.3×10^{-07}	6.3×10^{-25}
HD 111520	3.5×10^{-06}	1.2×10^{-23}	8.4×10^{-25}	1.2×10^{-03}	1.1×10^{-21}	4.8×10^{-04}	2.0×10^{-19}	6.8×10^{-03}	5.8×10^{-20}
HD 111631	3.0×10^{-12}	2.4×10^{-28}	4.1×10^{-30}	2.0×10^{-09}	1.2×10^{-26}	3.4×10^{-10}	5.9×10^{-28}	9.3×10^{-09}	2.2×10^{-26}
HD 11171	6.4×10^{-11}	1.1×10^{-27}	1.9×10^{-29}	4.8×10^{-08}	1.3×10^{-25}	2.0×10^{-08}	2.8×10^{-26}	2.7×10^{-07}	4.3×10^{-25}
HD 112429	1.1×10^{-09}	1.4×10^{-26}	2.7×10^{-28}	5.0×10^{-09}	6.7×10^{-27}	4.9×10^{-07}	3.5×10^{-22}	2.0×10^{-06}	1.6×10^{-23}
HD 114082	4.3×10^{-03}	1.2×10^{-21}	1.9×10^{-21}	7.0×10^{-03}	7.9×10^{-21}	1.7×10^{-04}	1.5×10^{-19}	2.9×10^{-02}	4.5×10^{-19}
HD 115617	3.7×10^{-10}	4.6×10^{-26}	8.1×10^{-28}	1.4×10^{-09}	4.5×10^{-26}	1.4×10^{-07}	1.2×10^{-22}	5.7×10^{-07}	1.7×10^{-23}
HD 117214	3.4×10^{-03}	9.2×10^{-22}	1.6×10^{-21}	8.5×10^{-03}	6.3×10^{-21}	2.6×10^{-04}	1.2×10^{-19}	3.5×10^{-02}	3.6×10^{-19}
HD 118972	3.5×10^{-10}	1.4×10^{-26}	2.5×10^{-28}	9.0×10^{-10}	2.7×10^{-27}	8.9×10^{-08}	1.1×10^{-22}	3.6×10^{-07}	4.7×10^{-24}
HD 119124	4.0×10^{-09}	6.5×10^{-26}	1.3×10^{-27}	1.8×10^{-08}	3.5×10^{-26}	1.8×10^{-06}	1.6×10^{-21}	7.1×10^{-06}	7.5×10^{-23}
HD 119718	5.6×10^{-07}	1.1×10^{-23}	1.2×10^{-23}	1.2×10^{-04}	7.8×10^{-22}	2.8×10^{-05}	1.4×10^{-20}	5.9×10^{-04}	4.8×10^{-20}
HD 120534	9.0×10^{-07}	2.2×10^{-23}	5.5×10^{-24}	2.1×10^{-04}	1.5×10^{-21}	1.0×10^{-04}	1.3×10^{-19}	1.2×10^{-03}	1.0×10^{-19}
HD 121189	1.2×10^{-06}	2.3×10^{-23}	2.3×10^{-23}	9.1×10^{-05}	5.3×10^{-22}	9.1×10^{-06}	5.8×10^{-21}	4.0×10^{-04}	2.9×10^{-20}
HD 121191	6.3×10^{-03}	3.3×10^{-22}	8.7×10^{-22}	2.8×10^{-03}	3.8×10^{-21}	1.6×10^{-04}	1.4×10^{-19}	1.2×10^{-02}	1.7×10^{-18}

Table C2 – *continued*

Name	M_{CO} ($M_\oplus$)	$F_{CO\ 1300}$ (W m^{-2})	$F_{CO\ 870}$ (W m^{-2})	$M_{C\,I}$ ($M_\oplus$)	$F_{C\,I\ 610}$ (W m^{-2})	$M_{C\,II}$ ($M_\oplus$)	$F_{C\,II\ 158}$ (W m^{-2})	$M_{O\,I}$ ($M_\oplus$)	$F_{O\,I\ 63}$ (W m^{-2})
HD 122652	1.2×10^{-08}	8.0×10^{-26}	1.6×10^{-27}	6.0×10^{-08}	5.9×10^{-26}	6.0×10^{-06}	2.7×10^{-21}	2.4×10^{-05}	1.3×10^{-22}
HD 12467	3.7×10^{-08}	1.2×10^{-25}	3.7×10^{-27}	2.8×10^{-06}	2.7×10^{-24}	6.8×10^{-05}	3.2×10^{-20}	2.8×10^{-04}	2.0×10^{-21}
HD 124718	2.1×10^{-06}	5.2×10^{-23}	9.0×10^{-24}	3.6×10^{-04}	2.6×10^{-21}	2.4×10^{-04}	3.8×10^{-19}	2.4×10^{-03}	1.8×10^{-19}
HD 125451	4.8×10^{-10}	6.5×10^{-27}	1.1×10^{-28}	2.6×10^{-09}	2.6×10^{-27}	2.6×10^{-07}	2.0×10^{-23}	1.0×10^{-06}	1.3×10^{-24}
HD 125541	1.8×10^{-07}	3.2×10^{-24}	1.7×10^{-24}	2.0×10^{-05}	1.4×10^{-22}	4.2×10^{-06}	2.9×10^{-21}	9.7×10^{-05}	8.2×10^{-21}
HD 126265	4.9×10^{-07}	1.1×10^{-23}	2.1×10^{-24}	1.1×10^{-04}	7.6×10^{-22}	7.0×10^{-05}	9.4×10^{-20}	7.1×10^{-04}	5.5×10^{-20}
HD 127821	4.5×10^{-08}	4.5×10^{-25}	8.5×10^{-27}	1.2×10^{-05}	7.0×10^{-23}	2.1×10^{-05}	9.4×10^{-21}	1.3×10^{-04}	1.2×10^{-21}
HD 129590	1.1×10^{-02}	9.9×10^{-22}	1.6×10^{-21}	1.9×10^{-02}	6.5×10^{-21}	6.1×10^{-04}	1.7×10^{-19}	8.0×10^{-02}	3.8×10^{-19}
HD 131885	4.4×10^{-07}	8.3×10^{-24}	6.6×10^{-24}	6.6×10^{-04}	4.9×10^{-21}	2.1×10^{-03}	7.6×10^{-19}	1.1×10^{-02}	6.3×10^{-19}
HD 132254	1.4×10^{-10}	2.1×10^{-27}	3.7×10^{-29}	6.2×10^{-10}	4.7×10^{-28}	6.1×10^{-08}	4.8×10^{-24}	2.5×10^{-07}	2.8×10^{-25}
HD 13246	1.2×10^{-09}	5.8×10^{-27}	1.0×10^{-28}	4.9×10^{-09}	1.8×10^{-27}	4.8×10^{-07}	6.2×10^{-23}	2.0×10^{-06}	2.8×10^{-24}
HD 133803	5.0×10^{-06}	8.0×10^{-23}	1.6×10^{-22}	1.7×10^{-04}	1.0×10^{-21}	1.0×10^{-05}	7.7×10^{-21}	7.1×10^{-04}	4.6×10^{-20}
HD 134888	9.2×10^{-07}	1.5×10^{-23}	3.9×10^{-24}	1.6×10^{-04}	7.9×10^{-22}	6.4×10^{-05}	5.5×10^{-20}	9.1×10^{-04}	5.0×10^{-20}
HD 135599	2.3×10^{-09}	9.2×10^{-26}	1.7×10^{-27}	7.8×10^{-09}	3.7×10^{-26}	7.7×10^{-07}	1.1×10^{-21}	3.1×10^{-06}	5.5×10^{-23}
HD 135953	7.8×10^{-07}	2.8×10^{-24}	3.0×10^{-25}	1.7×10^{-04}	1.9×10^{-22}	1.7×10^{-04}	5.6×10^{-20}	1.3×10^{-03}	1.6×10^{-20}
HD 136482	6.3×10^{-10}	3.2×10^{-27}	5.1×10^{-28}	8.1×10^{-07}	1.5×10^{-24}	1.9×10^{-05}	6.9×10^{-21}	7.8×10^{-05}	1.6×10^{-21}
HD 137057	4.4×10^{-07}	5.1×10^{-24}	6.0×10^{-24}	1.2×10^{-04}	4.8×10^{-22}	3.0×10^{-05}	9.4×10^{-21}	5.8×10^{-04}	3.1×10^{-20}
HD 138923	2.7×10^{-10}	5.4×10^{-27}	3.3×10^{-26}	5.9×10^{-06}	1.2×10^{-22}	5.9×10^{-06}	2.2×10^{-20}	4.7×10^{-05}	2.7×10^{-18}
HD 138965	8.6×10^{-07}	1.1×10^{-23}	1.4×10^{-24}	3.6×10^{-04}	1.6×10^{-21}	4.8×10^{-04}	4.6×10^{-19}	3.4×10^{-03}	1.3×10^{-19}
HD 139664	1.0×10^{-08}	3.6×10^{-25}	7.2×10^{-27}	5.8×10^{-08}	7.2×10^{-25}	5.8×10^{-06}	1.3×10^{-20}	2.3×10^{-05}	7.6×10^{-22}
HD 140817	1.7×10^{-09}	2.5×10^{-26}	1.1×10^{-25}	3.1×10^{-05}	3.8×10^{-22}	1.2×10^{-04}	5.4×10^{-20}	6.2×10^{-04}	1.2×10^{-19}
HD 14082B	1.1×10^{-08}	4.9×10^{-25}	2.7×10^{-26}	8.5×10^{-07}	1.2×10^{-23}	1.8×10^{-06}	1.1×10^{-20}	1.1×10^{-05}	1.5×10^{-21}
HD 140840	2.8×10^{-08}	4.7×10^{-25}	3.0×10^{-25}	2.9×10^{-05}	2.2×10^{-22}	1.9×10^{-04}	8.4×10^{-20}	8.8×10^{-04}	7.6×10^{-20}
HD 141943	5.9×10^{-09}	5.9×10^{-26}	1.6×10^{-27}	1.7×10^{-07}	3.5×10^{-25}	1.7×10^{-06}	2.4×10^{-21}	7.6×10^{-06}	1.5×10^{-22}
HD 143675	9.7×10^{-06}	1.5×10^{-22}	2.3×10^{-22}	3.7×10^{-04}	1.4×10^{-21}	2.1×10^{-05}	1.4×10^{-20}	1.6×10^{-03}	7.0×10^{-20}
HD 144981	9.1×10^{-09}	1.1×10^{-25}	4.8×10^{-25}	1.7×10^{-07}	1.4×10^{-24}	1.7×10^{-05}	2.3×10^{-20}	6.7×10^{-05}	1.1×10^{-18}
HD 145229	5.7×10^{-09}	4.8×10^{-26}	9.2×10^{-28}	2.5×10^{-08}	3.0×10^{-26}	2.5×10^{-06}	1.0×10^{-21}	1.0×10^{-05}	4.9×10^{-23}
HD 1461	1.2×10^{-09}	2.1×10^{-26}	3.7×10^{-28}	5.0×10^{-09}	7.4×10^{-27}	4.9×10^{-07}	1.6×10^{-22}	2.0×10^{-06}	7.9×10^{-24}
HD 147594	6.7×10^{-08}	8.2×10^{-25}	4.9×10^{-25}	6.7×10^{-06}	3.7×10^{-23}	1.3×10^{-06}	6.4×10^{-22}	3.2×10^{-05}	2.1×10^{-21}
HD 151044	3.4×10^{-09}	3.8×10^{-26}	6.8×10^{-28}	1.8×10^{-08}	2.2×10^{-26}	1.8×10^{-06}	4.3×10^{-22}	7.2×10^{-06}	2.2×10^{-23}
HD 15115	3.2×10^{-07}	3.2×10^{-24}	1.1×10^{-25}	8.9×10^{-05}	4.2×10^{-22}	1.1×10^{-04}	1.7×10^{-19}	8.0×10^{-04}	2.1×10^{-20}
HD 151376	2.3×10^{-05}	1.9×10^{-23}	2.7×10^{-23}	1.4×10^{-05}	1.8×10^{-22}	7.8×10^{-08}	1.6×10^{-22}	5.5×10^{-05}	1.7×10^{-19}
HD 15257	3.2×10^{-08}	1.2×10^{-25}	2.2×10^{-27}	3.8×10^{-05}	1.3×10^{-22}	1.7×10^{-05}	1.2×10^{-21}	2.2×10^{-04}	7.0×10^{-22}
HD 15745	6.8×10^{-05}	2.1×10^{-21}	2.5×10^{-21}	2.9×10^{-03}	1.3×10^{-20}	2.3×10^{-04}	3.8×10^{-19}	1.3×10^{-02}	7.0×10^{-19}
HD 157728	7.1×10^{-08}	6.6×10^{-25}	2.1×10^{-26}	8.8×10^{-06}	2.8×10^{-23}	3.9×10^{-05}	5.4×10^{-20}	1.9×10^{-04}	4.1×10^{-21}
HD 158633	8.4×10^{-11}	4.6×10^{-27}	8.0×10^{-29}	3.8×10^{-10}	1.6×10^{-27}	3.8×10^{-08}	6.0×10^{-25}	1.5×10^{-07}	2.9×10^{-25}
HD 159492	3.9×10^{-08}	4.1×10^{-24}	1.8×10^{-24}	2.0×10^{-05}	8.8×10^{-22}	2.9×10^{-05}	1.1×10^{-19}	1.9×10^{-04}	1.0×10^{-19}
HD 161868	8.7×10^{-09}	2.1×10^{-25}	8.6×10^{-27}	7.5×10^{-07}	1.3×10^{-23}	7.4×10^{-05}	2.6×10^{-19}	3.0×10^{-04}	2.2×10^{-20}
HD 164249	1.8×10^{-06}	9.0×10^{-23}	1.9×10^{-23}	3.9×10^{-04}	5.6×10^{-21}	2.0×10^{-04}	5.7×10^{-19}	2.4×10^{-03}	3.5×10^{-19}
HD 165908	1.5×10^{-10}	5.5×10^{-27}	9.4×10^{-29}	9.8×10^{-10}	6.7×10^{-27}	9.7×10^{-08}	1.3×10^{-24}	3.9×10^{-07}	1.7×10^{-24}
HD 165908B	1.4×10^{-10}	2.5×10^{-26}	4.3×10^{-28}	5.5×10^{-10}	2.2×10^{-26}	5.4×10^{-08}	6.1×10^{-24}	2.2×10^{-07}	5.8×10^{-24}
HD 166	1.6×10^{-09}	8.9×10^{-26}	1.8×10^{-27}	4.6×10^{-09}	4.0×10^{-26}	4.6×10^{-07}	1.8×10^{-21}	1.9×10^{-06}	8.7×10^{-23}
HD 16743	2.8×10^{-07}	1.4×10^{-24}	4.4×10^{-26}	9.5×10^{-05}	2.0×10^{-22}	1.1×10^{-04}	7.9×10^{-20}	8.1×10^{-04}	9.3×10^{-21}
HD 169666	1.3×10^{-06}	1.3×10^{-22}	2.9×10^{-22}	1.5×10^{-05}	1.3×10^{-21}	3.5×10^{-07}	3.5×10^{-21}	6.0×10^{-05}	4.9×10^{-19}
HD 170773	3.9×10^{-07}	3.6×10^{-24}	8.5×10^{-26}	2.1×10^{-04}	2.7×10^{-21}	1.0×10^{-04}	1.0×10^{-19}	1.2×10^{-03}	2.6×10^{-20}
HD 17390	5.4×10^{-08}	2.4×10^{-25}	4.5×10^{-27}	1.9×10^{-05}	2.4×10^{-23}	2.4×10^{-05}	4.9×10^{-21}	1.7×10^{-04}	5.0×10^{-22}
HD 17925	7.6×10^{-11}	6.5×10^{-27}	1.1×10^{-28}	3.3×10^{-10}	2.7×10^{-27}	3.2×10^{-08}	1.0×10^{-24}	1.3×10^{-07}	5.8×10^{-25}
HD 182681	4.8×10^{-08}	2.8×10^{-24}	2.2×10^{-24}	6.4×10^{-05}	1.8×10^{-21}	6.5×10^{-04}	8.3×10^{-19}	2.9×10^{-03}	7.7×10^{-19}
HD 191089	1.3×10^{-05}	1.1×10^{-21}	1.1×10^{-21}	1.2×10^{-03}	1.4×10^{-20}	1.5×10^{-04}	3.8×10^{-19}	5.2×10^{-03}	7.7×10^{-19}
HD 191849	1.6×10^{-12}	3.9×10^{-28}	6.6×10^{-30}	9.2×10^{-10}	2.0×10^{-26}	2.1×10^{-10}	1.5×10^{-27}	4.5×10^{-09}	4.4×10^{-26}
HD 192758	1.1×10^{-06}	1.4×10^{-23}	1.5×10^{-24}	2.9×10^{-04}	1.3×10^{-21}	2.4×10^{-04}	3.0×10^{-19}	2.2×10^{-03}	9.1×10^{-20}
HD 195627	1.2×10^{-08}	1.6×10^{-25}	3.0×10^{-27}	5.3×10^{-07}	3.7×10^{-24}	8.5×10^{-06}	4.5×10^{-21}	3.6×10^{-05}	3.7×10^{-22}
HD 199260	4.0×10^{-10}	7.9×10^{-27}	1.4×10^{-28}	1.5×10^{-09}	2.5×10^{-27}	1.4×10^{-07}	7.3×10^{-23}	5.8×10^{-07}	3.5×10^{-24}
HD 201219	5.1×10^{-09}	3.5×10^{-26}	6.5×10^{-28}	2.2×10^{-08}	1.5×10^{-26}	2.2×10^{-06}	5.5×10^{-22}	9.0×10^{-06}	2.5×10^{-23}
HD 202628	4.1×10^{-09}	6.5×10^{-26}	1.1×10^{-27}	2.2×10^{-08}	7.8×10^{-26}	2.2×10^{-06}	4.3×10^{-22}	8.9×10^{-06}	3.7×10^{-23}
HD 202917	1.9×10^{-08}	2.4×10^{-25}	9.5×10^{-27}	1.3×10^{-06}	4.3×10^{-24}	4.6×10^{-06}	8.9×10^{-21}	2.3×10^{-05}	8.1×10^{-22}

Table C2 – *continued*

Name	$M_{\rm CO}$ ($M_\oplus$)	$F_{\rm CO\ 1300}$ (W m^{-2})	$F_{\rm CO\ 870}$ (W m^{-2})	$M_{\rm C\,I}$ ($M_\oplus$)	$F_{\rm C\,I\ 610}$ (W m^{-2})	$M_{\rm C\,II}$ ($M_\oplus$)	$F_{\rm C\,II\ 158}$ (W m^{-2})	$M_{\rm O\,I}$ ($M_\oplus$)	$F_{\rm O\,I\ 63}$ (W m^{-2})
HD 203	5.0×10^{-08}	4.8×10^{-24}	1.3×10^{-24}	7.2×10^{-06}	2.7×10^{-22}	3.8×10^{-06}	2.0×10^{-20}	4.4×10^{-05}	1.9×10^{-20}
HD 205674	1.6×10^{-07}	1.1×10^{-24}	3.8×10^{-26}	3.2×10^{-05}	8.7×10^{-23}	6.6×10^{-05}	7.0×10^{-20}	3.9×10^{-04}	6.8×10^{-21}
HD 206860	6.3×10^{-11}	1.8×10^{-27}	3.1×10^{-29}	2.0×10^{-10}	3.2×10^{-28}	1.9×10^{-08}	3.0×10^{-24}	7.9×10^{-08}	1.8×10^{-25}
HD 206893	7.3×10^{-08}	5.6×10^{-25}	1.2×10^{-26}	1.4×10^{-05}	5.1×10^{-23}	3.4×10^{-05}	2.2×10^{-20}	1.9×10^{-04}	1.8×10^{-21}
HD 207129	3.3×10^{-09}	1.2×10^{-25}	2.1×10^{-27}	1.9×10^{-08}	2.8×10^{-25}	1.8×10^{-06}	6.2×10^{-22}	7.5×10^{-06}	1.0×10^{-22}
HD 218340	6.9×10^{-09}	2.1×10^{-26}	4.0×10^{-28}	3.4×10^{-08}	9.3×10^{-27}	3.3×10^{-06}	4.1×10^{-22}	1.3×10^{-05}	1.8×10^{-23}
HD 218511	1.3×10^{-11}	5.1×10^{-28}	8.8×10^{-30}	5.6×10^{-09}	1.5×10^{-26}	2.8×10^{-09}	2.0×10^{-27}	3.4×10^{-08}	3.1×10^{-26}
HD 219482	1.3×10^{-09}	3.6×10^{-26}	7.7×10^{-28}	8.9×10^{-09}	3.6×10^{-26}	4.3×10^{-07}	1.1×10^{-21}	1.8×10^{-06}	5.1×10^{-23}
HD 219623	3.8×10^{-10}	8.6×10^{-27}	1.6×10^{-28}	1.3×10^{-09}	2.4×10^{-27}	1.3×10^{-07}	7.7×10^{-23}	5.4×10^{-07}	3.6×10^{-24}
HD 22049	1.3×10^{-09}	1.1×10^{-24}	2.0×10^{-26}	4.4×10^{-09}	8.1×10^{-24}	4.4×10^{-07}	6.3×10^{-21}	1.8×10^{-06}	2.7×10^{-21}
HD 221354	1.5×10^{-07}	8.6×10^{-24}	2.5×10^{-25}	1.6×10^{-05}	5.5×10^{-22}	5.7×10^{-05}	4.6×10^{-19}	2.9×10^{-04}	3.9×10^{-20}
HD 22179	4.2×10^{-08}	2.0×10^{-25}	7.6×10^{-27}	4.4×10^{-06}	5.5×10^{-24}	1.3×10^{-05}	8.9×10^{-21}	6.8×10^{-05}	8.5×10^{-22}
HD 221853	2.9×10^{-06}	1.2×10^{-22}	5.0×10^{-23}	5.4×10^{-04}	4.4×10^{-21}	1.2×10^{-04}	1.7×10^{-19}	2.6×10^{-03}	2.5×10^{-19}
HD 223340	3.1×10^{-08}	3.1×10^{-25}	1.1×10^{-26}	1.8×10^{-06}	5.0×10^{-24}	8.4×10^{-06}	1.3×10^{-20}	4.1×10^{-05}	1.0×10^{-21}
HD 22484	2.3×10^{-10}	1.1×10^{-26}	2.1×10^{-28}	8.3×10^{-10}	4.7×10^{-27}	8.2×10^{-08}	1.0×10^{-22}	3.3×10^{-07}	5.3×10^{-24}
HD 2262	1.8×10^{-10}	3.6×10^{-27}	7.6×10^{-29}	1.1×10^{-08}	3.3×10^{-26}	1.9×10^{-07}	3.7×10^{-22}	8.1×10^{-07}	1.8×10^{-23}
HD 23484	1.5×10^{-09}	5.3×10^{-26}	9.3×10^{-28}	6.5×10^{-09}	4.5×10^{-26}	6.4×10^{-07}	1.3×10^{-22}	2.6×10^{-06}	1.6×10^{-23}
HD 24636	2.7×10^{-08}	5.7×10^{-25}	5.8×10^{-26}	4.3×10^{-06}	3.1×10^{-23}	3.7×10^{-06}	7.9×10^{-21}	3.2×10^{-05}	2.5×10^{-21}
HD 25457	4.9×10^{-09}	1.3×10^{-25}	2.3×10^{-27}	2.8×10^{-08}	2.6×10^{-25}	2.7×10^{-06}	1.6×10^{-21}	1.1×10^{-05}	1.3×10^{-22}
HD 25998	8.1×10^{-10}	1.8×10^{-26}	3.2×10^{-28}	3.4×10^{-09}	6.2×10^{-27}	3.4×10^{-07}	1.7×10^{-22}	1.4×10^{-06}	8.1×10^{-24}
HD 27290	1.2×10^{-09}	2.6×10^{-26}	4.5×10^{-28}	7.2×10^{-09}	3.9×10^{-26}	7.1×10^{-07}	1.6×10^{-22}	2.9×10^{-06}	1.7×10^{-23}
HD 274255	1.1×10^{-09}	3.0×10^{-26}	5.2×10^{-28}	3.3×10^{-09}	5.5×10^{-27}	3.2×10^{-07}	9.9×10^{-23}	1.3×10^{-06}	4.7×10^{-24}
HD 27638B	3.1×10^{-08}	1.8×10^{-25}	3.9×10^{-27}	1.4×10^{-07}	1.4×10^{-25}	1.4×10^{-05}	7.7×10^{-21}	5.8×10^{-05}	3.8×10^{-22}
HD 30447	1.9×10^{-06}	2.0×10^{-23}	2.2×10^{-24}	5.1×10^{-04}	1.7×10^{-21}	3.3×10^{-04}	3.0×10^{-19}	3.4×10^{-03}	1.0×10^{-19}
HD 30495	2.1×10^{-10}	1.1×10^{-26}	1.9×10^{-28}	1.1×10^{-09}	7.7×10^{-27}	1.1×10^{-07}	4.4×10^{-24}	4.5×10^{-07}	1.9×10^{-24}
HD 3126	1.6×10^{-08}	1.1×10^{-25}	2.5×10^{-27}	2.6×10^{-07}	3.4×10^{-25}	8.2×10^{-06}	5.6×10^{-21}	3.4×10^{-05}	2.8×10^{-22}
HD 31392	2.6×10^{-09}	3.8×10^{-26}	6.6×10^{-28}	6.7×10^{-07}	1.5×10^{-24}	1.0×10^{-06}	1.9×10^{-23}	6.8×10^{-06}	1.0×10^{-23}
HD 33636	5.1×10^{-10}	5.8×10^{-27}	9.9×10^{-29}	3.1×10^{-09}	2.9×10^{-27}	3.1×10^{-07}	2.9×10^{-24}	1.2×10^{-06}	6.2×10^{-25}
HD 34324	2.3×10^{-08}	3.9×10^{-26}	6.7×10^{-28}	2.0×10^{-05}	6.7×10^{-24}	6.1×10^{-06}	5.3×10^{-23}	1.1×10^{-04}	3.0×10^{-23}
HD 35650	1.0×10^{-09}	3.0×10^{-26}	5.1×10^{-28}	3.5×10^{-09}	9.6×10^{-27}	3.5×10^{-07}	6.1×10^{-23}	1.4×10^{-06}	4.3×10^{-24}
HD 35841	2.9×10^{-06}	3.5×10^{-23}	8.6×10^{-24}	5.9×10^{-04}	1.8×10^{-21}	2.5×10^{-04}	1.6×10^{-19}	3.4×10^{-03}	1.1×10^{-19}
HD 35850	8.6×10^{-10}	1.1×10^{-26}	2.0×10^{-28}	3.8×10^{-09}	4.5×10^{-27}	3.8×10^{-07}	7.7×10^{-23}	1.5×10^{-06}	4.0×10^{-24}
HD 3670	3.1×10^{-07}	8.1×10^{-25}	2.8×10^{-26}	8.6×10^{-05}	6.5×10^{-23}	1.1×10^{-04}	4.3×10^{-20}	7.8×10^{-04}	4.9×10^{-21}
HD 36968	3.8×10^{-06}	1.7×10^{-23}	2.8×10^{-24}	1.0×10^{-03}	1.1×10^{-21}	4.8×10^{-04}	1.4×10^{-19}	6.0×10^{-03}	6.6×10^{-20}
HD 37484	2.5×10^{-08}	8.5×10^{-26}	1.8×10^{-27}	1.6×10^{-06}	9.2×10^{-25}	1.4×10^{-05}	3.6×10^{-21}	6.1×10^{-05}	1.9×10^{-22}
HD 37594	1.7×10^{-07}	2.0×10^{-24}	7.3×10^{-26}	4.0×10^{-05}	2.2×10^{-22}	7.5×10^{-05}	1.3×10^{-19}	4.6×10^{-04}	1.4×10^{-20}
HD 377	6.0×10^{-08}	9.0×10^{-25}	3.6×10^{-26}	5.9×10^{-06}	2.9×10^{-23}	2.0×10^{-05}	4.5×10^{-20}	1.0×10^{-04}	4.3×10^{-21}
HD 38206	2.6×10^{-08}	2.2×10^{-25}	1.7×10^{-26}	2.2×10^{-06}	7.1×10^{-24}	2.1×10^{-04}	2.0×10^{-19}	8.7×10^{-04}	2.5×10^{-20}
HD 38207	7.6×10^{-07}	2.0×10^{-24}	8.6×10^{-26}	2.5×10^{-04}	2.1×10^{-22}	2.0×10^{-04}	7.9×10^{-20}	1.8×10^{-03}	1.3×10^{-20}
HD 38678	2.1×10^{-09}	1.7×10^{-24}	3.3×10^{-24}	3.3×10^{-06}	2.0×10^{-21}	1.2×10^{-05}	5.9×10^{-19}	5.9×10^{-05}	2.2×10^{-18}
HD 38858	2.7×10^{-09}	1.1×10^{-25}	2.0×10^{-27}	1.2×10^{-08}	1.5×10^{-25}	1.2×10^{-06}	8.9×10^{-22}	4.9×10^{-06}	7.5×10^{-23}
HD 40136	5.6×10^{-10}	5.6×10^{-26}	2.2×10^{-27}	1.5×10^{-08}	4.6×10^{-25}	1.3×10^{-07}	2.5×10^{-21}	5.8×10^{-07}	1.6×10^{-22}
HD 40540	3.6×10^{-07}	3.2×10^{-24}	3.1×10^{-25}	7.9×10^{-05}	2.3×10^{-22}	8.3×10^{-05}	7.2×10^{-20}	6.5×10^{-04}	2.0×10^{-20}
HD 45184	4.1×10^{-09}	8.4×10^{-26}	1.6×10^{-27}	1.9×10^{-08}	7.2×10^{-26}	1.9×10^{-06}	1.3×10^{-21}	7.6×10^{-06}	7.0×10^{-23}
HD 50554	1.3×10^{-09}	1.3×10^{-26}	2.4×10^{-28}	5.8×10^{-09}	5.7×10^{-27}	5.7×10^{-07}	9.2×10^{-23}	2.3×10^{-06}	4.8×10^{-24}
HD 50571	1.8×10^{-08}	1.6×10^{-25}	3.0×10^{-27}	2.1×10^{-06}	4.6×10^{-24}	1.0×10^{-05}	3.2×10^{-21}	5.0×10^{-05}	2.3×10^{-22}
HD 52265	6.7×10^{-10}	7.6×10^{-27}	1.4×10^{-28}	2.8×10^{-09}	2.6×10^{-27}	2.8×10^{-07}	6.3×10^{-23}	1.1×10^{-06}	3.0×10^{-24}
HD 53143	8.7×10^{-09}	4.4×10^{-25}	1.4×10^{-26}	4.4×10^{-07}	5.6×10^{-24}	2.1×10^{-06}	1.6×10^{-20}	1.0×10^{-05}	1.2×10^{-21}
HD 54341	6.1×10^{-08}	3.7×10^{-25}	4.0×10^{-26}	2.1×10^{-05}	4.7×10^{-23}	4.3×10^{-04}	2.3×10^{-19}	1.8×10^{-03}	3.8×10^{-20}
HD 59967	3.5×10^{-10}	6.7×10^{-27}	1.2×10^{-28}	1.3×10^{-09}	1.5×10^{-27}	1.3×10^{-07}	1.7×10^{-23}	5.3×10^{-07}	8.9×10^{-25}
HD 60491	4.7×10^{-09}	9.7×10^{-26}	2.2×10^{-27}	1.6×10^{-07}	5.3×10^{-25}	1.2×10^{-06}	2.6×10^{-21}	5.4×10^{-06}	1.5×10^{-22}
HD 61005	1.8×10^{-06}	1.4×10^{-22}	2.2×10^{-23}	2.7×10^{-04}	6.8×10^{-21}	2.0×10^{-04}	1.0×10^{-18}	1.9×10^{-03}	4.3×10^{-19}
HD 6798	2.3×10^{-08}	4.3×10^{-25}	9.8×10^{-26}	2.8×10^{-06}	2.1×10^{-23}	2.8×10^{-04}	2.7×10^{-19}	1.1×10^{-03}	8.4×10^{-20}
HD 6963	1.8×10^{-09}	2.4×10^{-26}	4.2×10^{-28}	7.2×10^{-09}	7.2×10^{-27}	7.2×10^{-07}	1.6×10^{-22}	2.9×10^{-06}	7.7×10^{-24}
HD 69830	5.6×10^{-06}	4.6×10^{-22}	9.2×10^{-22}	3.3×10^{-06}	3.2×10^{-21}	1.6×10^{-08}	1.4×10^{-21}	1.3×10^{-05}	1.9×10^{-19}
HD 71722	1.6×10^{-08}	1.0×10^{-25}	5.5×10^{-27}	4.9×10^{-07}	1.0×10^{-24}	4.8×10^{-05}	4.3×10^{-20}	1.9×10^{-04}	3.9×10^{-21}

Table C2 *– continued*

Name	M_{CO} ($M_\oplus$)	$F_{CO\ 1300}$ (W m^{-2})	$F_{CO\ 870}$ (W m^{-2})	$M_{C\,I}$ ($M_\oplus$)	$F_{C\,I\ 610}$ (W m^{-2})	$M_{C\,II}$ ($M_\oplus$)	$F_{C\,II\ 158}$ (W m^{-2})	$M_{O\,I}$ ($M_\oplus$)	$F_{O\,I\ 63}$ (W m^{-2})
HD 72905	6.8×10^{-11}	3.0×10^{-27}	5.2×10^{-29}	2.3×10^{-10}	5.6×10^{-28}	2.3×10^{-08}	3.5×10^{-24}	9.1×10^{-08}	2.4×10^{-25}
HD 73350	6.8×10^{-09}	1.2×10^{-25}	2.1×10^{-27}	3.3×10^{-08}	1.4×10^{-25}	3.3×10^{-06}	1.8×10^{-21}	1.3×10^{-05}	1.1×10^{-22}
HD 7590	1.0×10^{-08}	1.8×10^{-25}	3.3×10^{-27}	3.2×10^{-07}	1.4×10^{-24}	5.5×10^{-06}	2.1×10^{-21}	2.3×10^{-05}	1.6×10^{-22}
HD 76151	1.1×10^{-10}	3.4×10^{-27}	5.9×10^{-29}	3.5×10^{-10}	5.9×10^{-28}	3.4×10^{-08}	8.6×10^{-24}	1.4×10^{-07}	4.5×10^{-25}
HD 76543	5.5×10^{-08}	1.1×10^{-24}	7.9×10^{-26}	3.5×10^{-06}	2.8×10^{-23}	5.8×10^{-05}	1.4×10^{-19}	2.5×10^{-04}	1.7×10^{-20}
HD 76582	3.5×10^{-07}	7.8×10^{-24}	6.2×10^{-25}	7.7×10^{-05}	7.5×10^{-22}	1.3×10^{-04}	3.3×10^{-19}	8.5×10^{-04}	6.4×10^{-20}
HD 80950	7.4×10^{-10}	4.2×10^{-26}	8.2×10^{-26}	9.6×10^{-06}	3.6×10^{-22}	4.1×10^{-05}	6.2×10^{-20}	2.0×10^{-04}	1.3×10^{-19}
HD 82443	7.3×10^{-10}	2.6×10^{-26}	5.5×10^{-28}	2.4×10^{-08}	1.1×10^{-25}	1.4×10^{-07}	4.4×10^{-22}	6.7×10^{-07}	2.3×10^{-23}
HD 82943	8.2×10^{-09}	1.1×10^{-25}	2.1×10^{-27}	4.2×10^{-08}	1.4×10^{-25}	4.2×10^{-06}	2.6×10^{-21}	1.7×10^{-05}	1.4×10^{-22}
HD 84075	2.8×10^{-08}	9.8×10^{-26}	2.9×10^{-27}	2.4×10^{-06}	1.9×10^{-24}	9.6×10^{-06}	5.0×10^{-21}	4.8×10^{-05}	3.6×10^{-22}
HD 84870	2.0×10^{-07}	2.7×10^{-25}	5.3×10^{-27}	1.4×10^{-04}	8.3×10^{-23}	5.0×10^{-05}	3.9×10^{-21}	7.7×10^{-04}	9.3×10^{-22}
HD 85672	1.9×10^{-06}	2.6×10^{-23}	7.9×10^{-24}	4.9×10^{-04}	1.7×10^{-21}	2.2×10^{-04}	1.3×10^{-19}	2.8×10^{-03}	1.1×10^{-19}
HD 86087	1.8×10^{-07}	7.0×10^{-24}	8.4×10^{-24}	4.1×10^{-04}	7.6×10^{-21}	1.8×10^{-03}	1.0×10^{-18}	8.7×10^{-03}	1.2×10^{-18}
HD 87696	5.6×10^{-10}	3.0×10^{-26}	2.4×10^{-27}	2.3×10^{-09}	1.4×10^{-25}	2.3×10^{-07}	5.6×10^{-21}	9.4×10^{-07}	1.8×10^{-21}
HD 8907	5.5×10^{-08}	5.1×10^{-25}	1.1×10^{-26}	8.6×10^{-06}	3.9×10^{-23}	2.6×10^{-05}	1.9×10^{-20}	1.4×10^{-04}	1.6×10^{-21}
HD 90089	9.3×10^{-11}	1.8×10^{-27}	3.2×10^{-29}	8.1×10^{-08}	3.0×10^{-25}	2.0×10^{-08}	3.7×10^{-26}	4.0×10^{-07}	9.1×10^{-25}
HD 92945	5.4×10^{-08}	1.2×10^{-24}	2.3×10^{-26}	5.6×10^{-06}	8.6×10^{-23}	2.3×10^{-05}	2.3×10^{-20}	1.1×10^{-04}	2.4×10^{-21}
HD 95086	1.1×10^{-05}	2.2×10^{-22}	8.4×10^{-23}	2.6×10^{-03}	7.9×10^{-21}	7.3×10^{-04}	5.7×10^{-19}	1.3×10^{-02}	4.4×10^{-19}
HD 95698	4.4×10^{-08}	2.1×10^{-25}	5.9×10^{-27}	2.9×10^{-06}	4.4×10^{-24}	2.7×10^{-05}	1.8×10^{-20}	1.2×10^{-04}	1.2×10^{-21}
HIP 11437	1.2×10^{-07}	2.7×10^{-24}	1.6×10^{-25}	1.0×10^{-05}	7.4×10^{-23}	2.2×10^{-05}	6.4×10^{-20}	1.3×10^{-04}	9.4×10^{-21}
HIP 1368	3.5×10^{-10}	1.4×10^{-26}	2.4×10^{-28}	1.1×10^{-07}	7.3×10^{-25}	9.4×10^{-08}	5.3×10^{-25}	8.1×10^{-07}	3.3×10^{-24}
HIP 32480	3.8×10^{-09}	1.3×10^{-25}	2.2×10^{-27}	2.3×10^{-08}	3.5×10^{-25}	2.3×10^{-06}	8.7×10^{-22}	9.1×10^{-06}	1.3×10^{-22}
HIP 43534	1.6×10^{-09}	5.5×10^{-26}	9.4×10^{-28}	7.4×10^{-07}	6.7×10^{-24}	3.0×10^{-07}	2.6×10^{-24}	4.2×10^{-06}	2.5×10^{-23}
HIP 63942	1.6×10^{-09}	4.3×10^{-26}	7.5×10^{-28}	5.1×10^{-09}	1.0×10^{-26}	5.0×10^{-07}	1.8×10^{-22}	2.0×10^{-06}	8.7×10^{-24}
HIP 74995	1.7×10^{-11}	3.8×10^{-27}	6.5×10^{-29}	4.9×10^{-11}	8.6×10^{-28}	4.8×10^{-09}	5.6×10^{-26}	1.9×10^{-08}	1.4×10^{-25}
HR 4796	1.1×10^{-04}	3.8×10^{-21}	1.4×10^{-20}	1.7×10^{-01}	4.9×10^{-20}	1.8×10^{-02}	8.2×10^{-19}	7.5×10^{-01}	4.4×10^{-18}

Column 1: star's name. *Column 2:* CO mass. *Columns 3 and 4:* CO flux at 1.3 mm, 870 microns. *Column 5:* C I mass. *Column 6:* C I flux at 610 microns. *Column 7:* C II mass. *Column 8:* C II flux at 158 microns. *Column 9:* O I mass (with extra water, see Section 6.2). *Column 10:* O I flux at 63 microns (with extra water).

This paper has been typeset from a TeX/LaTeX file prepared by the author.